Study of the Formation and Dissolution of δ-ferrite During High Temperature Forging Processing of Austenitic, Martensitic and PH Stainless Steels

by

Pedro de Souza Ciacco

Bachelor in Materials Engineering, Universidade Federal de Itajubá, 2019

Submitted to the Graduate Faculty of the

Swanson School of Engineering in partial fulfillment

of the requirements for the degree of

Master of Science in Materials Science and Engineering

University of Pittsburgh

2023

UNIVERSITY OF PITTSBURGH

SWANSON SCHOOL OF ENGINEERING

This thesis was presented

by

Pedro de Souza Ciacco

It was defended on

March 6, 2023

and approved by

Susheng Tan, Ph. D., Associate Professor, Department of Electrical and Computer Engineering

Esta Abelev, Ph. D., Associate Professor, Department of Mechanical Engineering and Materials Science.
Thesis Advisor: Calixto Isaac Garcia, Ph. D., Professor, Department of Mechanical Engineering and Materials Science

Study of the Formation and Dissolution of δ-ferrite During High Temperature Forging Processing of Austenitic, Martensitic and PH Stainless Steels

Pedro de Souza Ciacco, MSc.

University of Pittsburgh, 2023

The present study develops a logical and novel approach to understand the formation and dissolution of δ-ferrite during high temperature forging processing of 15-5 PH, Jethete (154-M), and 304 L stainless steels. This new process proposes alternative routes to examine the dissolution kinetics behavior of δ-ferrite, creating an in-depth comprehension about the synergistic effect of chemical composition, reheating temperature, deformation temperature, amount of deformation (ε), and strain rate ($\dot{\varepsilon}$). In addition, well-known conventional annealing heat treatments, based exclusively on time and temperature, acted as a parameter to be further compared with the new proposed technique. The introduction of deformation at high temperatures is expected to increase the kinetics of dissolution of δ-ferrite, consequently decreasing the total heat treatment time to fully dissolve this microconstituent. Combining time, temperature, and deformation, a forging process could be represented, while the effect of those forging strategies on the formation and dissolution behavior of δ-ferrite could be understood.

Modern electron optics analytical techniques were used to characterize all aspects of the stainless-steel alloys, their microstructural development, and the characteristics of the formation and dissolution of δ-ferrite. Those aspects included stereological features, morphology, area fraction, and chemical composition differences. The changes in area fraction and stereology could be observed under Optical Microscopy (OM), as the δ-ferrite morphology and area fraction changed as time and temperature were varied. The amount of δ-ferrite decreased after conventional

annealing heat treatments, and even more when time, temperature, and deformation were combined, as suggested by this new approach. For the 15-5 PH alloy, an average of 0.9% in area fraction of δ-ferrite could be seen after compression and post processing of 10 minutes at a high temperature. In contrast, the specimen conventionally annealed for 3 hours exhibited an area fraction average of 1.2%. Both the Jethete and 304L alloys followed the same tendency, presenting lower δ-ferrite fractions after deformation.

Electron Probe Micro Analysis (EPMA) was utilized to investigate chemical composition variances, contrasting the as-received materials and the specimen submitted to various heat treatments and laboratory physical simulations. As the dissolution starts to take place, chemical variations along the matrix and δ-ferrite could be noticed, mainly in terms of Chromium. Aiming the homogenization of the microstructure, the Cr content tends to be equalized, not showing discrepancies between the matrix and the δ-ferrite areas. The 304L alloy heat treated for longer times and higher temperatures presented a δ-ferrite phase with Cr depletion in comparison with the same material when having its start condition analyzed (~21.wt% vs, ~27.wt%, respectively). Furthermore, EDS compositional measurements were used as an input for further thermodynamic calculations, conducted with the aid of ThermoCalc and DICTRA, estimating the time for fully dissolving δ-ferrite after long isothermal heat treatments. According to DICTRA, the microstructure of the 15-5PH material is expected to be fully chemical homogenized after 10 hours of annealing at 1000°C, and 6 hours at 1150°C. For the Jethete alloy, a similar trend could be noticed for the simulation conducted at 1000°C, with a longer chemical accommodation time of 8 hours predicted after 1150°C. From the three analyzed stainless steels, the 304L alloy showed a faster dissolution attached to the matrix and δ-ferrite chemical homogenization, where 2 hours of annealing at 1150° was sufficient to consistently approximate the δ-ferrite and matrix chemistries.

Table of Contents

List of Tables

List of Figures

Preface

Since 2019, when I joined the Ferrous Physical Metallurgy group, I have been fortunate to meet an enormous number of people, which helped develop myself as a professional, and mainly as a person. Each of them somehow pavemented my path and made this journey, under all circumstances, a little easier, bringing more joy and happiness. Of course, my gratitude goes beyond this section, and extends to all the people I have met during my years here.

First and foremost, I would like to praise and thank God, who has granted blessing, peace, and knowledge, guiding me, and enlightening the choices and decisions I have made throughout the way. Thanks very much to my family that passed this beautiful faith to me.

I would also like to thank my advisor, Prof. Dr. C. Isaac Garcia, firstly for the enormous opportunity of joining your research group, and for all the guidance, help, patience, and sensibility. You have always been a professional reference to me, considering all your thoughtful insights, and expertise in Materials Science and in Physical Metallurgy. After all these years, you have also become a personal inspiration, not only for your passion at work, but for making me and everyone that surrounds you welcome and comfortable. Thanks for understanding every single problem, being always open and available to talk about life. You are a living example, and my sincere thanks go to you.

I want to thank my committee members Dr. Esta Abelev and Dr. Susheng Tan for your enormous contributions, suggestions, and teachings throughout my whole time at the University of Pittsburgh, not only as a graduate student. You both have tremendously collaborated to my development as a professional, always motivating and instigating my analytical thoughts. I also want to give a special thanks to Dr. Soumya Sridar, for all your guidance and patience on teaching how to use and adapt the software ThermoCalc/DICTRA to my needs.

To all the friends and peers that stayed close to me during these years, I express here my deepest gratitude. Each moment, discussion, and moral support were valuable and taught me a lot. Certainly, I consider each of you my Pittsburgh family. I specially thank my closest friends and co-workers Artur Ferreira, Gregorio Solis, Javier Carreno, Luis Simoes, Marcos Moritugui and Yuankang Wang. Furthermore, I would like to thank all the undergraduate students for arising my wish to do better every day. I am grateful for meeting, teaching, and of course learning from each of you. Thanks to Eve, that made my life more colorful since the day we met. I really appreciate all the laughs and happy moments.

In the end, I would like to thank the ones I love the most. To my father Luís Fernando, my mother Josiana and my sister Luísa. Even being physically far, you have never distanced yourselves from me, not even for a minute. Thanks for staying close, supporting, praying and cheering for all my accomplishes here. I would have never succeeded without your unconditional love. My heart will always be with you. Thanks to my grandfather José Roberto, example of fight, resilience, and love, and to my two little stars I lost throughout my years here, my grandmothers Aldenise and Ana Olívia. Every time I close my eyes, I immediately think about you, and I know you both are interceding to God for me. Thank you for everything! More often than not the distance felt unsurpassed, but all of you made this achievement possible. No further words are necessary, since any could ever describe what you mean to me. This is all for you, my family!

1.0 Introduction

Stainless steels are a well-known and important category of alloy which are widely used on a vast range of applications, going from simple culinary uses, passing through surgical tools, and getting to more robust uses, such as on construction, automotive and aerospace industries, for example. These steels can be sub-divided into other three classes, based on properties, microstructures, and different applications. Ferritic, Austenitic and Martensitic stainless steels. For having a different range of chemical compositions and, therefore, phase distributions, these materials embrace a wide set of properties, but with one common challenge that has risen throughout the time: δ-ferrite as a major constituent on their microstructure.

δ-ferrite is a deleterious phase component that adversely affects stainless steel's properties, promoting cracks at its interface with the matrix, impairing corrosion resistance, and acting as nucleation sites during hot deformation. Consequently, the dissolution of this secondary phase is one of the primmest topics of study in this field. Traditional approaches to reduce the volume fraction of δ-ferrite have been designed by using long isothermal heat treatments. The considerable amount of energy offered by high temperatures of the system, in combination with the long soaking times, promotes shorter diffusion paths, inducing and favoring the δ-ferrite dissolution. However, different alloys exhibit distinct responses to those treatments, as chemical composition is one of the prime parameters that dictates how the diffusion path is shortened.

For that reason, the present study intends to propound a new dissolution approach, that would decrease the total dissolution time of δ-ferrite. The combination of isothermal heat treatments and hot deformation would create a more energized system, decreasing the δ-ferrite fraction after shorter treatment times. In other words, the impact of different thermomechanical processes on the final microstructure and δ-ferrite fraction of various stainless-steel alloys will be analyzed. After analyzing different systems and alloys, empirical thermodynamic calculations will be utilized to determine the optimum time for δ-ferrite dissolution.

2.0 Background

2.1 Stainless Steels

Stainless steels are defined as iron-based alloys that contain a considerable addition of chromium, which is required to prevent oxidation. The stainless characteristics are achieved through the formation of an adherent chromium-rich oxide surface film, named passivated layer, which forms and heals itself in the presence of oxygen. [1] In order to form this film, a minimum of 10.5% chromium is necessary, and other chemical elements, such as nickel, carbon, manganese, molybdenum, copper, and silicon, can be combined to enhance physical properties. [2] Therefore, the alloying element control promotes a vast range of strength and corrosion resistance, with each of the chemical components acting for specific purposes. [3] For this wide range of physical properties, the stainless steels are divided in different categories [4] , as exemplified on Figure 1.

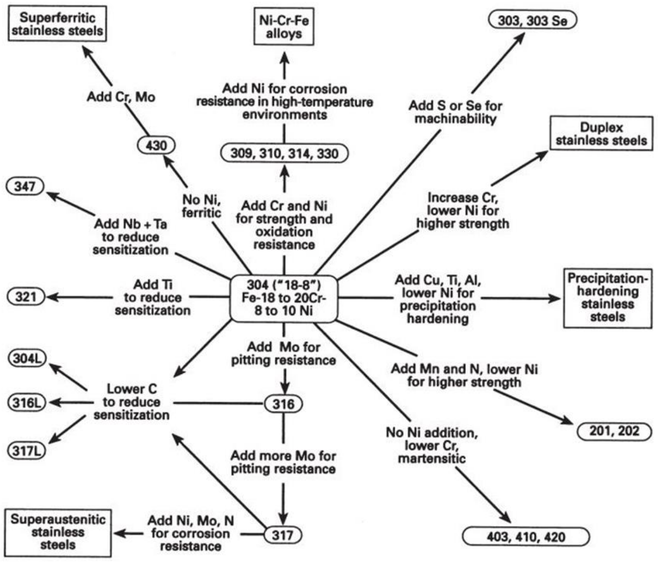

Figure 1: Composition and property linkages in the stainless-steel family of alloys. [5]

Since the chemical composition is the main determinant of the stainless-steels phases and microstructures, knowing the stabilizing effect of each element is important. Therefore, the Schaeffler diagram can be used to predict which phase is the stable phase for a given Cr and Ni composition, main components of stainless steel. [6] Figure 2 shows the variation of chromium and nickel equivalent weight percent, drawing limits between the four main categories of stainless steels (austenitic, ferritic, martensitic, and duplex). However, since the present work focused on the characterization of only three classes (precipitation hardening, martensitic and austenitic stainless steels), more detailed theoretical information will be introduced in the following sections.

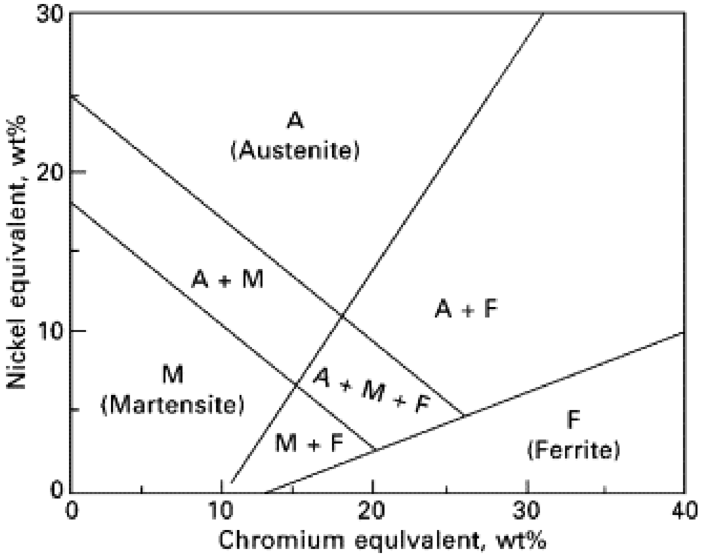

Figure 2: Schaeffler diagram. [7]

The compositional fields of ferrite, austenite, and martensite at room temperature, and in terms of chromium and nickel equivalents, is plotted on the Schaeffler diagram, showing the regions of existence of those three phases for the Fe-Cr-Ni alloys. However, when other alloying elements are considered, this approach becomes much wider. Accordingly, for the Cr equivalent empirical calculations, the most common ferrite-forming elements (in wt. %) are taken in consideration, whereas for the Ni equivalent, the familiar austenite-forming elements (in wt. %) are accounted, as represented on Equations 2-1 and 2-2. [1]

$$\text{Cr equivalent} = (\text{Cr}) + 2(\text{Si}) + 1.5(\text{Mo}) + 5(\text{V}) + 5.5(\text{Al}) + 1.75(\text{Nb}) + 1.5(\text{Ti}) + 0.75(\text{W}) \quad \textbf{Eq. 2-1}$$

$$\text{Ni equivalent} = (\text{Ni}) + (\text{Co}) + 0.5(\text{Mn}) + 0.3(\text{Cu}) + 25(\text{N}) + 30(\text{C}) \quad \textbf{Eq. 2-2}$$

2.1.1 Precipitation Hardening Stainless Steels

Precipitation Hardening (PH) stainless steels are Fe-Ni-Cr alloys with the addition of chemical elements, such as aluminum, titanium, niobium, and copper. Those elements act as increasing strength, ductility, and corrosion resistance by precipitation during aging. [8] Those stainless steels can be either austenitic, semi-austenitic or martensitic depending on the alloy composition. [7] The most common alloys, 15-5 PH (15% Cr and 5% Ni) and 17-4 PH, are fully martensitic at room temperatures, but presenting a soft and low-carbon martensite when compared with martensitic stainless-steels. This soft matrix attains great strength with high toughness, in addition combining a good corrosion resistance. All those attributes are strictly related to the necessary processing steps that are commonly adopted during manufacturing. [7]

One characteristic of these alloys is the lower austenitic stability among all Fe-Cr-Ni materials, exploiting the retained austenitic structure at room temperatures, and the subsequent formation of martensite after thermal treatments below zero degrees Celsius. This martensite is usually further hardened by the coherent precipitation of intermetallic elements, such as copper, nitrides, or even phosphides, at temperatures between 400 and 600°C, adjusting the final mechanical properties. [9]

2.1.2 Martensitic Stainless Steels

Martensitic stainless steels are represented by Fe-Cr-C alloys which contain up to 0.6% of carbon. This high carbon content facilitates the martensite formation at room temperatures. For this reason, this grade of steel is typically processed by fully austenitization at high temperatures, with subsequent quenching and tempering treatments. The first heat treatment step is adopted to entirely homogenize the steel microstructure; the second promotes martensitic transformation, (preventing from embrittlement issues); and the third is responsible for increasing ductility and toughness. At the end of the processing, martensitic stainless steels are usually composed of a α' matrix, undissolved carbides, and, in some cases, δ-ferrite. [10]

Considered a metallurgically complex material, martensitic stainless steels, at annealed conditions, presents a microstructure of ferrite and spheroidized carbides. This distribution is changed to increase strength and corrosion resistance, and to enlarge the spectrum of applications for these alloys. This enhance in properties is possible for the higher amount of carbon and lower amount of chromium present. Therefore, the mechanical and corrosion resistances range is strongly attached to the chemical composition, i.e., to the amount of carbon and other alloying elements in the austenite. [11]

2.1.3 Austenitic Stainless Steels

Austenitic stainless steels are well known for their exceptional corrosion resistance and mechanical properties, associating high strength, toughness, and formability. For that reason, this alloy constitutes the largest stainless-steel family in terms of alloy and usage. However, at least 15% of chromium is required to stabilize the austenite (FCC structure) under normal conditions.

In addition, a considerably high amount of other alloying elements is required, such as nickel, manganese, and nitrogen. The combination of all those elements with carbon would create a favorable environment for the austenite stabilization. [5]

The AISI 300 family embrace materials corresponded to the Fe-Cr-Ni alloys and modified versions of these alloys. For example, the 304 stainless steels generally contain 16% to 26% of Cr and 10% to 22% of Ni, along with small amounts of other alloying elements, that can include Mo, Ti, and Nb. On the other hand, the AISI 200 grade also corresponds to Fe-Cr-Ni alloys, but with Mn as the main alloying element, and the Super-Austenitic grade contains considerably high amounts of Mo, Ni, and N for improving even more the corrosion resistance. [12]

2.2 δ-ferrite

δ-ferrite is a metallurgical phase commonly found in stainless steels. Largely regarded as the same phase as ferrite, for presenting a body centered cubic (BCC) crystal structure, there is a significant temperature gap that separates both phases, as δ-ferrite is only formed at considerably high temperatures. [13] Besides the temperature range, the presence of δ-ferrite depends on chemical composition and on cooling rate during solidification. [14] Appraising the material's chemistry, the ferrite content present on stainless steels can be estimated and calculated using the Schoefer diagram, represented on Figure 3. This approach considers both the chromium and nickel equivalent (Equations 2-1 and 2-2). In general, as properties and performance of materials are correlated to their microstructural distribution, it is important to investigate and evaluate the impact of each microstructural feature on final properties.

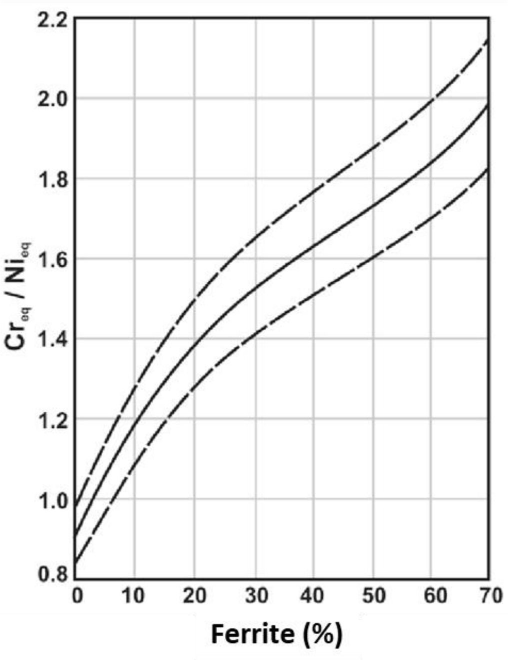

Figure 3: Schoefer diagram for estimating the Ferrite content on stainless steels. [15]

Regarding stainless steel, the δ-ferrite fraction is especially important, since this component has detrimental effects on several factors, such as high temperature workability, mechanical properties, and corrosion resistance. [16] The lack of cohesion between the surrounding matrix and the δ-ferrite grains can be considered the major reason for this deterioration of physical properties. [17] In addition, this secondary phase also introduces a ferromagnetic characteristic to the material, which causes even more restrictions regarding final applications. For instance, fatigue cracks initiated at the δ-ferrite and matrix interface are constantly reported in 304L stainless steels, leading the material to failure by crack propagation. [18]

The δ-ferrite chemical composition is significantly different when compared with the matrix of stainless steels, mostly in terms of Cr and Ni. For that reason, a compositional chromium and nickel variation with distance (δ-ferrite ↔ matrix) is expected. [18] Those differences can be associated with both the δ-ferrite and matrix (austenite, martensite) solubility coefficients. Since higher chromium contents are normally seen inside the δ-ferrite grains, a high solubility coefficient for this specific chemical element is associated with δ-ferrite. In contrast, this phase is characterized for exhibiting a lower nickel solubility, as lower nickel content is usually found on those grains. [19] Figure 4 shows the micro-composition across the δ-ferrite/austenite interface of a 304L austenitic stainless steel, representing a Cr and Ni variation along the measured distance.

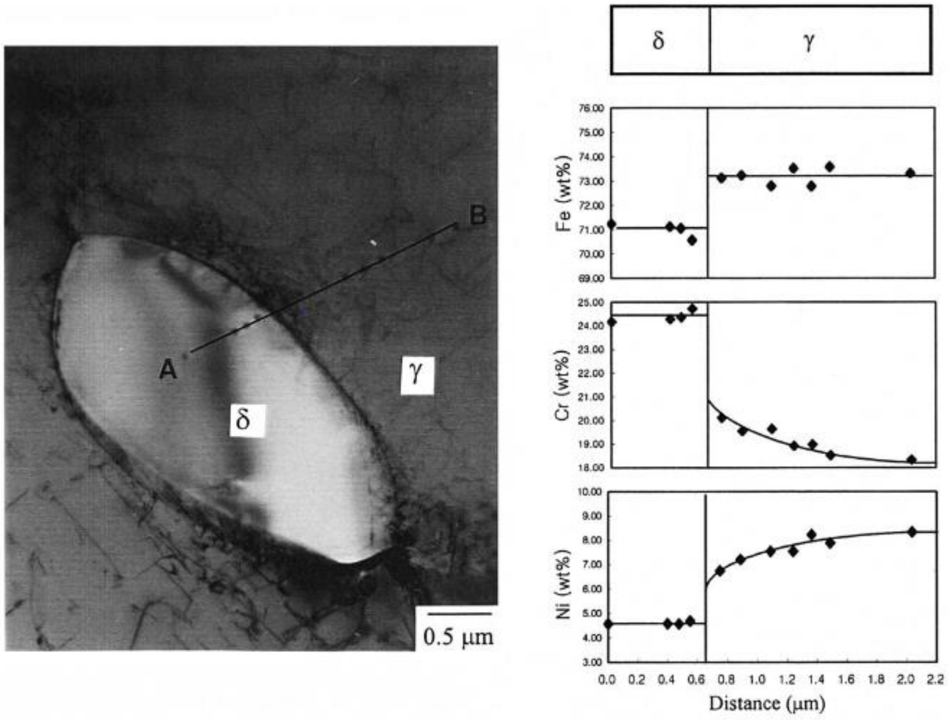

Figure 4: TEM micrograph and composition profiles along the δ/γ interface, showing Cr, Ni, and Fe compositional profile. [18]

2.2.1 Stereology of δ-ferrite

The morphology of δ-ferrite is primarily attached to the solidification path the material was submitted during processing. To elucidate this idea, the solidification of austenitic stainless steels after welding follows four solid-state transformation regimes, as demonstrated on Equations 2-3, 2-4, 2-5, and 2-6 [20] and represented on Figure 5.

Austenite mode (A): $L \rightarrow L + \gamma \rightarrow \gamma$ **Eq. 2-3**

Austenitic-Ferritic mode (AF): $L \rightarrow L + \gamma \rightarrow L + \gamma + \delta \rightarrow \gamma + \delta$ **Eq. 2-4**

Ferritic-Austenitic mode (FA): $L \rightarrow L + \delta \rightarrow L + \delta + \gamma \rightarrow \gamma + \delta \rightarrow \gamma$ **Eq. 2-5**

Ferrite mode (F): $L \rightarrow L + \delta \rightarrow \delta \rightarrow \delta + \gamma$ **Eq. 2-6**

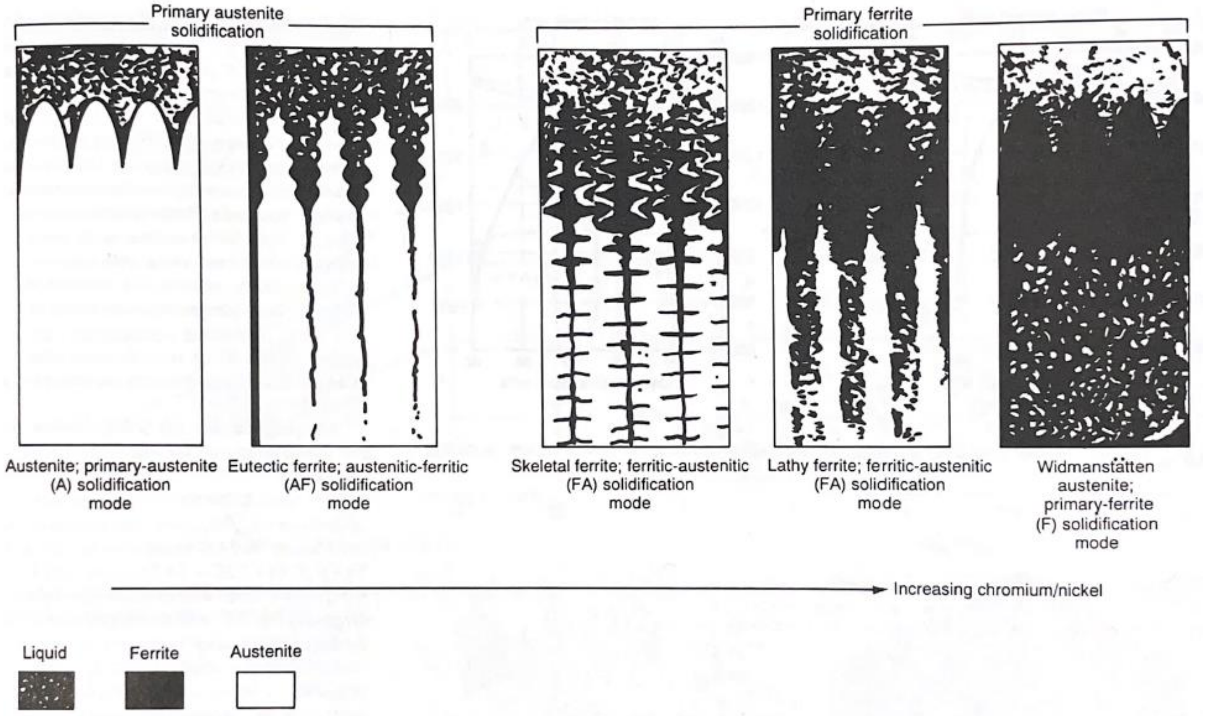

Figure 5: Schematics showing solidification and solid-state transformation behavior of welds, as Cr_{eq}/Ni_{eq} is increased. [5]

The A mode is represented by an enrichment in Cr and Ni at inter-dendritic regions. Differently, an enrichment in Cr occurs followed by a depletion in Ni content when the AF mode is analyzed. As the Cr_{eq}/Ni_{eq} ratio is increased (towards the FA and F regimes), a more accentuated enrichment in Cr is noted, while a stronger Ni decrease is observed at the inter-dendritic locations. Furthermore, for nucleating at those high Cr and low Ni areas, the δ-ferrite phase is known for containing high chromium and low nickel, as the segregation of Cr to ferrite and Ni to austenite stabilizes this phase. [21] Therefore, the initial δ-ferrite microstructural distribution is identified as vermicular, lathy, or acicular, depending on the heat treatment process and on the solidification rate. To elucidate, a three-dimensional micrograph demonstrates a δ-ferrite network, with connected grains, configuring a skeletal distribution. Figure 6 shows this microstructure.

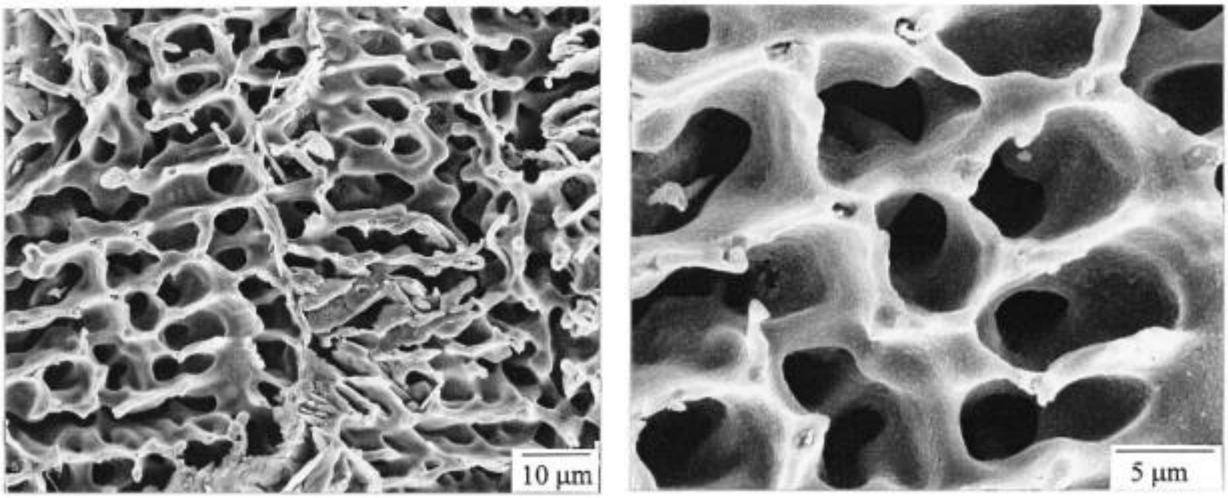

Figure 6: SEM micrograph of strip cast specimen showing three-dimensional δ-ferrite network. [18]

With the increasing of the Cr_{eq}/Ni_{eq} ratio, microstructures at room temperatures retain a significant amount of δ-ferrite, as exemplified on the above figure. Importantly, not only the composition influences the δ-ferrite stabilization at room temperatures, but also the solidification sequence and rate, or, in other words, processing and manufacturing conditions. [22]

2.2.2 Dissolution of δ-ferrite in Stainless Steels

As the δ-ferrite is mostly deleterious to stainless steels properties, diverse approaches are employed to alter this primary morphology. Different heat treatment designs combine time and temperature, aiming the fully dissolution of this phase. [23] Annealing time at certain high temperatures both dissolves and changes the δ-ferrite shape. The energy generated from the temperature act as homogenizing the microstructure, minimizing the chemical deviation matrix ↔ δ-ferrite. [24] Dissolution treatments are usually conducted at ranges between 1050°C and

1250°C. [22] In order to illustrate the dissolution of δ-ferrite taking place, in addition with morphological changes, Figure 7 shows the evolution of morphology of this phase when different annealing temperatures are adopted.

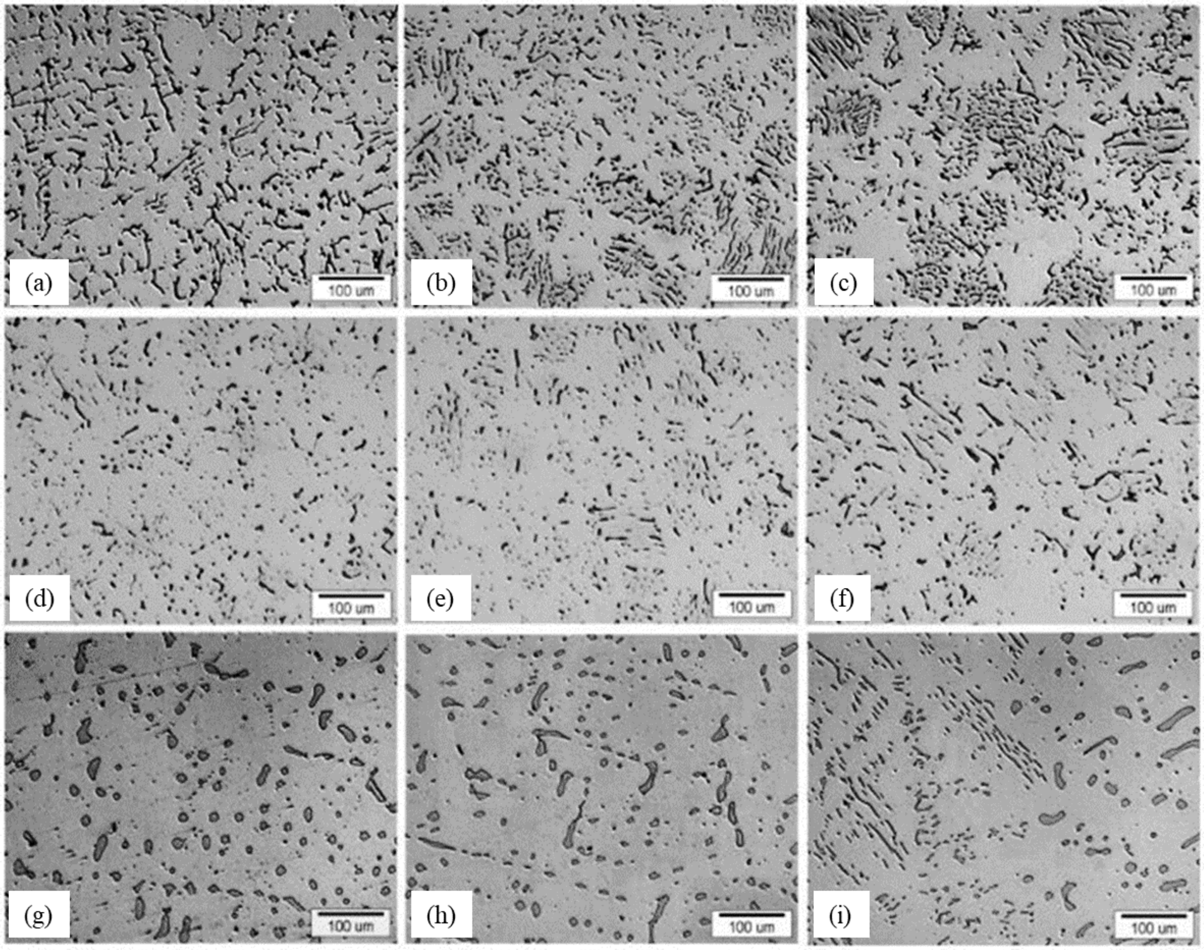

Figure 7: Evolution of morphology of δ-ferrite after 5 minutes of annelaing at (a-c) 1050°C, (d-f) 1150°C, and (g-i) 1250°C. [22]

Generally, elevated temperatures lead to the dissolution of the metastable δ-ferrite. As demonstrated on Figure 7, the δ-ferrite initial dendritic network tends to break down and spheroidize. Simultaneously, higher content of individual δ-ferrite islands appears in a more spherical shape, increasing the surface area δ-ferrite and matrix, and decreasing the interfacial energy along their boundaries. Those stereographical changes provide advantages in terms of crack initiation, which usually takes place at the δ-ferrite interfaces. [22]

Another approach for dissolving the δ-ferrite appears to be the adoption of post processing heat treatments after mechanical work. The introduction of deformation accommodates the grain boundary strain after cold working, and the afterwards application of temperature causes drastic reductions on the δ-ferrite phase fractions, due to the favorable transformation δ → γ. [23]

The δ-ferrite dissolution can be compared with the spheroidization of cementite, in high carbon steels. For those alloys, annealing treatments result in a microstructure of fine spherical cementite in a soft ferritic matrix, [25] which the morphological changes attributed to one of two different types, subcritical or inter-critical. [26]

- Subcritical spheroidization: this phenomenon is characterized by the cementite lamellae breaking up into spheres, in turn induced by the surface energy reduction, and happening below the A1 temperature. This model is usually adopted for hypoeutectoid steels.
- Intercritical spheroidization: the intercritical process happens above the A1 temperature, being applied for hypereutectoid steels. Instead of breaking the cementite lamellae, the spheroidization takes place partially dissolving the cementite grain boundaries.

Similar to the subcritical cementite spheroidization, the δ-ferrite dendritic morphology tends to break up and form round shaped grains. This phase morphology varies from vermicular, lacy, and acicular shapes to globular as the temperature and time are elevated, both critical parameters for diffusion processes. [27] Figure 8 compares a high carbon steel cementite spheroidization with an austenitc stainless steel that contains δ-ferrite on its microstructure. The carbon steel was annealed for 2 hours and slow cooled [27] while the stainless steel was subjected to a 60 second fast annealing heat treatment. [18]

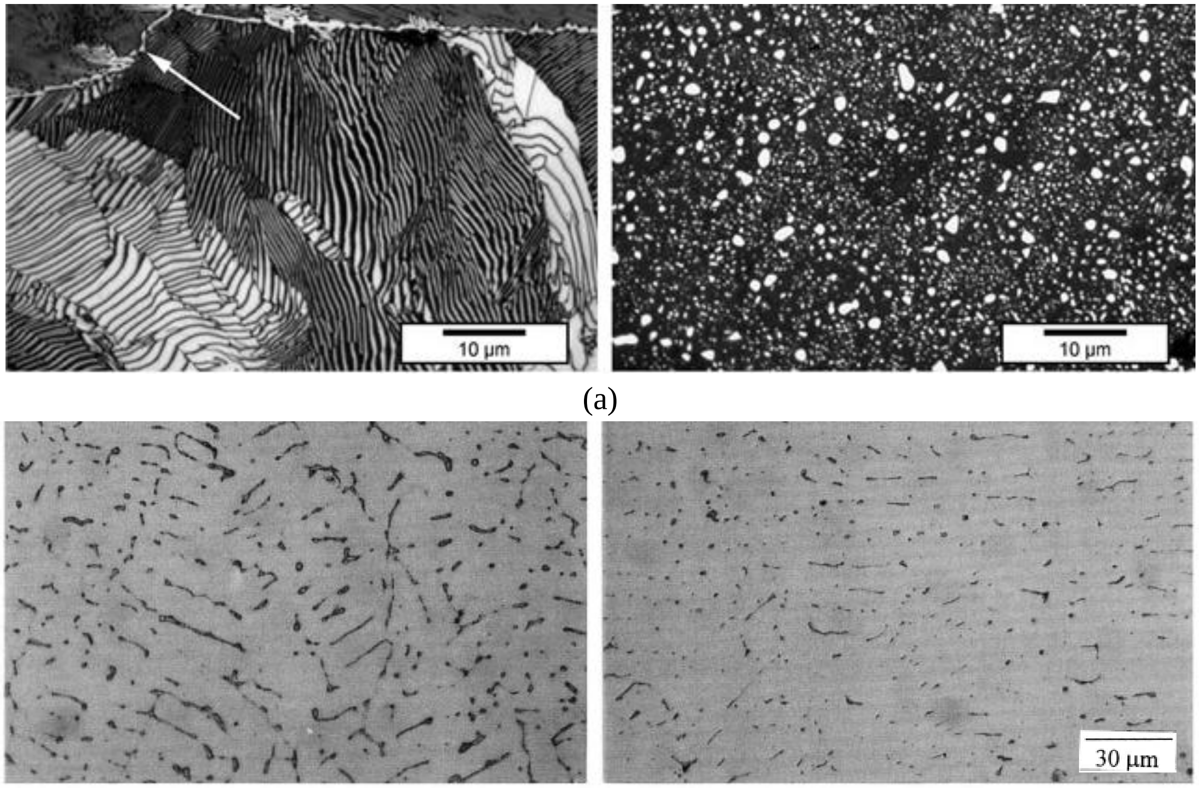

(a)

(b)

Figure 8: Optical micrographs showing the (a) cementite spheriodization, [27] and (b), the δ-ferrite morphological changes. [18]

Not only the area fraction and the morphology are modified while the dissolution of δ-ferrite is taking place, but the phase chemical composition changes as well. As well notably understood, the δ-ferrite presents higher chromium content within its phase, due to the solidification path ang higher Cr solubility. [21] Therefore, when a complete dissolution is assumed to happen, no chemical differences would be seen between the areas where δ-ferrite was present and the stainless steels matrix. For example, high annealing temperatures and times would act as favoring the diffusion and the microstructural homogenization, starting with the first solubilization of $M_{23}C_6$ carbides at lower temperatures (between 500 and 900°C). [28] The chemical homogenization is more accentuated as both the annealing temperatures and times are increased. In other words, the chemistry tends to assume similar values inside and outside the δ-ferrite grains as the δ-ferrite fraction decreases. [29] [30] According to Figure 9, as the annealing time escalates, the δ-ferrite and matrix chemical composition are approximated, while inducing dissolution.

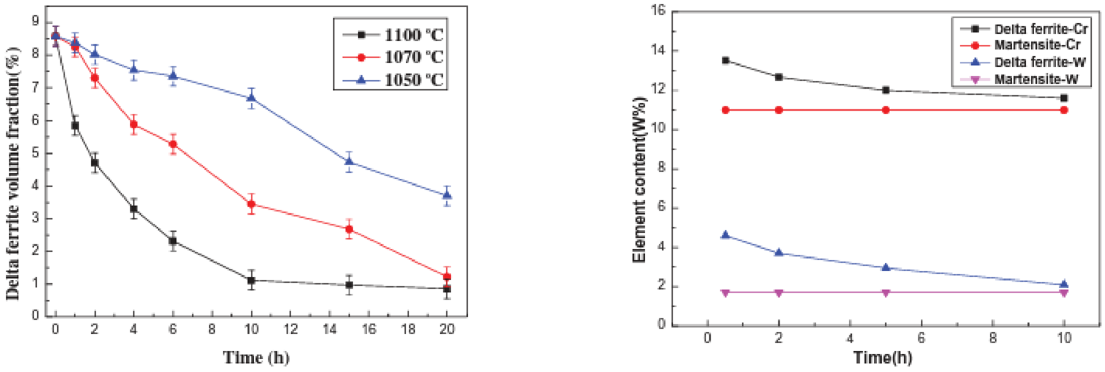

(a) (b)

Figure 9: (a) Variation in δ-ferrite fraction with annealing temperature and time; and (b) measurements of W and Cr content after annealing at 1100°C for different times. [29]

2.3 Dissolution Kinetics of δ-ferrite

As the δ-ferrite represents a significant problem during processing of stainless steels, this phase needs to be dissolved, targeting the increase in properties, such as tensile strength, fatigue and corrosion resistance. [31] [32] Morphological changes and chemical homogenization are common phenomena that take place during the dissolution of δ-ferrite. [28] Therefore, understanding the dissolution behavior of δ-ferrite implies also acknowledging the kinetics of dissolution of this phase.

The dissolution of δ-ferrite is usually reported to be divided in two stages. The early stage englobes a rapid dissolution of this phase, due to the first precipitation of $M_{23}C_6$ carbides along the δ-ferrite boundaries, at a temperature between 500 and 900°C. [33] At this range of temperatures, the δ-ferrite decomposes with the formation of those carbides, as seen on Figure 10.

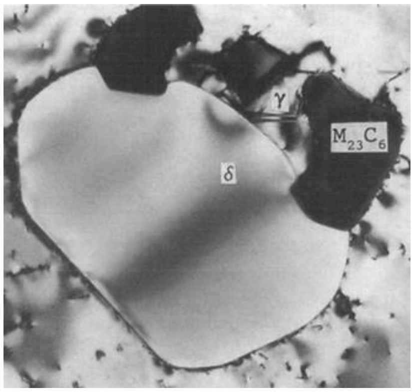

Figure 10: Bright-field TEM micrograph showing the decomposing δ-ferrite, for a material aged at 720°C for 10 hours. [33]

Once the temperature is further increased, the $M_{23}C_6$ carbides tend to dissolve along with the δ-ferrite grains. The energy from high temperatures drives this phase dissolution, inducing morphological changes by capillarity effect. An increase in roundness area of individual δ-ferrite grains is pursued by a decrease in volume fraction. Figure 11 shows the microstructural evolution of δ-ferrite dissolution during annealing at 1230°C.

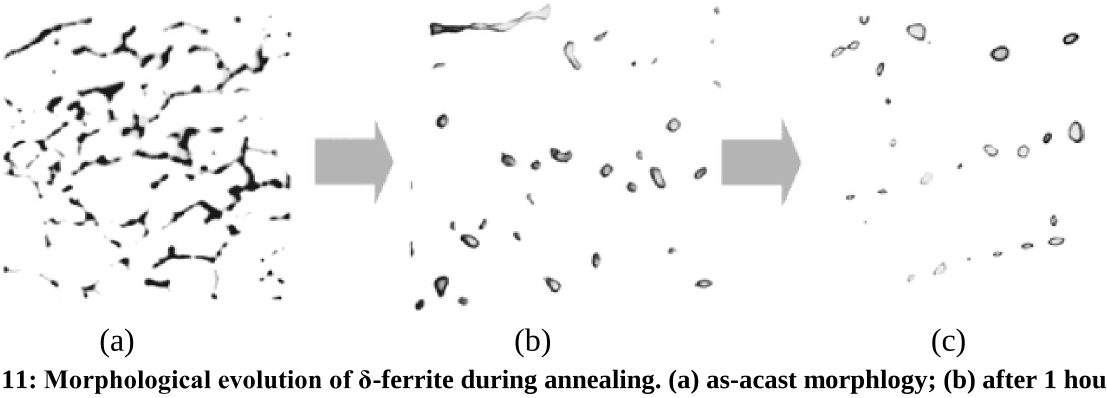
(a) (b) (c)

Figure 11: Morphological evolution of δ-ferrite during annealing. (a) as-acast morphlogy; (b) after 1 hour of annealing; and (c) after 1.5 hours of annealing. [34]

The dissolution process of δ-ferrite can be expressed accounting the variation in δ-ferrite fraction as the aging or annealing temperatures is changed, by using a pseudo-rate equation, seen on Equation 2-7. [35]

$$\frac{f}{f_0} = \mathrm{C} - b \log t \qquad \textbf{Eq. 2-7}$$

Where:

- f is the undissolved δ-ferrite content after a heat treatment at a temperature T during a time t.
- f_0 is the initial δ-ferrite content.
- b is a temperature dependent rate constant during the dissolution process; and
- C is the slope of the ordinate of the ${}^{f}/_{f_0}$ vs. $\log t$ plot.

The b constant is calculated and can be evaluated for each temperature, as it depends on this variable and obeys an Arrhenius expression, demonstrated on Equation 2-8. [35]

$$b = b_0 e^{\left(-\frac{Q}{RT}\right)} \qquad \textbf{Eq. 2-8}$$

Where:

- b_0 represents a pre-exponential factor.
- Q is the activation energy for the dissolution process.
- R is the gas constant; and
- T is the heat treatment temperature, in Kelvin.

The kinetics of the spheroidization process can be adapted to the δ-ferrite mechanism, as it considers a “rod-like” phase dissolution controlled by: 1) interface diffusion; 2) volume diffusion; 3) interface reaction; and/or 4) plastic flow. [36] This process is described by the Equation 2-9, below.

$$R^n = \alpha G t \qquad \textbf{Eq. 2-9}$$

Where:

- R is the radius of the rod (linearly dimensioned).
- α represents a geometric factor; and
- G is a constant depended on the appropriate transport mechanism.

With the δ-ferrite dissolution rising great interest on the optimization of stainless-steel processing, computational models are considered advantageous for increasing the effectiveness of heat treatments and other experimental techniques applied for this purpose. ThermoCalc is widely applied in the industry and one of its add-ons, DICTRA (Diffusion Controlled Transformations), is utilized as a one-dimensional simulation software for multicomponent alloys. [37] [38]

DICTRA was previously reported as a useful tool for the design of homogenization processes, predicting phase chemical compositional changes as a function of time or of distance. The kinetics of transformation could be predicted during cooling and solidification, targeting micro-segregation areas originated from those systems. [39]

3.0 Objective and Hypothesis

Objective:

The major objective of this project is to introduce a novel approach for increasing the dissolution kinetics of δ-ferrite. The combination of hot deformation experiments with post processing annealing heat treatments will act to reducing the total δ-ferrite dissolution time. As the conventional methods use long isothermal heat treatments, the synergistic combination of reheating temperature, deformation temperature, amount of deformation (ε) and strain rate (έ) will create more energized system, fastening the dissolution of this phase.

Hypothesis:

The complete dissolution of δ-ferrite can be achieved by long isothermal annealing heat treatments. Reducing the amount of time is essential for cost reduction and for increasing manufacturing effectiveness. Therefore, the introduction of a pre-annealing hot deformation step would promote a faster dissolution of δ-ferrite, as the diffusion path of this phase is significantly shortened with the energy prevenient from deformation. Favoring diffusion by compression will generate a more energized system, as not only time and temperature will drive the dissolution phenomenon, but the combination of time, temperature, strain rate, and amount of strain.

4.0 Experimental Procedure

Three stainless steel alloys, 15-5 PH, 154-M, and 304 L, were received from a sponsoring company, that manufactured each material with the purpose of producing steels which would exhibit a microstructure containing δ-ferrite. As the purpose of the present study, the δ-ferrite phase would be further investigated, allowing the understand about the response, in terms of formation and dissolution, of each alloy to conventional annealing heat treatments, additionally with hot compression experiments. Samples were received by the Ferrous Physical Metallurgy Group, at the University of Pittsburgh and sectioned from the forged pieces. Table 1 presents the chemical composition, as well with the stainless-steel grade, for each material, highlighting the some of the chemical elements present.

Table 1: Chemical Composition (.wt%) of the received samples

	C	**Mn**	**Si**	**Cr**	**Ni**	**Mo**	**Cu**	**N**
15-5	0.04	0.54	0.22	15.46	4.06	0.22	3.85	0.005
JET	0.13	0.72	0.20	11.50	2.80	1.72	0.17	0.017
304L	0.02	1.51	0.41	18.88	10.63	0.22	0.04	0.005

Since different stainless-steel grades were studied, the chemical composition varied substantially around Chromium, Nickel, Copper, and Carbon. As precipitation hardening, martensitic and austenitic stainless steels exhibit different chemistries, the formation/dissolution behavior of δ-ferrite is expected to be distinct among the three alloys. For this reason, each of the received materials was studied and further compared with regard to chemical composition variances.

The received stainless steels were sectioned and machined into coupons to be subjected to physical simulations, which in turn were divided in three stages:

1) Re-engineering of δ-ferrite: melting heat treatments consisted of heating up the materials to temperatures higher than 1400°C, adopting a slow cooling rate down to room temperatures. This experiment was conducted with the aid of a 30kW induction power system, capable of heating steel samples from room temperature up to 1500°C, at heating rates from 100 to 1000°C/s. The materials were encapsulated to avoid any interference of oxidation during the process. This first step was designed with the objective of creating δ-ferrite on the materials that had not exhibited any on the received/initial condition. Figure 12 shows the setup previously described, as well the samples before (4in long and 0.5in in diameter) and after (1.5in long and 0.8in in diameter) the re-melting process.

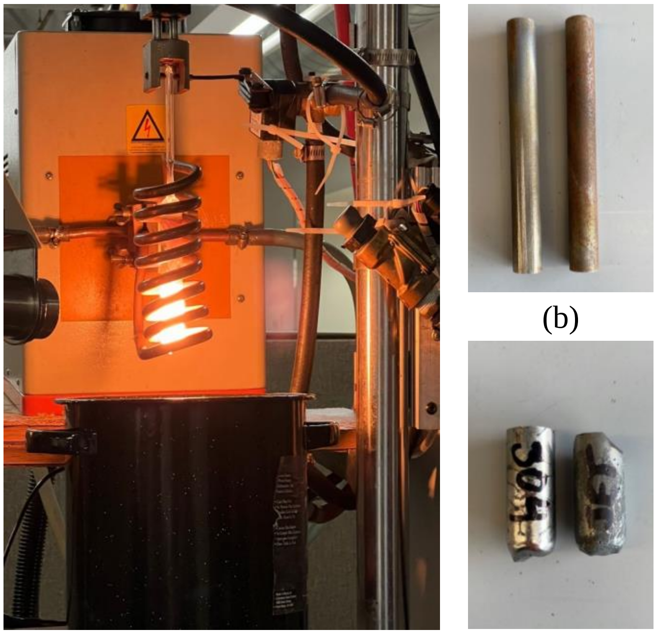

(b)

(a) (c)

Figure 12: (a) Induction heater setup; samples (b) before; and (c) after the melting process.

2) Conventional Annealing Heat Treatments: isothermal annealing heat treatments were outlined aiming the dissolution of δ-ferrite. Two different temperatures, 1000°C and

1150°C, were combined with three distinct holding times, 1 hour, 2 hours, and 3 hours, with the δ-ferrite area fraction analyzed after each condition. Those treatments were done by using a Three Zone Tube Furnace (*LINDBERG CC58434C*), with all the samples encapsulated to prevent oxidation. After holding the steels at a high temperature, all samples were air cooled down to room temperature. Figure 13 shows the utilized conventional heat treatment approach.

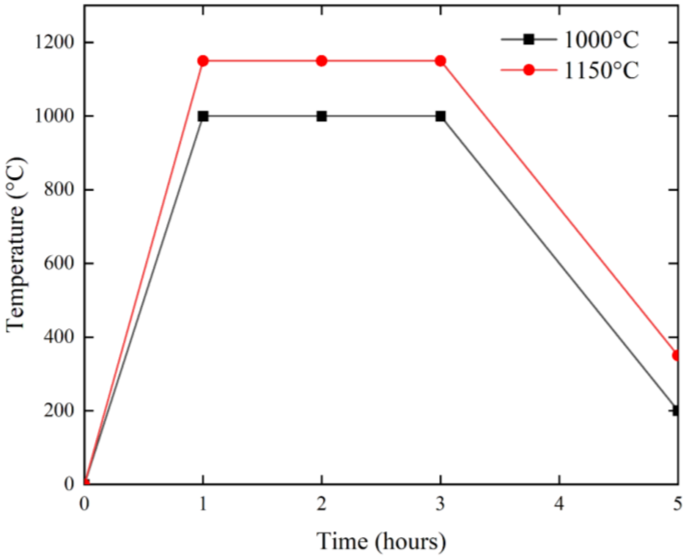

Figure 13: Proposed Annealing Heat Treatment Design

3) Hot Compression Experiments: tests were performed with the aid of a Universal Testing Machine (*1000HDX INSTRON*) adapted with an infrared furnace (*Chamb IR-E4-D-01-A*), in turn equipped with four 1000W lamps. The hot compression system is equipped with tungsten carbide dies, which have high strength at high temperatures. Prior to testing the dies were heated up to the deformation temperature. Subsequently, the sample was placed between the dies, and immediately deformed. Three different strain rates were chosen, 0.1/s, 1/s, and 10/s, and a fixed amount of deformation, 60%, was applied. After compression, the specimens were subjected to a post processing

isothermal heat treatment, with the aid of a muffle furnace (*Thermo Scientific Thermolyne FB1315M*), for 10 minutes, and then air cooled. The adopted post processing temperatures were selected as the same as the ones used during conventional annealing (1000°C and 1150°C). Figure 14 exhibits the hot compression design, highlighting the compression temperature of 900°C, in addition with the adopted two post processing temperatures.

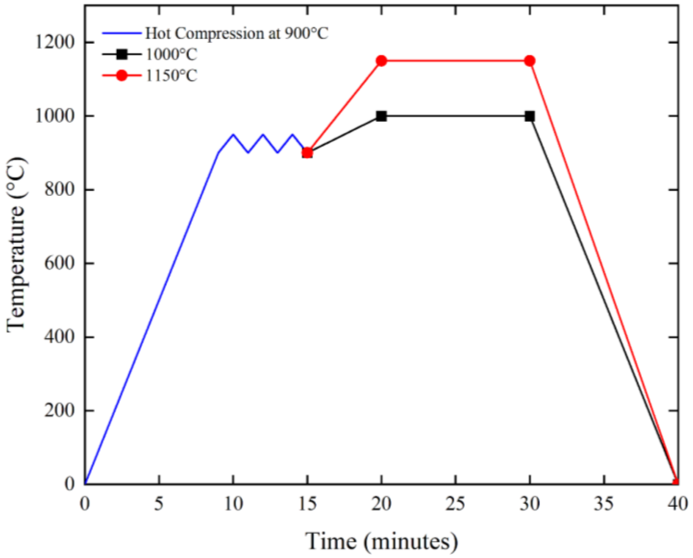

Figure 14: Proposed Hot Compression Experimental Design

After submitting to all physical simulation and prior to any microstructural characterization, the samples were prepared following standard metallographic procedures. Specimen were mounted in a 1.5” mount using conductive Cu-powder (*Struers CitoPress Mounting*) and submitted to manual grinding using papers from 120 to 1200 grit. After abrasive grinding, samples were manually polished for 5 minutes using a 0.5 µm alumina suspension followed by a mechanical vibratory polisher (*Giga-S 0900*) for 1 hour using a 0.05 µm deagglomerated alumina solution, to improve the surface quality.

Subsequently, each of the alloys were chemically etched using different solutions, to better revealing the δ-ferrite phase. The 15-5 PH steel was etched with Murakami's Reagent (*10g of Potassium Ferricyanide, 10g of NaOH, and 100mL of DI Water*), the M-154 was etched with Villela's Reagent (*1g of Picric Acid, 5mL of HCl, and100mL of ethanol*), and the microstructure of the 304 L material was revealed by using an electro-etching solution composed by 10% Oxalic Acid in DI Water, at 15V dc current. Images of the etched surfaces were acquired with the aid of a digital optical microscope (*Zeiss Smartzoom*), and then later processed using the free software ImageJ, where the δ-ferrite morphology and area fraction were assessed by color thresholding.

Further compositional analysis of the phases was conducted using an Electron Probe Microanalyzer (EPMA) (*Jeol JXA-8530F Field Emission Probe Microanalyzer*) to quantify the chemical deviations between the δ-ferrite and the matrix of each steel. All chemical analyses were carried out using a 20kV beam at a probe current of 100nA, proceeding with the line-scan feature for data asset. Thermodynamic calculations were done with the aid of Thermo-Calc software, equipped with the Diffusion (DICTRA) Add-on Module. 500 points were acquired in a compositional line-scan, with the chemical data regarding the three received samples, 15-5 PH, M-154, and 304 L, was employed as an input for the succeeding calculations and predictions done by the software. Assuming a homogenized system, the total δ-ferrite dissolution time after isothermal heat treatments could be predicted and simulated. Figure 15 illustrates the procedure utilized, additionally with the technique implied during Scanning Electron Microscopy (SEM) and Energy Dispersive Spectroscopy (EDS) *(Zeiss Sigma 500VP Field Emission Gun/Oxford Aztec ESD Detector)* data acquisition at 20kV.

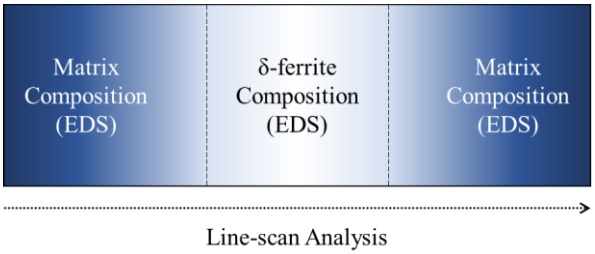

Figure 15: Schematic of the setup utilized for estimating the dissolution time of δ-ferrite

5.0 Results and Discussion

As the objective of the present study was to create an understanding about the formation and dissolution of δ-ferrite, the microstructural characterization of this microconstituent was conducted focusing on area fraction measurements and on matrix and δ-ferrite chemical composition deviations. All the microstructural conditions, after conventional annealing treatments and hot compression experiments, were studied and compared. Therefore, in order to fulfil and complete the suggested examination, Optical Microscopy, Scanning Electron Microscopy, and Electron Probe Micro-analysis were conducted. At the first level of characterization, Optical Microscopy was used to evaluate the overall microstructures of each alloy after all the proposed physical simulations. In addition, area fraction measurements were assessed after analyzing low magnification images, where a better picture about both δ-ferrite morphology and fraction could be acknowledged. On a more advanced level of characterization, SEM/EDS and EPMA techniques were implied to evaluate chemical composition changes and differences after each studied condition.

5.1 Microstructural Characterization

5.1.1 15-5PH Stainless Steel

The 15-5 Precipitation-Hardened Stainless Steel was etched with Murakami's Reagent, having the microstructure revealed by coloring the martensitic matrix in dark colors, while the δ-ferrite phases were shaded in lighter colors. Figure 16 shows a micrograph of the as-received 15-5PH steel.

Figure 16: Optical microscopy showing the 15-5PH as-received microstructure.

On this specific alloy, characterized right after being received, the δ-ferrite grains appeared with very elongated and continuous morphology. As expected, the δ-ferrite continuity would be changed to round-shaped grains with the increase of annealing time and temperature, factors that favor dissolution. Figure 17 shows a schematic of the δ-ferrite stereology as the annealing times and/or temperatures are increased. The characteristic δ-ferrite morphology is altered by capillarity effect, where the very elongated grains are divided, approximating into round grains. [40]

(a) (b) (c) (d)

Figure 17: Schematics showing the 15-5PH δ-ferrite phase morphology evolution - (a) to (d) - after annealing.

Before studying the dissolution behavior of δ-ferrite, simple EDS characterization was conducted to assess this phase chemical composition. As is well known, the δ-ferrite has a characteristic of exhibiting high Chromium contents. [41] Figure 18 exemplifies this behavior, with the shaded areas representing the δ-ferrite grain.

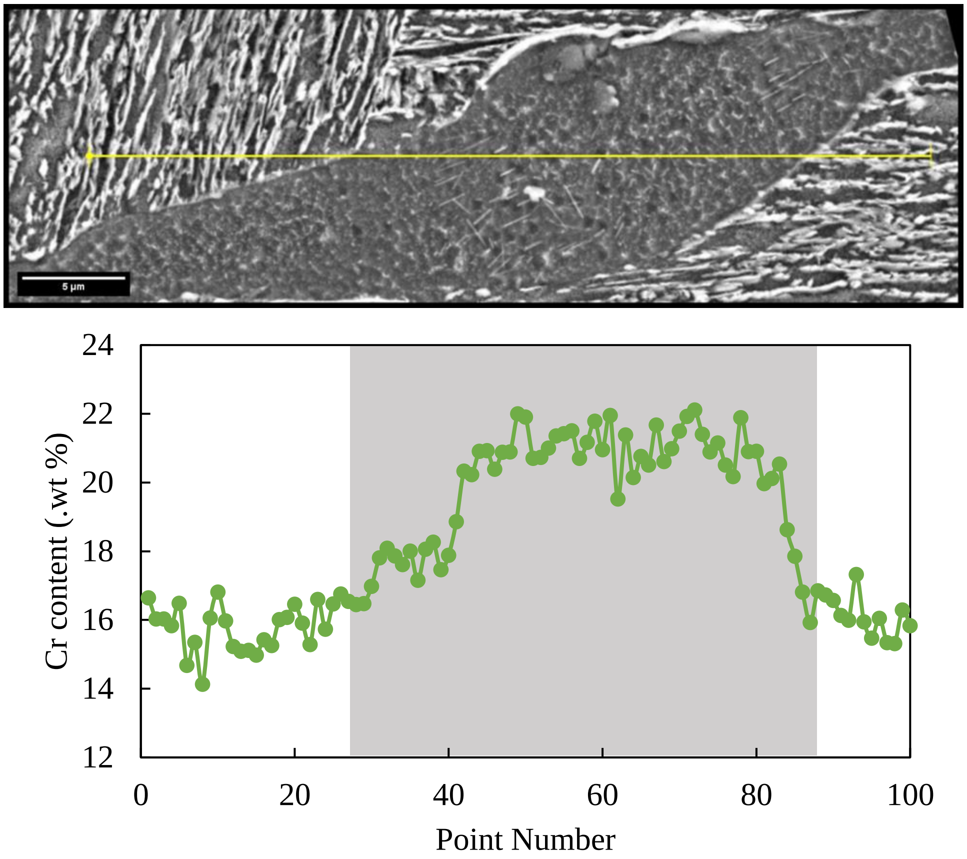

Figure 18: EDS analysis of the 15-5PH as-received sample.

After corroborating that the as-received sample presented δ-ferrite, and to observe the stereological and fraction changes of this microconstituent, annealing heat treatments were performed. As can be observed on Figure 19, after heat treating the material at 1000°C and adopting different holding times, two main attributes can be observed: the δ-ferrite decreasing fraction, while changing morphology into round grains.

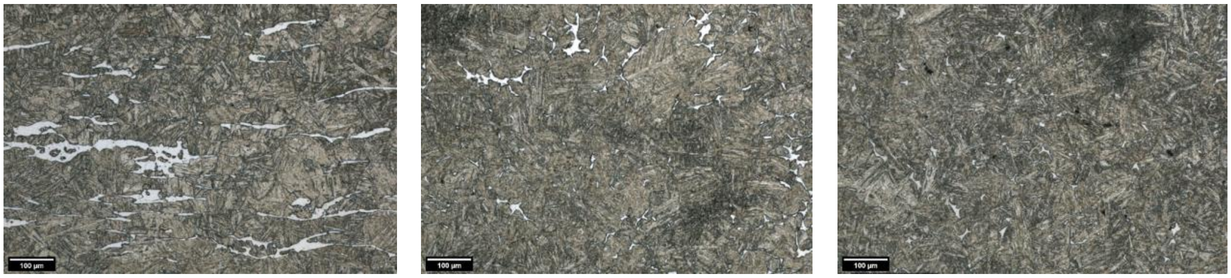

(a) (b) (c)

Figure 19: Optical microscopy of the 15-5PH steel after annealing at 1000°C, for (a) 1h, (b) 2h, and (c) 3h.

Those two points suggest the dissolution kinetics of δ-ferrite taking place as the annealing time is increased. A similar trend could be noticed for the samples treated at 1150°C for 1, 2, and 3 hours. Although, since the annealing temperature was higher, the dissolution kinetics of δ-ferrite was expected to be more accentuated. [22] Therefore, both the morphological changes and the area fraction reduction were more drastically stimulated. Figure 20 shows the resulting micrographs after annealing at 1150°C for different holding times.

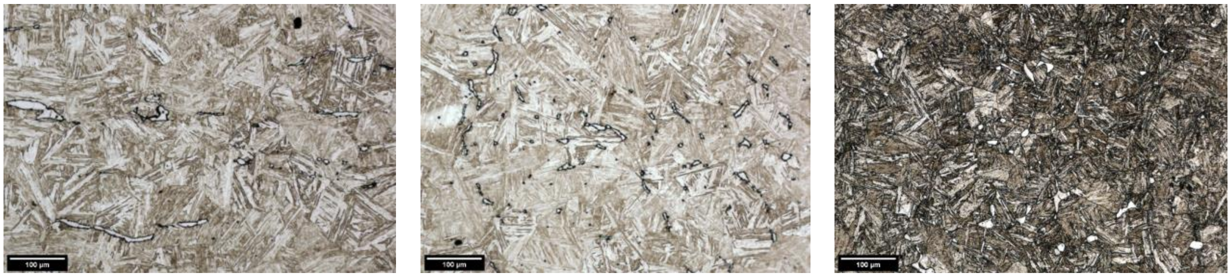

(a) (b) (c)

Figure 20: Optical microscopy of the 15-5PH steel after annealing at 1150°C, for (a) 1h, (b) 2h, and (c) 3h.

Area fraction measurements, comparing the behavior after annealing at 1000°C and 1150°C for different times, helped understanding about the dissolution kinetics of δ-ferrite. With those measurements, the influence of annealing temperature and time could be studied, while the most efficient approach on fully dissolving this secondary phase was understood. At this level of characterization, the area fraction was the primary parameter utilized, where simple one assumption was made: lower fraction of δ-ferrite would impose higher dissolution rates previously acting in the system. Figure 21 represents the area fraction acquired after color thresholding each individual micrograph. The material was received with close to 3% of δ-ferrite, and when he most extreme condition was analyzed, i.e., after 3 hours at 1150°C, this number was decreased to 0.6%.

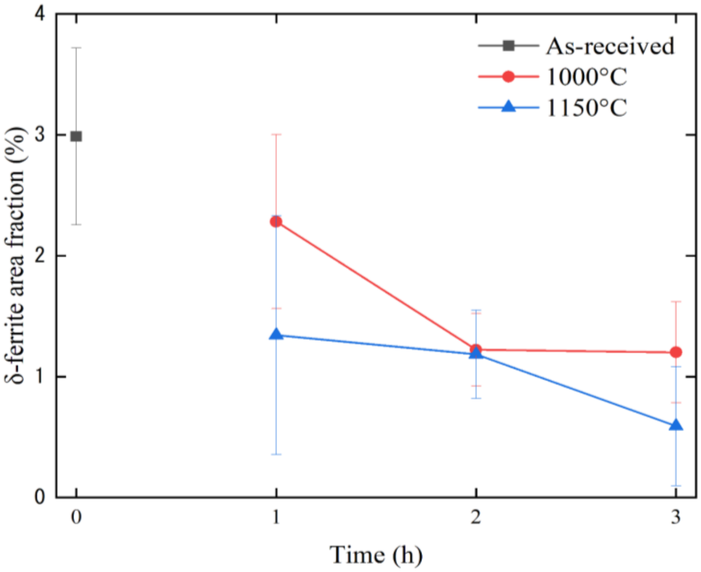

Figure 21: 15-5PH area fraction measurements after conventional annealing treatments.

As a matter of comparison, the annealing time of 2 hours was selected to underline the changes in stereology of δ-ferrite. At this condition, the area fraction was roughly similar for both samples, but more round grains could be seen after 1150°C. Figure 22 shows this example. As indicated before, the dissolution of δ-ferrite was faster after heat treating the material at a higher temperature. The energy offered by temperature promoted a shorter diffusion path, and induced dissolution.

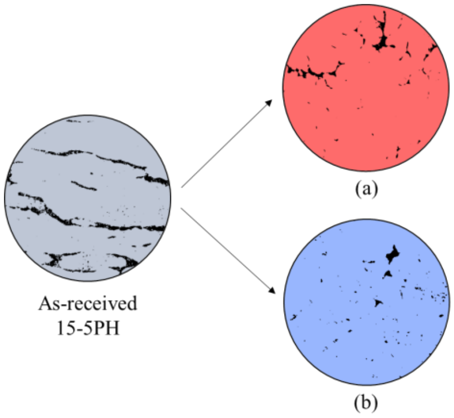

Figure 22: Comparisons of the 15-5PH samples treated at (a) 1000°C and (b) 1150°C, both for 2 hours.

After annealing, the dissolution behavior of δ-ferrite was studied after hot compression experiments. With this approach, the influence of deformation and strain rate, in addition with time and temperature could be accounted. The dissolution kinetics of δ-ferrite was expected to be increased with the introduction of deformation into the system. Assuming the diffusion path to be further decreased by the combination of strain rate and deformation, the dissolution kinetics of the system would be escalated. Figure 23 presents the material at compressed under three different strain rates and post heat treated at 1000°C for 10 minutes.

(a) (b) (c)

Figure 23: Optical microscopy of the 15-5PH steel after hot compression and post processing at 1000°C, at (a) 0.1/s, (b) 1/s, and (c) 10/s strain rates.

Clearly, the addition of deformation to the system increased even more the dissolution kinetics of δ-ferrite. The fact that more round grains were seen corroborates with the previous affirmation. Furthermore, an annealing time of 10 minutes was sufficient for dissolving the phase in a more accentuated intensity than after conventional heat treatments. Likewise, a post compression temperature of 1150°C generated samples following a similar tendency and Figure 24 exhibits the micrographs regarding the steel post processed at this temperature for 10 minutes, again under the same three strain rates: 0.1/s, 1/s, and 10/s.

(a) (b) (c)

Figure 24: Optical microscopy of the 15-5PH steel after hot compression and post processing at 1150°C, at (a) 0.1/s, (b) 1/s, and (c) 10/s strain rates.

A similar behavior was noticed after hot compression and post processing at 1150°C; however, the change in morphology seems to be more associated to the deformation process, as the δ-ferrite grains appeared to be more deformed and elongated. Area fraction measurements observed on Figure 25 show a reduction from values close to 3%, in the as-received material, to less than 1% for the hot compressed and annealed alloys.

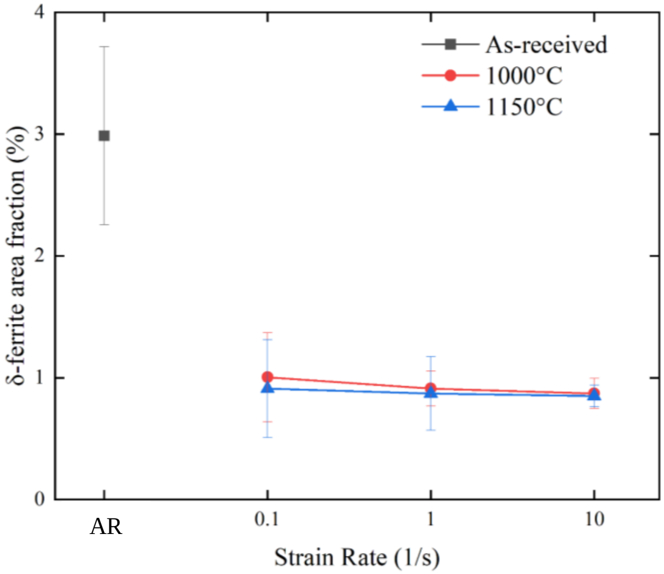

Figure 25: 15-5PH area fraction measurements after hot compression experiments.

Although the percentage of δ-ferrite remained within the standard deviation for all studied conditions, slightly lower fractions were calculated after 1150°C. Analyzing the strain rate, even less influence was observed. For both evaluated temperatures, the fractions ranged from a maximum value of 1% to a minimum of 0.85%, representing only a 0.15% difference between the two opposite hot compression states. The strain rate of 10/s was selected to underline the changes stereology of δ-ferrite. As observed before, and throughout the whole experimental design, the area fraction was roughly similar after compression, not substantially varying with different strain rates, and neither with different post processing temperatures, indicating a stronger influence of the annealing time to promote the dissolution. Figure 26 shows this example.

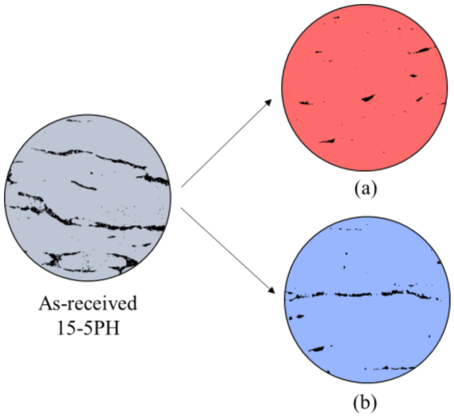

Figure 26: Comparisons of the 15-5PH samples post heat treated at (a) 1000°C and (b) 1150°C, after compressed under 10/s strain rate.

Figure 27 demonstrate the measured area fraction values for all the conditions studied. What was highlighted in the previous paragraphs are graphically seen after annealing and hot compression. The decrease in δ-ferrite fraction is noticeable after hot compression, as the percentage of this phase reached lower levels after 10 minutes of annealing.

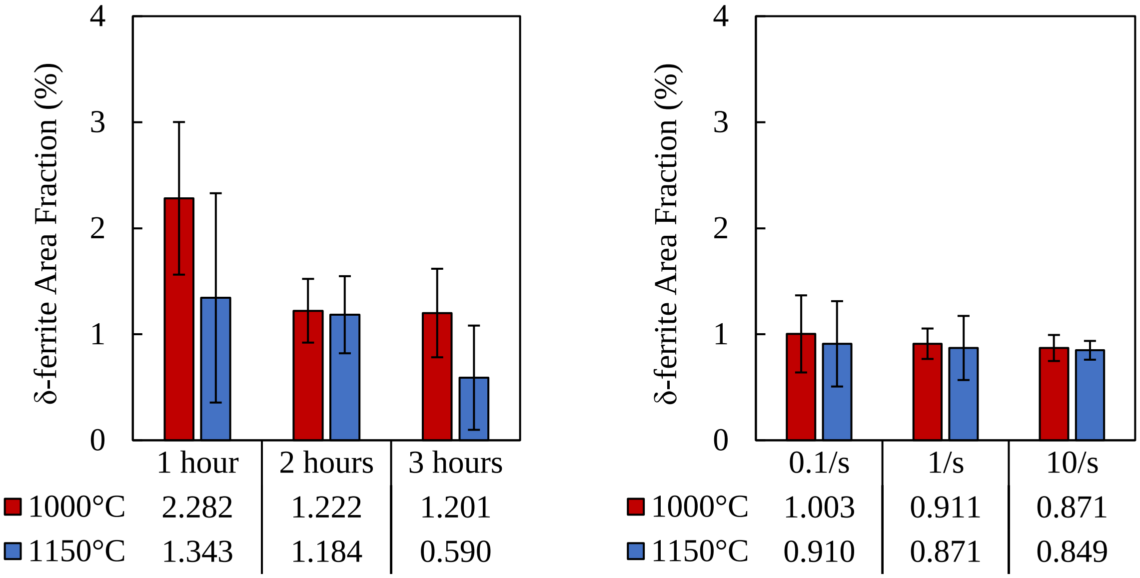

(a) (b)

Figure 27: 15-5PH area fraction measurements after (a) conventional annealing treatments, and (b) hot compression experiments.

5.1.2 M-154 Jethete Stainless Steel

The Jethete martensitic stainless steel (JET) was etched with modified Villela's reagent for revealing the δ-ferrite grains along with the material matrix; however, no δ-ferrite was observed. Figure 28 presents the Jethete alloy showing a martensitic matrix, with no apparent secondary phases on the as-received material.

Figure 28: Optical microscopy showing the JET as-received microstructure.

The Jethete steel was re-melted aiming the formation/creation of δ-ferrite at temperatures higher than 1400°C, and subsequently slow cooled to room temperature. Except for this extra step, the JET alloy was also subjected to conventional annealing treatments and to hot compression experiments. The microstructure of the re-melted Jethete material can be visualized on Figure 29.

Figure 29: Optical microscopy showing the JET microstructure after melting.

Differently from the as-received condition, after the re-engineering processing, the δ-ferrite, was etched in dark colors and appeared decorating the prior austenite grain boundaries. Higher energized regions, such as grain boundaries, acted as nucleation sites for the δ-ferrite after melting, promoting the precipitation of this constituent on those areas. [42] EDS characterization was adopted to confirm the presence of this phase, and Figure 30 shows this analysis. An expected enrichment in Chromium could be observed in the δ-ferrite rich regions.

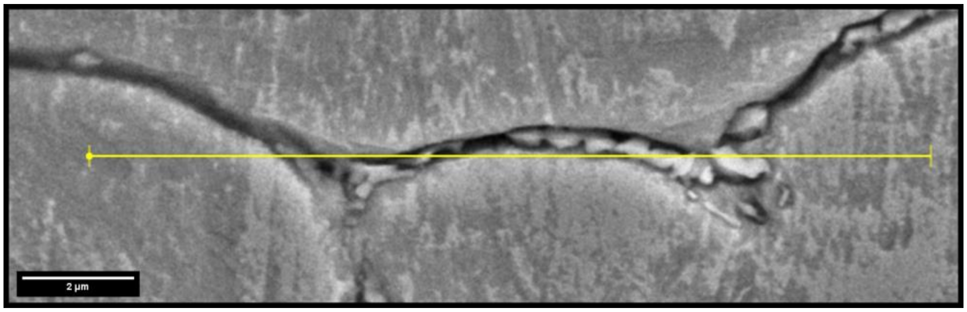

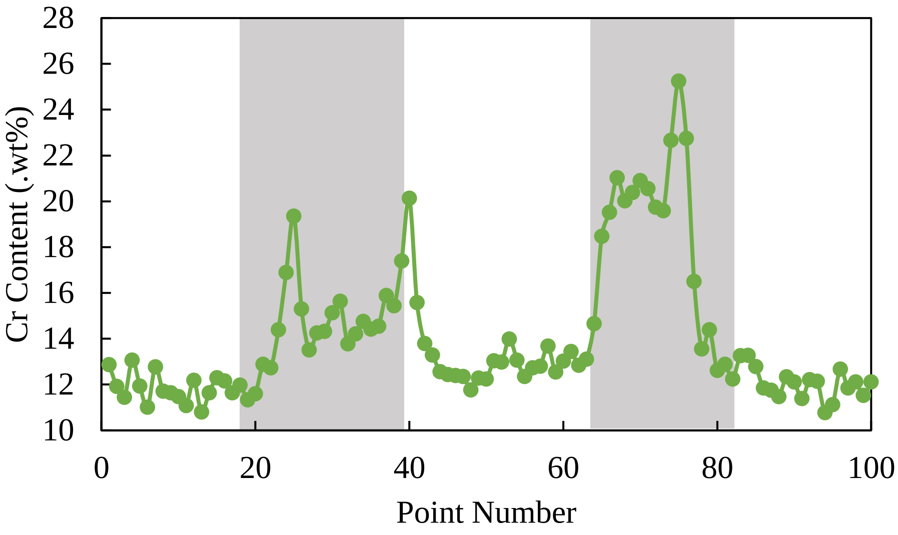

Figure 30: EDS analysis of the JET as-melted sample.

With the formation of δ-ferrite, the dissolution behavior could be forward studied. To accomplish that, continuous annealing treatments and hot deformation experiments were selected. The δ-ferrite morphology was expected be changed after those processes, by transforming its continuity, as smaller and more round grains appear. [34] Figure 31 shows a schematic representation of the δ-ferrite microstructural evolution after annealing, for this specific alloy.

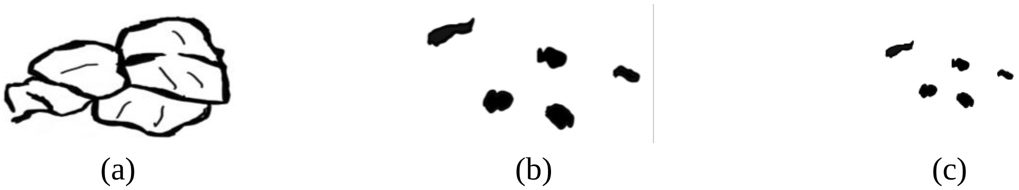
(a) (b) (c)

Figure 31: Schematics showing the JET δ-ferrite phase morphology evolution - (a) to (c) - after annealing.

Corroborating the schematics, the experimental results after annealing show the same trend. The δ-ferrite grains, once decorating the prior austenite grain boundaries, appeared randomly distributed in small and round grains. Figure 32 shows the alloy treated at 1000°C, for different times. As exemplified before, the δ-ferrite area fraction was reduced as the annealing time was increased. The capillarity effect for this steel is apparently stronger than what was observed for the 15-5 PH material, since the round δ-ferrite grains were found at the early stages of annealing.

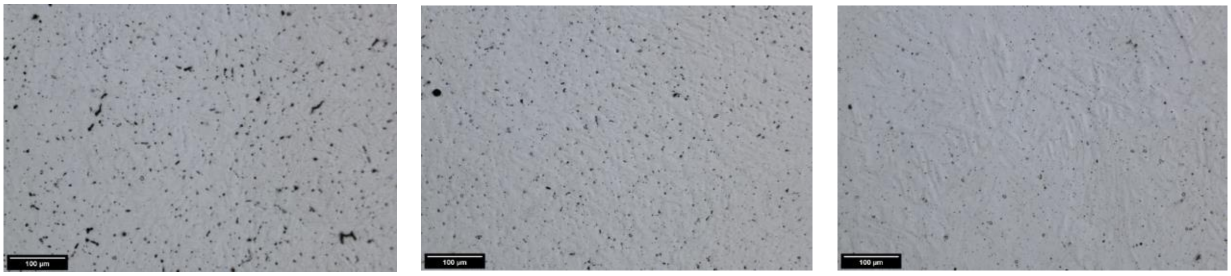
(a) (b) (c)

Figure 32: Optical microscopy of the JET steel after annealing at 1000°C, for (a) 1h, (b) 2h, and (c) 3h.

Correspondingly, the samples treated at 1150°C for 1, 2, and 3 hours also followed the same tendency, differing by the number of δ-ferrite grains after each stage of annealing. This difference can be explained by the higher annealing temperature, which speeded the dissolution kinetics up. The resulting micrographs after annealing at 1150°C for different holding times can be observed on Figure 33.

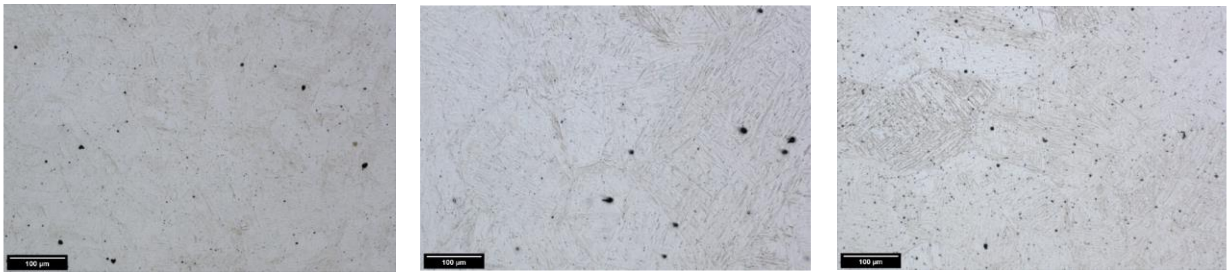
(a) (b) (c)

Figure 33: Optical microscopy of the JET steel after annealing at 1150°C, for (a) 1h, (b) 2h, and (c) 3h.

The area fraction was utilized to conclude about which system promoted the faster dissolution of δ-ferrite, considering the variables time and temperature. Lower fractions of δ-ferrite imply higher dissolution rates. Comparing the annealing behavior at 1000°C and 1150°C, after different soaking times, it is clear that the higher temperature promoted a faster dissolution rate, as lower δ-ferrite percentages were observed. In addition, considering all sample's conditions, both two temperatures and three times, a decrease in area fraction was also noticeable. The re-melted material showed 13% of δ-ferrite, and when the most extreme condition was analyzed, i.e., after 3 hours at 1150°C, this number was decreased to 1.2%. All measurements, conducted by color thresholding each δ-ferrite grain, are introduced on Figure 34.

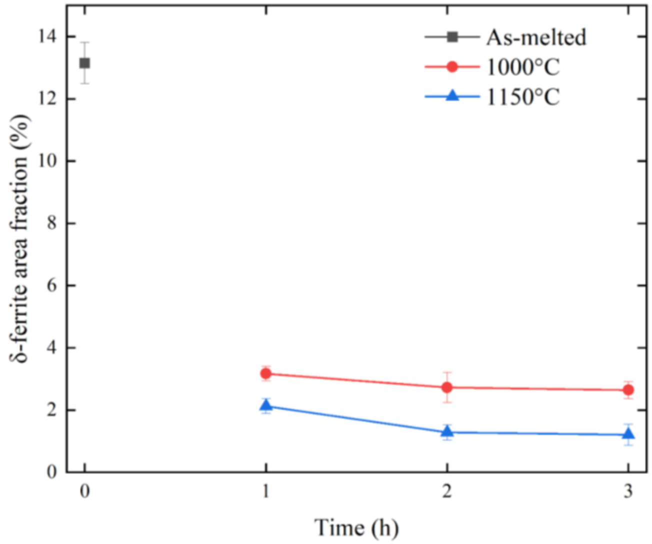

Figure 34: JET area fraction measurements after conventional annealing treatments.

In order to compare the schematics of Figure 31 to what was measured after this experimental approach, the annealing time of 2 hours was selected to underline the changes in stereology of δ-ferrite, for the Jethete alloy. At this condition, the sample treated at 1150°C showed lower area fraction values, as the studied microconstituent appeared distributed in smaller grains. Figure 35 shows this example. As indicated before for the 15-5PH material, the dissolution of δ-ferrite is faster after heat treating the material at a higher temperature, which in turn offers a higher energy to the system, promoting a shorter diffusion/dissolution path.

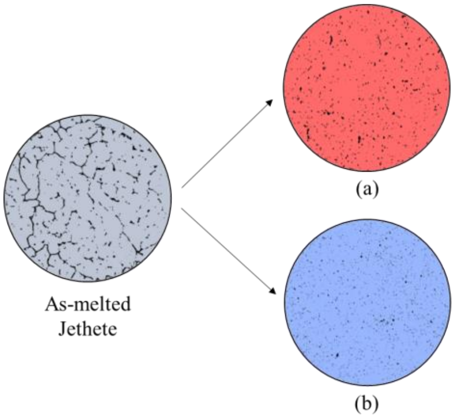

Figure 35: Comparisons of the JET samples treated at (a) 1000°C and (b) 1150°C, both for 2 hours.

As proposed, after the annealing stage, the Jethete steel was studied posteriorly to hot compression experiments. Theoretically, when introducing deformation to the system, the dissolution velocity is likely to be increased, since not only time and temperature are acting to decrease the diffusion path of δ-ferrite, but also strain rate and deformation. Figure 36 shows the micrographs of the Jethete steel after compression, and post processing annealing at 1000°C. Three different strain rates were adopted: 0.1/s, 1/s, and 10/s.

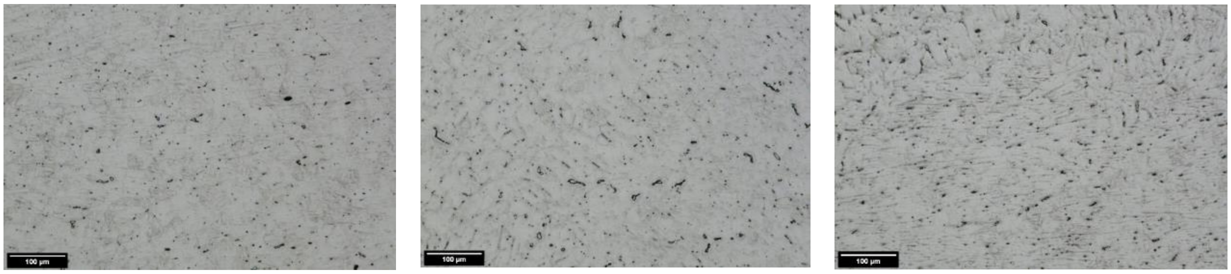

(a) (b) (c)

Figure 36: Optical microscopy of the JET steel after hot compression and post processing at 1000°C, at (a) 0.1/s, (b) 1/s, and (c) 10/s strain rates.

As the adoption of deformation possibly increased the dissolution kinetics of the system, comparable fractions of δ-ferrite were observed after hot compression. At this stage, not very small grains were observed, although they presented a dispersed distribution throughout the samples. The combination of these two factors contributed to the decrease in δ-ferrite area fraction, as 10 minutes of annealing presented as sufficient to considerably dissolve this phase. As seen on Figure 37, a similar behavior was noticed after analyzing the sample post treated at 1150°C. The micrographs regarding this treatment condition can be seen below.

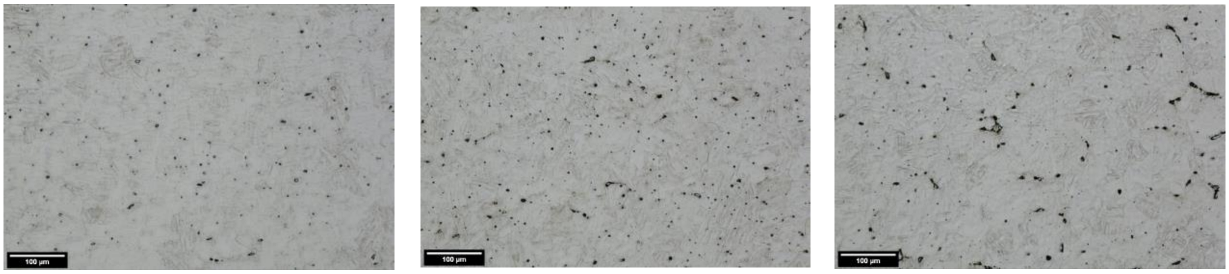

(a) (b) (c)

Figure 37: Optical microscopy of the JET steel after hot compression and post processing at 1150°C, at (a) 0.1/s, (b) 1/s, and (c) 10/s strain rates.

With the increase in strain rate, no significant decrease of δ-ferrite was observed. In conclusion, the strain rate range used in this study does not seem to influence the dissolution kinetics of δ-ferrite as much as the annealing times. However, the combination of deformation, strain rate and deformation temperature certainly increased the dissolution velocity of δ-ferrite, as lower percentages were observed after 10 minutes of post processing heat treatments. Figure 38 shows the area fraction measurements after hot compression experiments.

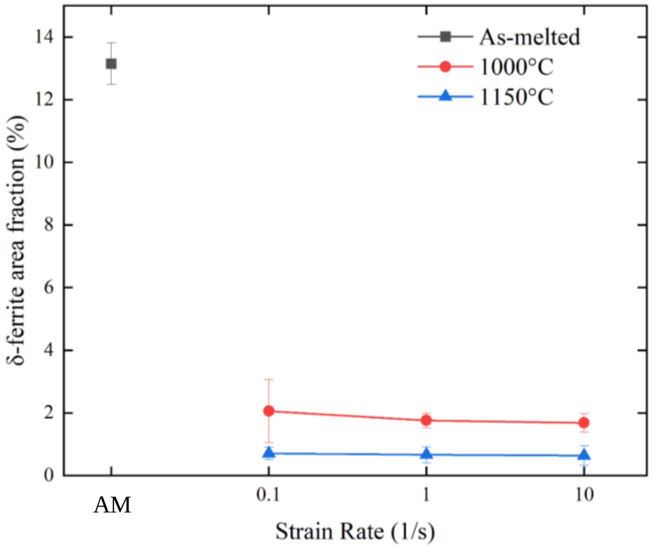

Figure 38: JET area fraction measurements after hot compression experiments.

The δ-ferrite fraction slightly decreased with the increase in stain rate, maintaining within the standard deviation of one another, for both temperatures. However, no significant changes could be noticed as the strain rate was changed. Therefore, the effect of deformation could have been more accentuated on the dissolution if longer annealing times were adopted during the post processing treatments, since the holding time of 10 minutes was not enough to promote a more perceptible difference for each strain rate. Figure 39 compares both specimens compressed under a 10/s strain rate, regarding phase morphology and distribution. The adoption of a higher post compression annealing temperature generated samples with different δ-ferrite morphologies, as a vermicular distribution can be seen at the material post processed at 1000°C, while the alloy post processed at 1150°C had this distribution disappeared, with rounder δ-ferrite grains observed.

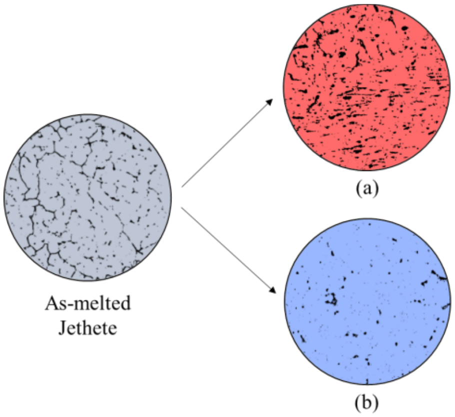

Figure 39: Comparisons of the JET samples post heat treated at (a) 1000°C and (b) 1150°C, after compressed under 10/s strain rate.

Figure 40 shows a comparison of the δ-ferrite area fractions after conventional and hot compression treatments. A decrease in δ-ferrite with the increase of the annealing temperatures and times was noticed after conventional heat treatments. On the other hand, the two different adopted post deformation temperatures kept the δ-ferrite fraction roughly constant.

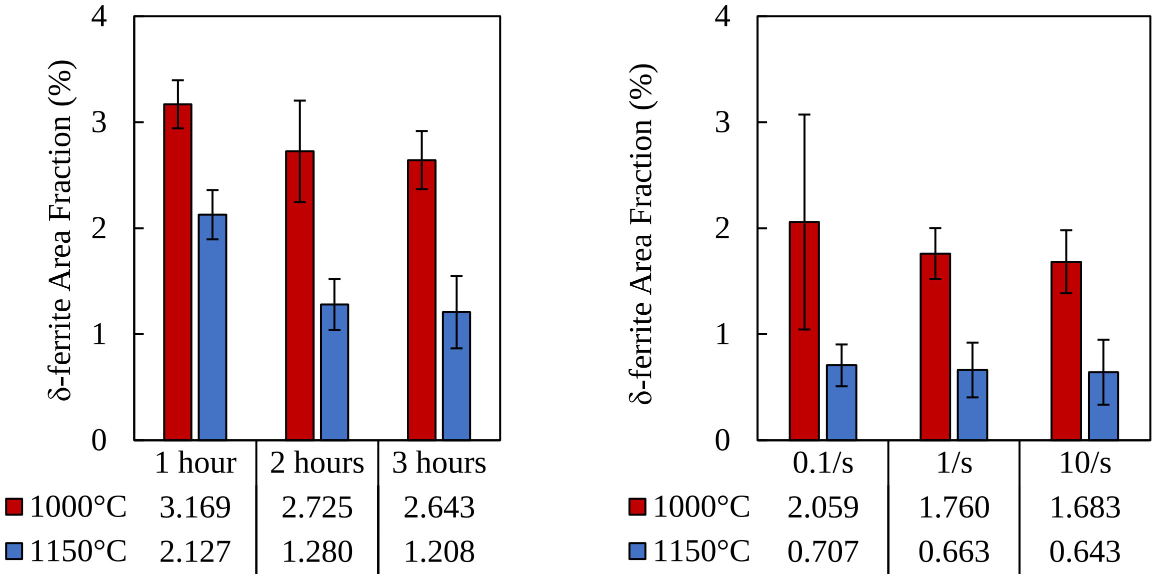

(a) (b)

Figure 40: JET area fraction measurements after (a) conventional annealing treatments, and (b) hot compression experiments.

5.1.3 304L Stainless Steel

The austenitic stainless steel 304L was electro-etched with a solution containing 10% oxalic acid diluted in DI water, while a dc current of 15V was applied. However, analogously from what was observed for the Jethete material, no δ-ferrite was found throughout the microstructure. Figure 41 shows the 304L alloy after received. This stainless steel presented a recrystallized microstructure, with small grains and twin boundaries, typically found on austenitic stainless steels. [5]

Figure 41: Optical microscopy showing the 304L as-received microstructure.

In order to create and induce the precipitation of δ-ferrite, the re-engineering of δ-ferrite process was adopted, re-melting the 304L samples at temperatures higher than 1400°C. The previous recrystallized microstructure gave place to a dendritic microstructure after the melting process, as shown on Figure 42. δ-ferrite, colored in dark, presented a dendritic, and vermicular stereology, characteristic of a cast microstructure. [43]

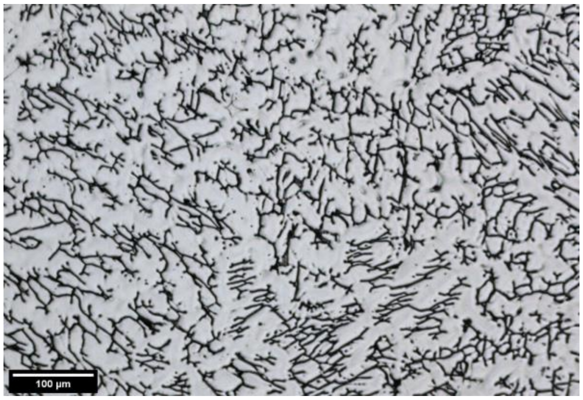

Figure 42: Optical microscopy showing the 304L microstructure after melting.

Figure 43 corroborates what was seen after optical microscopy with SEM/EDS characterization. As expected, the δ-ferrite exhibits a higher Chromium content in comparison with the austenitic matrix of the 304L alloy. Adopting a line-scan approach, the enrichment in Cr inside the δ-ferrite grains could be clearly seen.

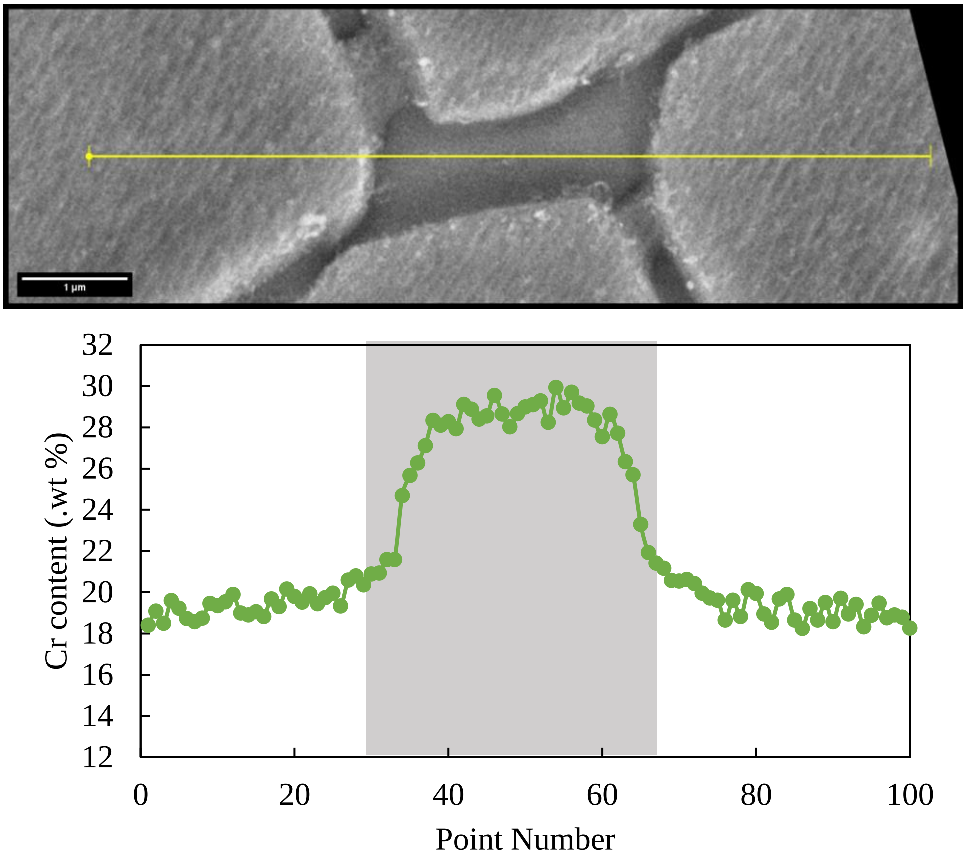

Figure 43 EDS analysis of the 304L as-melted sample

Since the δ-ferrite is now formed, the dissolution behavior of this phase could be investigated. As determined for all the samples analyzed, continuous annealing treatments and hot compression experiments acted as a baseline for further comparisons.

As visualized on the other alloys, morphological changes were expected to take place after each experimental step. Specifically, the 304L dendritic/vermiform morphology will give place to smaller and rounder δ-ferrite grains. As exemplified on Figure 44, after annealing, the microstructural evolution of δ-ferrite tends to the formation of round grains.

(a) (b) (c)

Figure 44: Schematics showing the 304L δ-ferrite phase morphology evolution - (a) to (c) - after annealing.

The influence of both time and temperature will be studied, concluding about each of those is more critical for increasing the dissolution kinetics of δ-ferrite. Later on, the deformation and strain rates will be also considered. Therefore, with the successful formation of this δ-ferrite, the samples were annealed at 1000°C, and three soaking times were selected. The vermicular δ-ferrite morphology apparently remains stable after 1 and 2 hours of treatment. On the other hand, after 3 hours, rounder grains were observed. The δ-ferrite area fraction seems to decrease as the holding time was increased. Figure 45 shows the micrographs of the samples treated at 1000°C for 1, 2, and 3 hours.


(a) (b) (c)

Figure 45: Optical microscopy of the 304L steel after annealing at 1000°C, for (a) 1h, (b) 2h, and (c) 3h.

Differently from what was observed before, the annealing time of 1150°C granted a higher energy to the system, which in turn acted as modifying the initial distribution of δ-ferrite at the initial stages of annealing. For this reason, round δ-ferrite grains were visualized after 1, 2, and 3 hours of treatment. Figure 46 exhibits the micrographs of the samples treated at this higher temperature of 1150°C for 1, 2, and 3 hours.

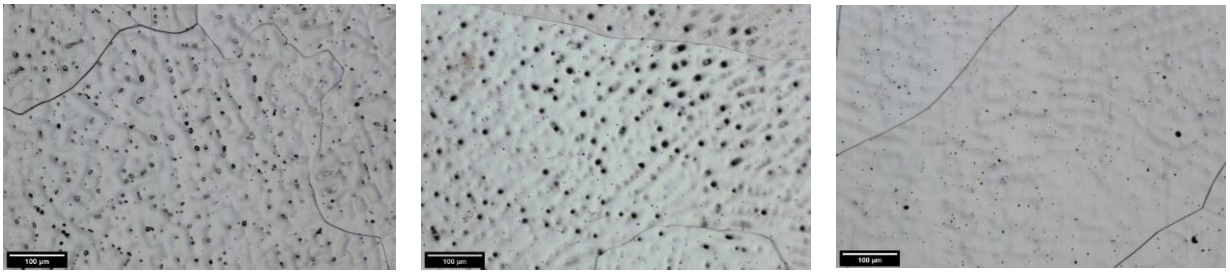
(a) (b) (c)

Figure 46: Optical microscopy of the 304L steel after annealing at 1150°C, for (a) 1h, (b) 2h, and (c) 3h

Higher energized systems would logically promote faster dissolution rates, and therefore, lower δ-ferrite area fractions, which accordingly calculated for the samples annealed at 1150°C. In addition, the impact of time and temperature could be evaluated, as the dissolved δ-ferrite percentage is higher after longer times and higher temperatures. After melting, the 304L steel showed values of, approximately, 25% of δ-ferrite, and when the most extreme condition was analyzed, i.e. after 3 hours at 1150°C, this number was considerably reduced to 0.76%. Each individual δ-ferrite grain was color thresholded, and the area fraction measurements are showed on Figure 47.

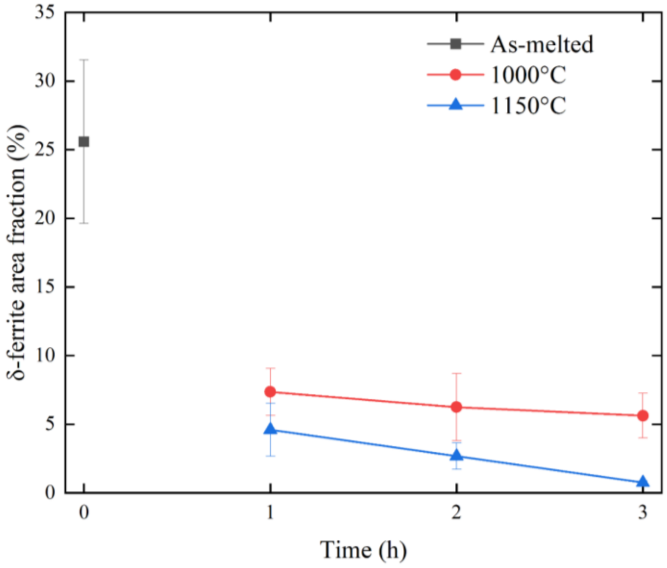

Figure 47: 304L area fraction measurements after conventional annealing treatments.

Schematics from Figure 44 can be compared with the ones showed on Figure 48, where samples treated for 2 hours, at both 1000°C and 1150°C, are represented. A sample treated at 1000°C presented a partial vermicular microstructure, whereas the specimen treated at the higher temperature of 1150°C showed a more round δ-ferrite distribution. The lower area fractions observed after 2 hours of treatment at 1150°C are justified in reason of the more energy spent towards the dissolution of δ-ferrite. Additionally, shorter diffusion paths could be evidenced by the difference in δ-ferrite morphologies and area fractions on the highlighted stages.

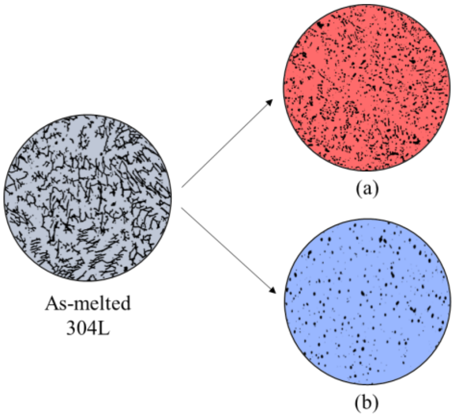

Figure 48: Comparisons of the 304L samples treated at (a) 1000°C and (b) 1150°C, both for 2 hours.

As suggested and proposed for the other two alloys, the 304L material was subsequently subjected to hot compression. For this reason, time and temperature were combined with strain rate and deformation, creating a system more susceptible to inducing δ-ferrite diffusion. From what can be visualized on Figure 49, the first set of compression was performed at 1000°C, under different strain rates. However, no substantial decrease in δ-ferrite area fraction was perceptible, nor any categorical changes in morphology. For all designs, the δ-ferrite vermicular distribution remained roughly constant, not becoming more circular as observed after annealing.

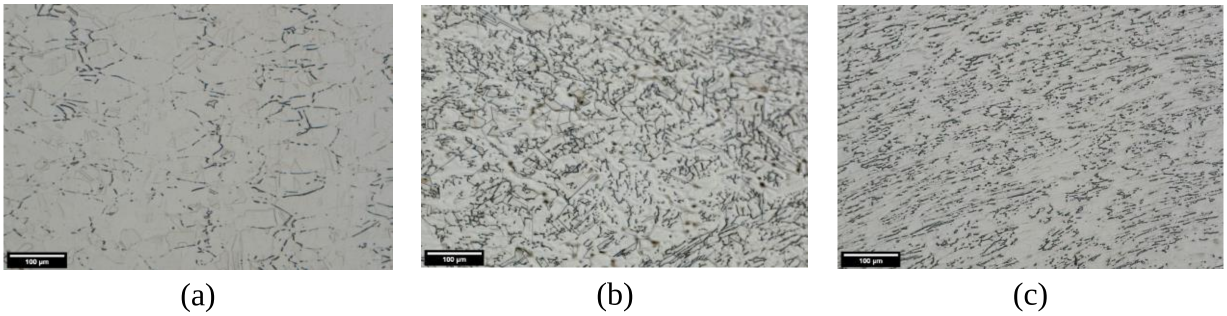

Figure 49: Optical microscopy of the 304L steel after hot compression and post processing at 1000°C, at (a) 0.1/s, (b) 1/s, and (c) 10/s strain rates.

Since the temperature of 1000°C was not enough to promote visible deviations in terms of δ-ferrite percentage, a higher post processing temperature of 1150°C was further studied. One similar behavior was recognized, as the area fraction remains constant even after increasing the strain rate. On the other hand, the reduction in δ-ferrite area fraction was more accentuated, explained by the higher temperature adopted after deformation. The micrographs regarding these treatment conditions can be seen on Figure 50.

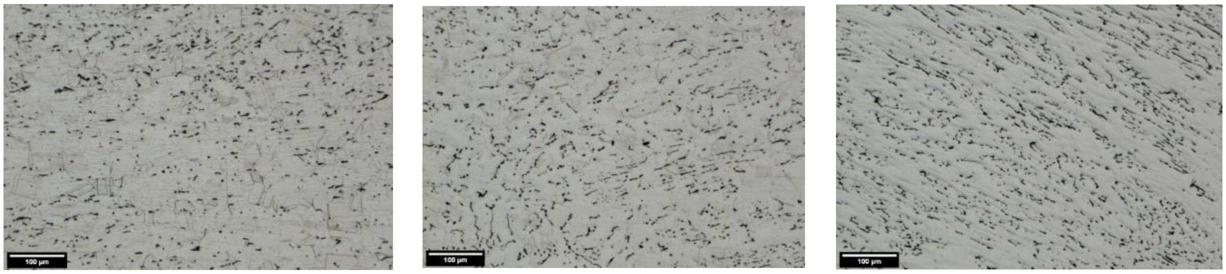

(a) (b) (c)

Figure 50: Optical microscopy of the 304L steel after hot compression and post processing at 1150°C, at (a) 0.1/s, (b) 1/s, and (c) 10/s strain rates.

For one post processing temperature, 1150°C, the hot compression experiments increased the dissolution kinetics of the system, since the δ-ferrite area fraction remarkably decreased after 10 minutes of post processing heat treatments. In contrast, no changes were observed with the variation in strain rate, as this parameter by itself does not seem to produce an increase on the reaction of dissolution compared to time and temperature. Samples treated at the lower post processing temperature of 1000°C did not exhibit large deviations when compared to the alloys conventionally annealed at the same temperature. Although, the decrease in area fraction was considered significant, similar δ-ferrite percentages were observed after annealing for 1, 2, and 3 hours, and after 10 minutes of post compression treatments. Figure 51 shows the area fraction measurements after hot compression experiments.

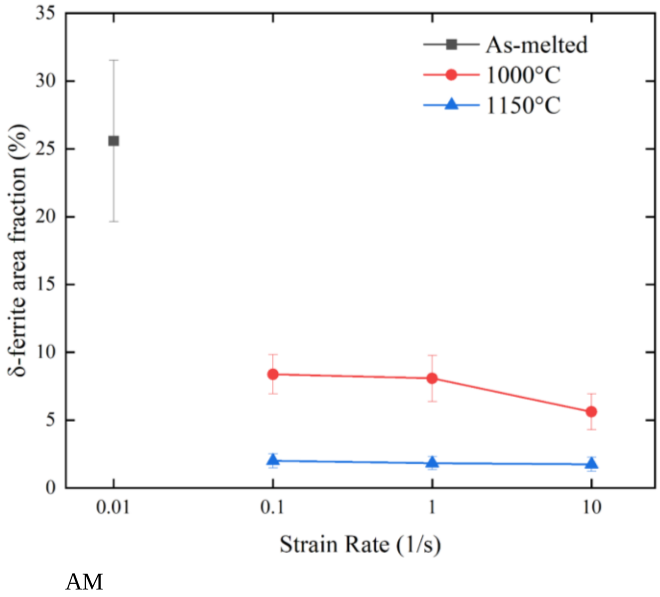

Figure 51: 304L area fraction measurements after hot compression experiments.

For the 304L steel, the expected behavior after compression was observed. When fixing the strain rate and individually comparing the post processing temperatures, lower δ-ferrite fractions were seen at 1150°C. Additionally, the vermicular distribution, characteristic of the as-melted sample, apparently disappears with the combination of compression and annealing at 1150°C. Figure 52 compares the samples analyzed after 10/s compression strain rate and the two adopted annealing temperatures.

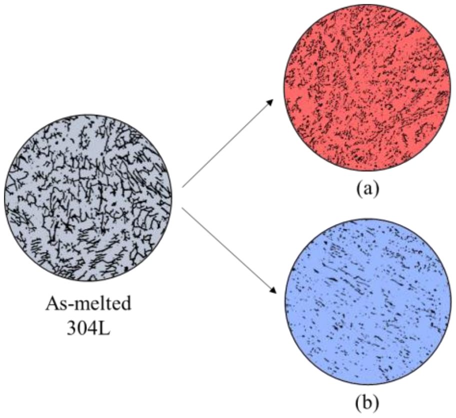

Figure 52: Comparisons of the 304L samples post heat treated at (a) 1000°C and (b) 1150°C, after compressed under 10/s strain rate.

A comparison of the δ-ferrite area fractions can be seen on Figure 53, where both analyses, after conventional and hot compression treatments, were evaluated. As expected, at the two selected temperatures, higher annealing times promoted a more emphasized decrease in δ-ferrite fractions, with the temperature of 1150°C being more effective, as the area fractions were considerably lower. In contrast, after compression, the two different adopted post deformation temperatures produced samples with different fractions of δ-ferrite. At 1000°C, those values were higher due to the higher flow stress at a low temperature, compared with the samples post treated at 1150°C, that presented a short diffusion path due to the lower flow stresses.

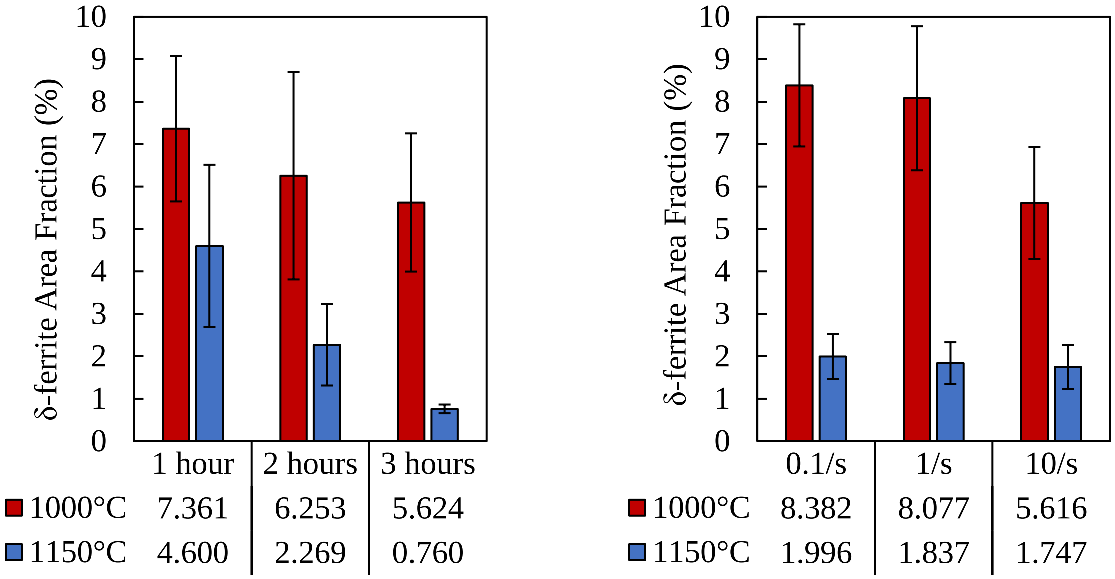

(a) (b)

Figure 53: 304L area fraction measurements after (a) conventional annealing treatments, and (b) hot compression experiments.

After compression, the dissolution behavior of the alloy post treated at 1000°C seems to be less effective compared to the values observed after isothermal annealing and holding times for the same comparable temperatures. However, increasing the holding time after deformation and annealing appeared to be more effective on dissolving the δ-ferrite at 1000°C. On the other hand, at 1150°C, only the annealing of 3 hours generated a sample containing lower δ-ferrite fractions than what was observed after compression (at strain rates of 0.1 and 1/s). For this case, the input of a higher temperature, in combination with deformation, could create a system where the dissolution of δ-ferrite was increased, the percentages of the δ-ferrite were measured to be close to 1.8%.

5.2 Advanced Microstructural Characterization

Proceeding with more advanced characterization, chemical composition measurements were acquired with the aid of EPMA analysis. This technique was utilized to identify chemical deviations between the matrix and the δ-ferrite phases, within each individual sample. Along with this approach, the examination of chemical differences across samples from distinct experimental simulations were besides investigated.

5.2.1 15-5 PH Stainless Steel

15-5 PH samples, from the two different physical simulations, were studied regarding chemical composition analysis. Two samples for each experimental design were selected: after annealing at 1000°C for 1 hour, and after treating at 1150°C for 3 hours. In addition, two samples were analyzed after hot compression: 1) 1000°C at a strain rate of 0.1/s; and 2) 1150°C compressed at 10/s. Besides the overall chemical composition evaluation, the EPMA analysis was mainly focused on measuring the chemical deviation δ-ferrite vs. matrix, firstly in terms of Cr and Ni content. As known, those two elements usually exhibit characteristic trends when the δ-ferrite phase is targeted. For the 15-5 PH alloy, this behavior could be highlighted and will be further discussed. Compositional line profiles were acquired for the as-received material, and the results are included on Figure 54. Shaded areas represent regions inside the δ-ferrite grains.

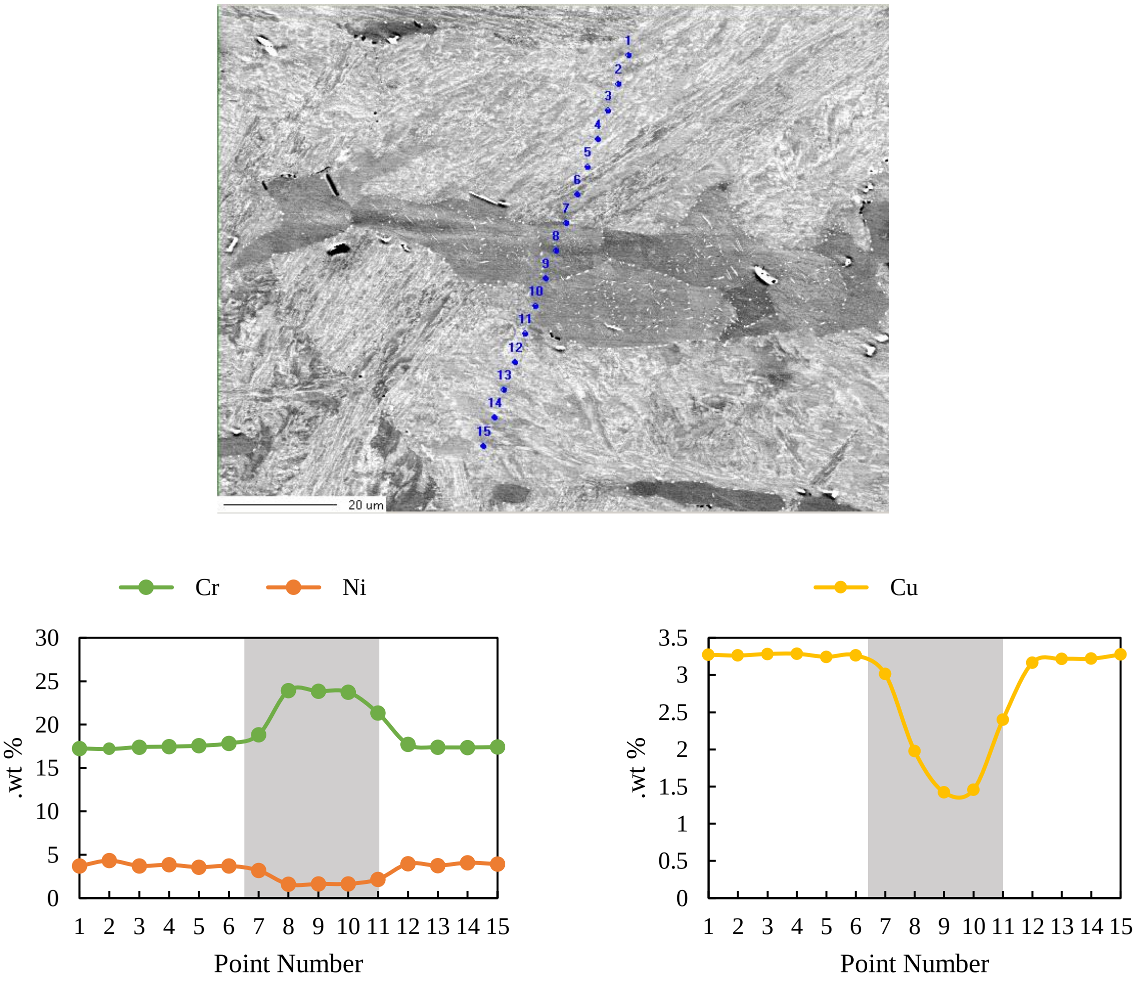

Figure 54: EPMA measurements for the as-received 15-5 PH steel, with respective Cr, Ni and Cu content.

Along with the compositional line profiles, map analysis was performed on the as-received sample, where the chemical composition differences could be more accentuated seen. As well with the differences in Chromium, Nickel, and Copper, precipitates were seen along the δ-ferrite boundaries. Figure 55 shows the results, where Nb and Cu carbides were seen across those regions.

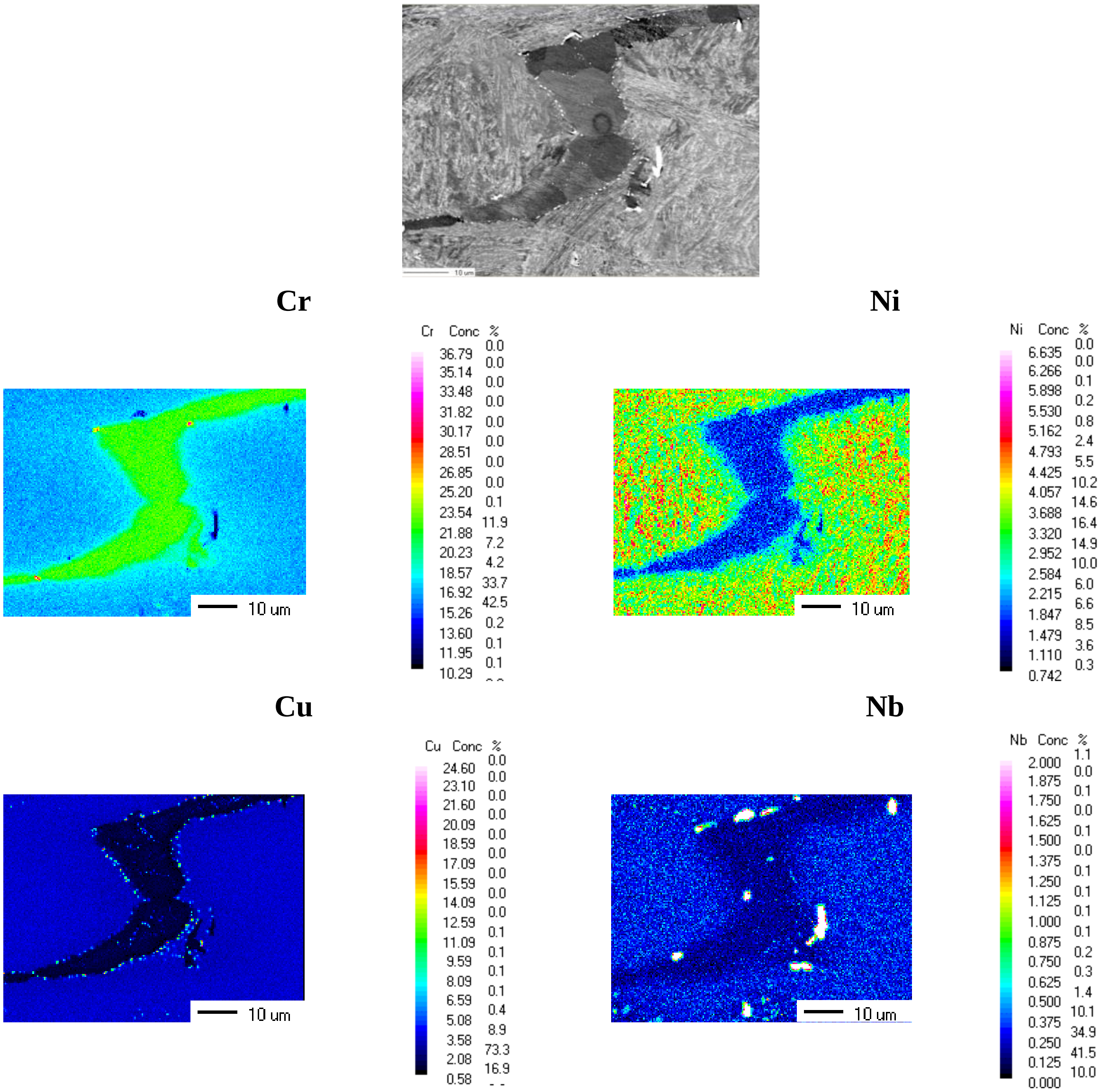

Figure 55: EPMA map analysis for the as-received 15-5 PH steel.

The EPMA results indicate the different behavior attached to the δ-ferrite regions of the 15-5 PH steel. As elucidated, once the measurements were acquired over the δ-ferrite areas, a Cr enrichment followed by a defacement in Ni and Cu was clearly visible. Similar analysis was carried out on the samples subjected to the most extreme conditions along the experimental approach. Therefore, for the annealing treatments, the combination of the lowest temperature, 1000°C, with the shortest time, 1 hour, was selected, as well the highest temperature, 1150°C, attached to the longest annealing time of 3 hours. The chemical dissolution behavior of δ-ferrite was again studied based on those two opposite conditions, where chemical deviations are expected to be seen. Figure 56 shows these EPMA data.

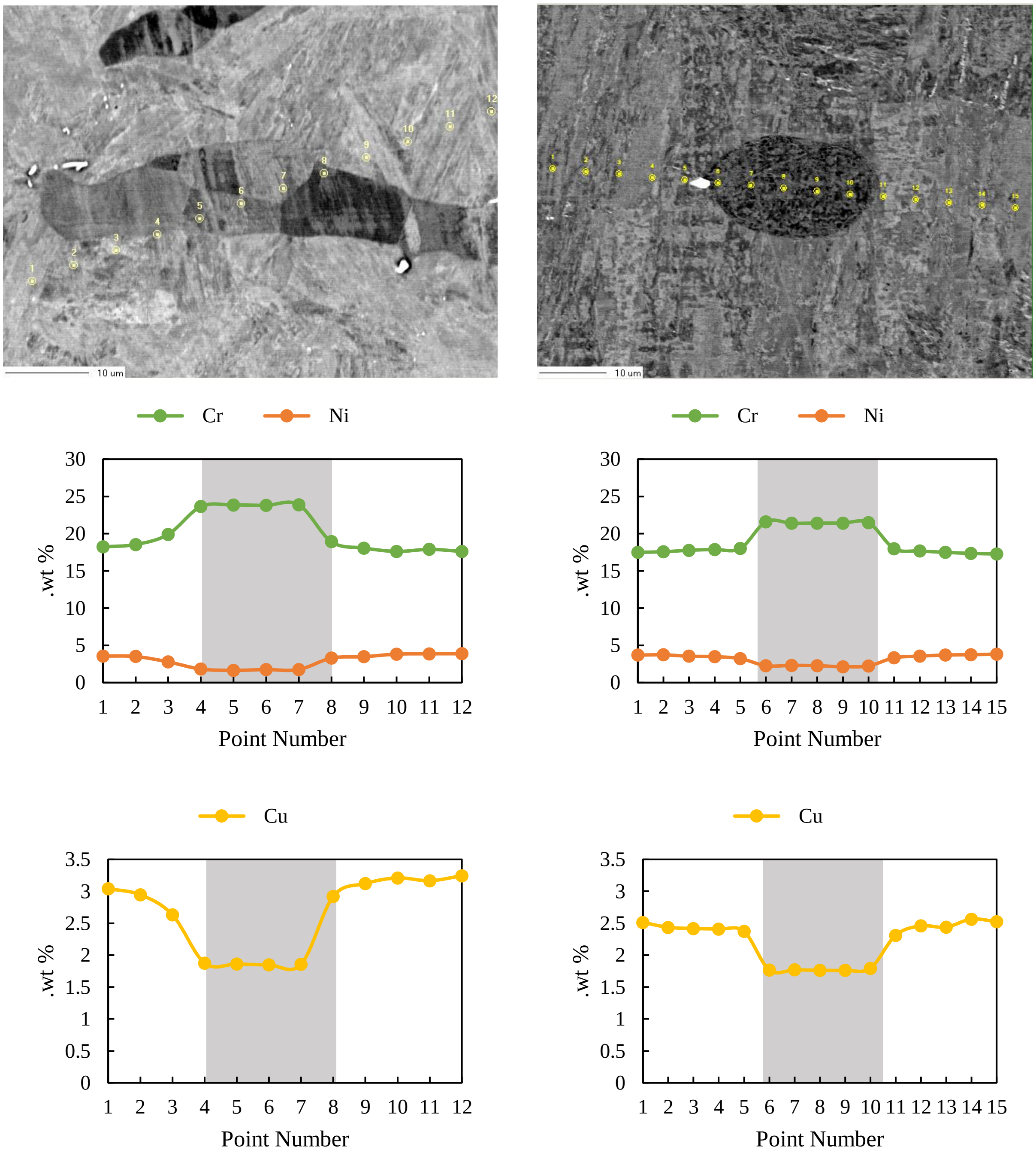

(a) (b)

Figure 56: EPMA measurements for the annealed 15-5PH samples at (a) 1000°C for 1 hour, and (b) 1150°C for 3 hours, with respective Cr, Ni and Cu content.

Both selected conditions presented Cr and Ni differences, as could be seen on the as-received specimen. However, since the annealing temperature promotes a microstructural homogenization with the increasing in holding time, the deviation matrix ↔ δ-ferrite was apparently less significant after heat treating the alloy at 1150°C for 3 hours. At this most extreme condition, a 3.81wt% drop in Cr content was observed, whereas after annealing at 1000°C for 1 hour this Cr difference reached 5.51wt%.

When analyzing the Cr content behavior inside and outside the δ-ferrite islands, a better understanding about the diffusion phenomena could be achieved. Figure 57 shows the average Cr values for the samples annealed at 1150°C. At this temperature, both the matrix and the δ-ferrite phase exhibited a lower Cr content as the time goes longer, indicating the diffusion of this element towards the complete microstructural homogenization. If longer annealing times were utilized, the deviation between the δ-ferrite and the matrix were expected to be even lower.

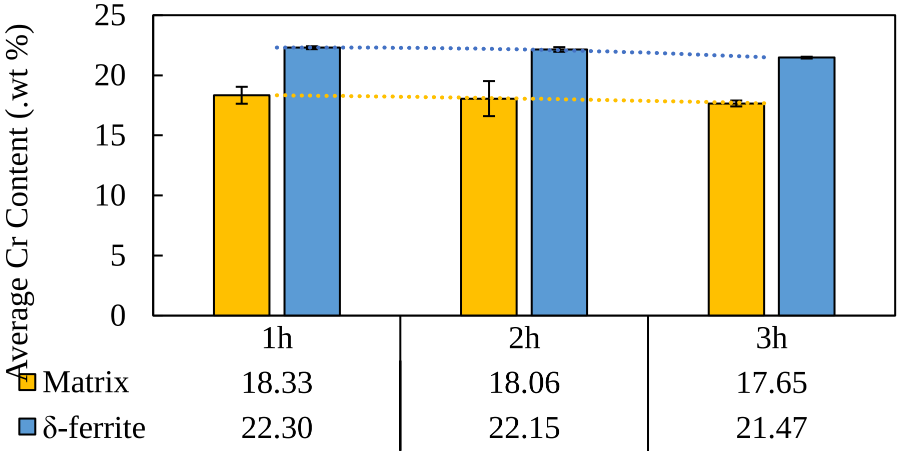

Figure 57: Cr average values from EPMA for each annealed condition at 1150°C.

After hot compression, the same approach was used, selecting the two extreme conditions. The sample compressed under 0.1/s strain rate and post processed at 1000°C, and the material deformed under 10/s strain rate and post processed at 1150°C. Line compositional profiles, with respective chemical elements content are exemplified on Figure 58, targeting Cr, Ni, and Cu readings, as demonstrated before.

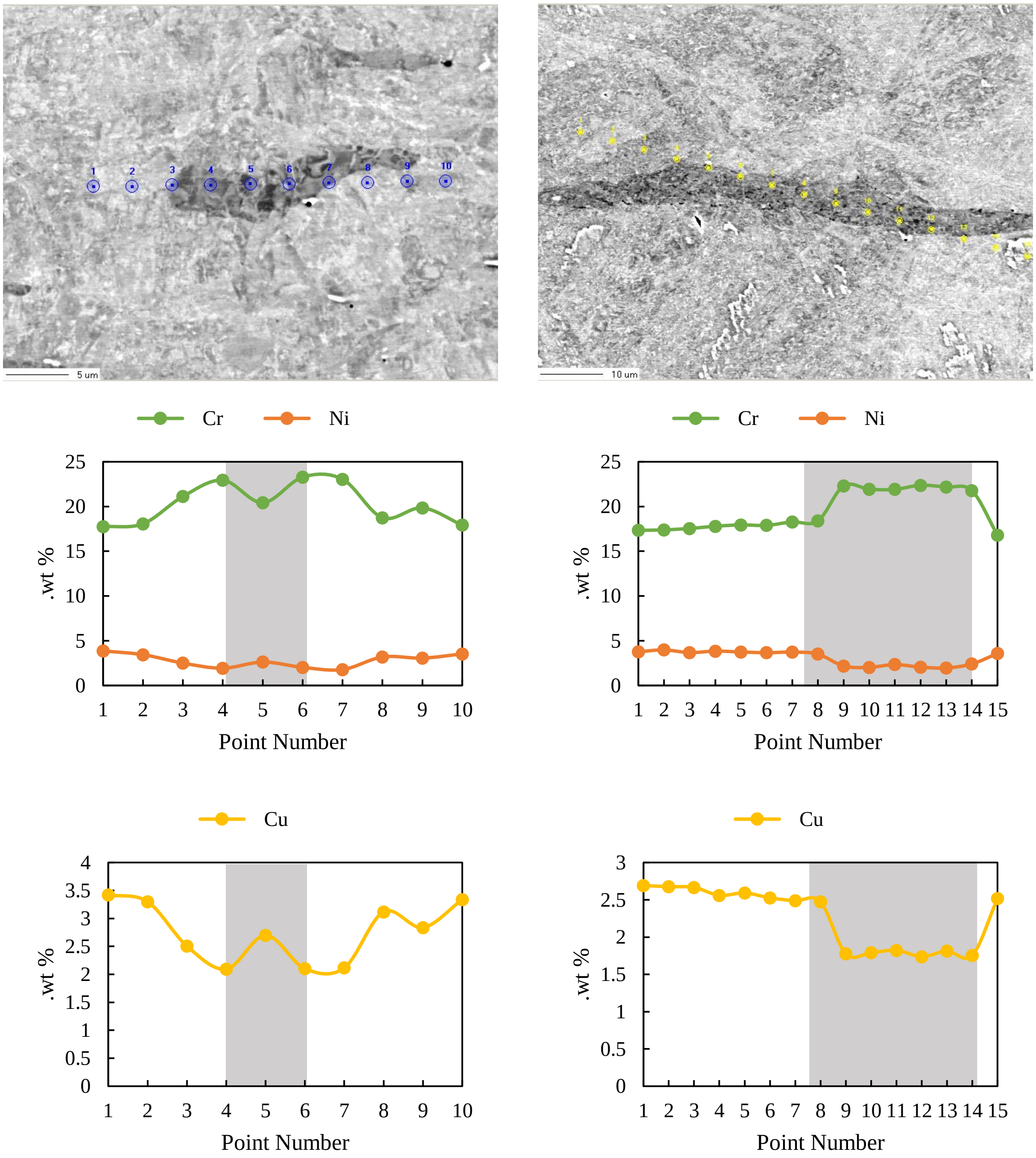

(a) (b)

Figure 58: EPMA measurements for the hot compressed 15-5PH samples at (a) 1000°C under 0.1/s strain rate, and (b) 1150°C under 10/s strain rate, with respective Cr, Ni and Cu content.

Chemical deviations after compression demonstrated not as strong as the ones observed after annealing, as the EPMA results showed similar values at both of the regions of interest. For the sample compressed at 0.1/s strain rate and post processed at 1000°C for 10 minutes, average values at the matrix and at the δ-ferrite exhibited a 4.21wt% of Cr deviation. On the other hand, the sample more strongly compressed, and post treated at a higher temperature presented a 4.50wt% Cr difference. In addition, when all the hot deformation parameters are analyzed, no significant changes are noticed after post heat treatments at 1150°C, as the matrix and the δ-ferrite Cr composition remain constant with the increase in strain rate. Figure 66 presents those measurements.

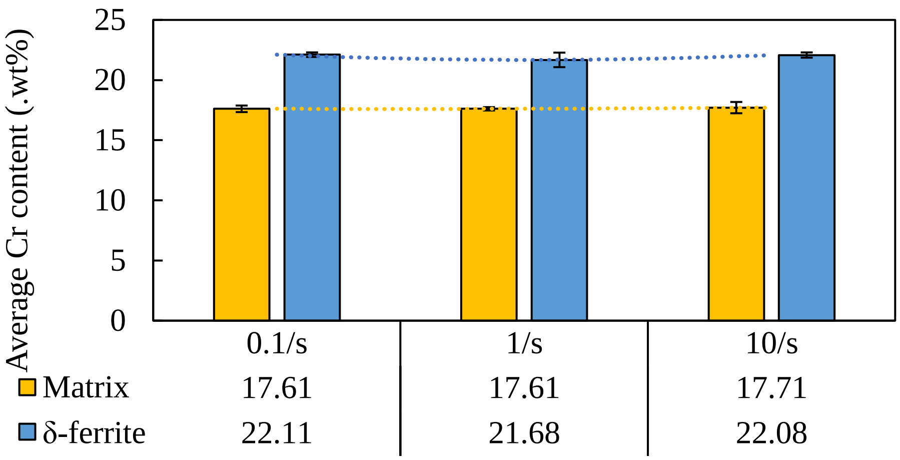

Figure 59: Cr average values from EPMA for each compressed condition at 1150°C.

5.2.2 154-Jethete Stainless Steel

Following the same approach that was conducted for the 15-5PH alloy, the Jethete material was subjected to chemical composition analyses with the aid of EPMA. This alloy was studied after the re-engineering treatment, and after each physical simulation, highlighting the most extreme ones. Figure 60 shows the EPMA analysis for the as-melted material.

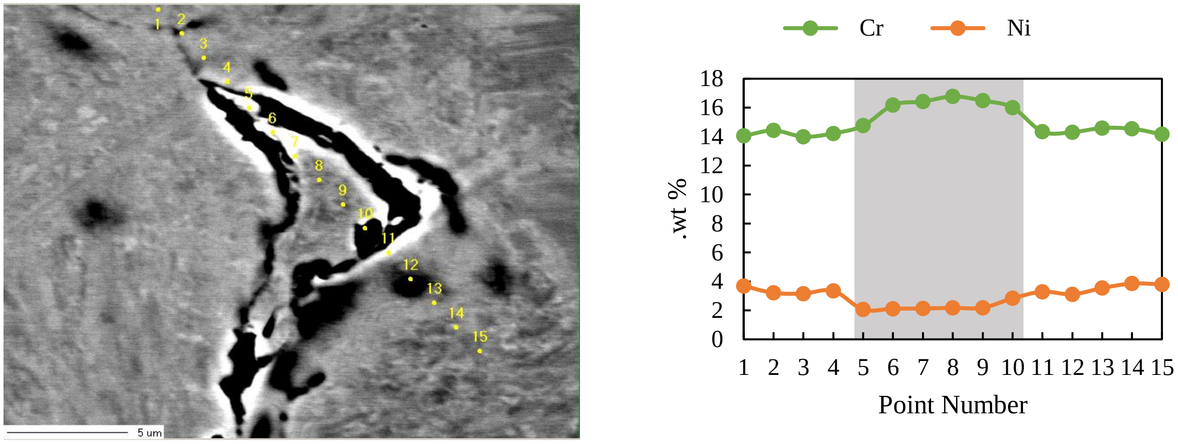

Figure 60: EPMA measurements for the melted M-154 Jethete steel, with respective Cr and Ni content.

As expected, higher Cr content could be seen followed by lower Ni readings inside the δ-ferrite grain. The same behavior could be visualized when a map analysis was performed. The results can be seen on Figure 61.

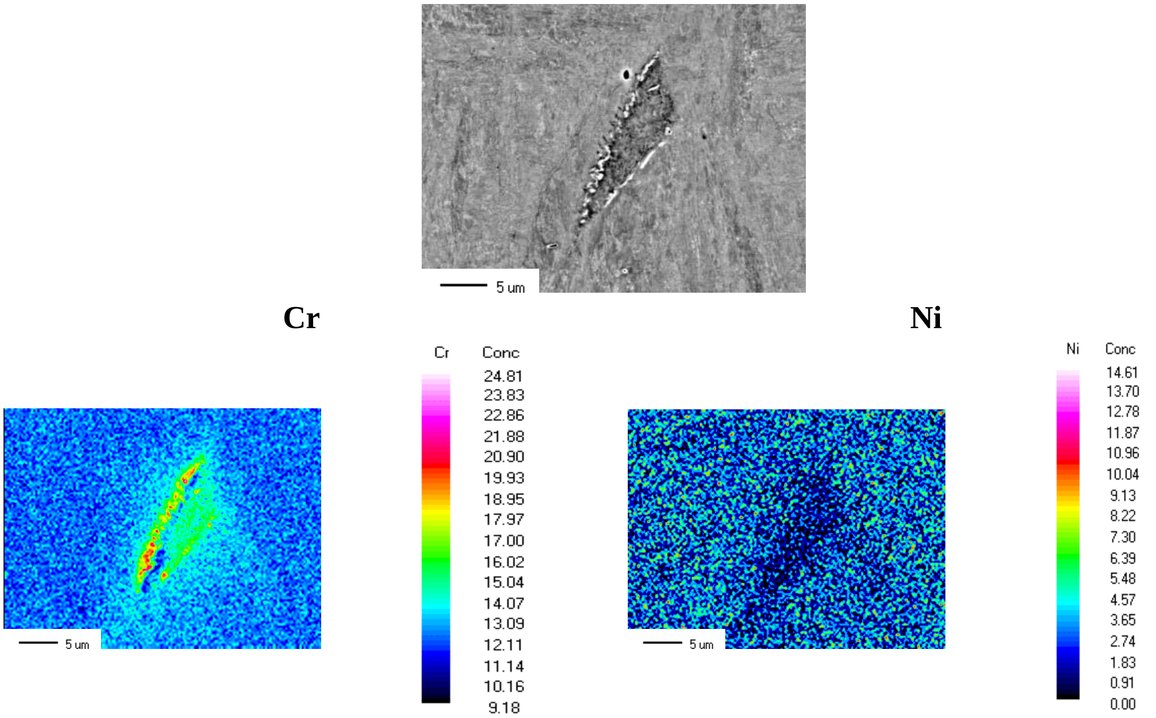

Figure 61: EPMA map analysis for the as-melted M-154 Jethete steel.

As the conventional annealing heat treatments were conducted, no significant chemical changes were noticed, even after analyzing the samples subjected to lower temperatures and times. According to Figure 62, both samples treated at 1000°C for 1 hour and at 1150°C for 3 hours presented a lighter increase in chromium inside the δ-ferrite islands. The results indicate a faster homogenization of the microstructure even after shorter annealing heat treatments.

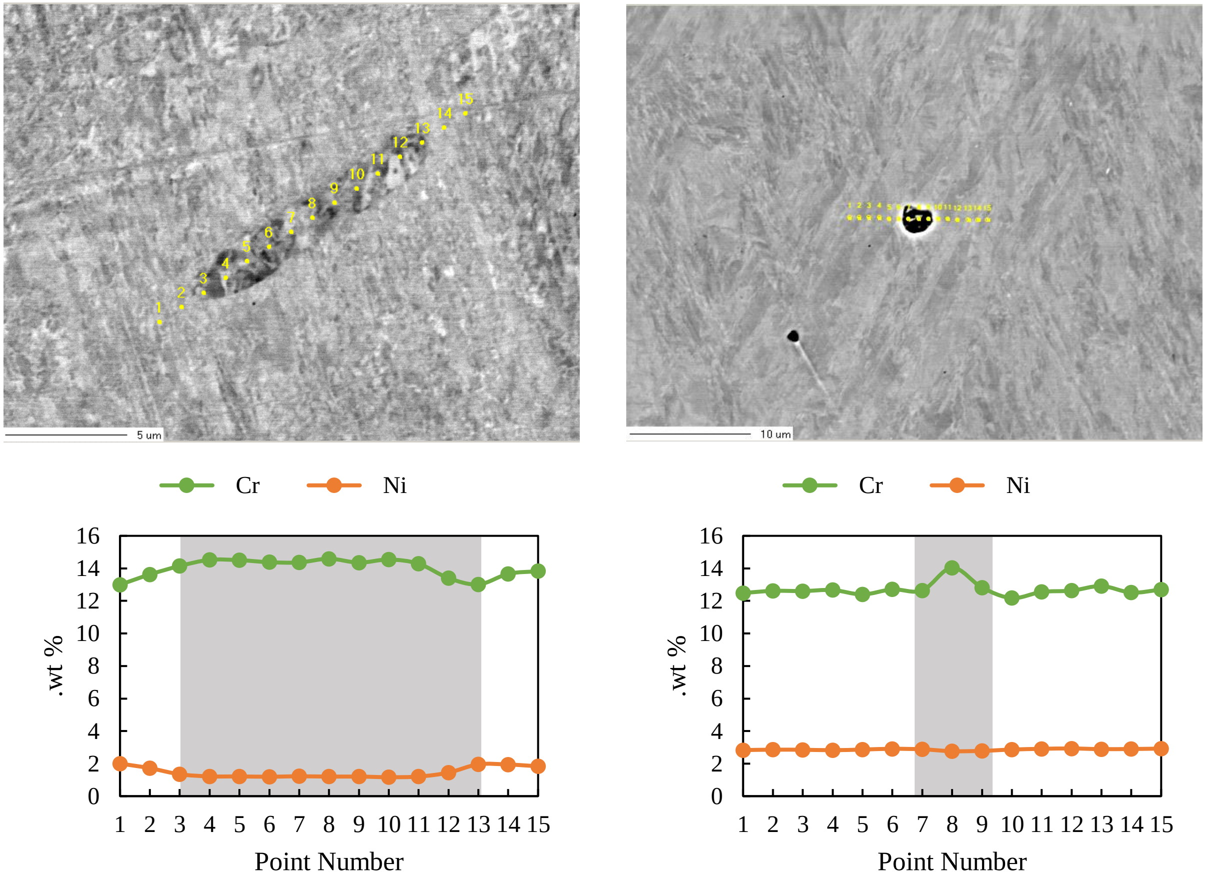

(a) (b)

Figure 62: EPMA measurements for the M-154 Jethete annealed samples at (a) 1000°C for 1 hour, and (b) 1150°C for 3 hours, with respective Cr and Ni content.

Analyzing Figures Figure 60 and Figure 62, it is possible to notice a more accentuated deviation between the matrix and the δ-ferrite grains on the re-melted specimen, which exhibited a 2.03wt% of Cr content difference. However, the conventional annealed Jethete material only showed a variance of 0.9wt% of Cr after 1 hour at 1000°C, and of 0.5wt% of Cr posteriorly to the heat treatment at 1150°C for 3 hours. The average Cr content inside and outside the δ-ferrite grains was assessed on all annealed samples at 1150°C. As the time was increased, lower Cr contents were measured on both areas, following by a smaller difference matrix vs. δ-ferrite, indicating that the decrease in area fraction acted in accordance with a chemical accommodation of the material. Figure 63 represents those measurements.

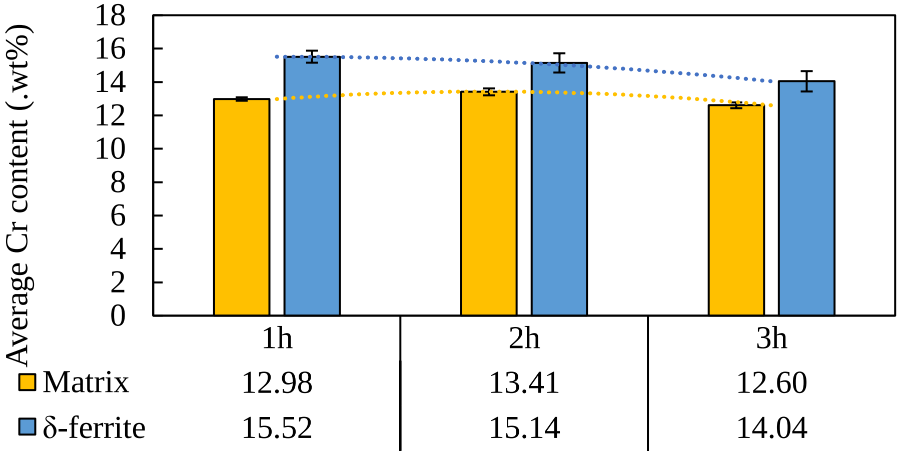

Figure 63: Cr average values from EPMA for each annealed condition at 1150°C.

After hot compression, samples were evaluated with regard of chemical composition. The two opposite states were analyzed, i.e., after compression under 0.1/s strain rate and post heating at 1000°C, and when a faster strain rate of 10/s was used prior to a post annealing process at 1150°C for 10 minutes. Figure 64 shows this analysis, highlighting the Cr and Ni content.

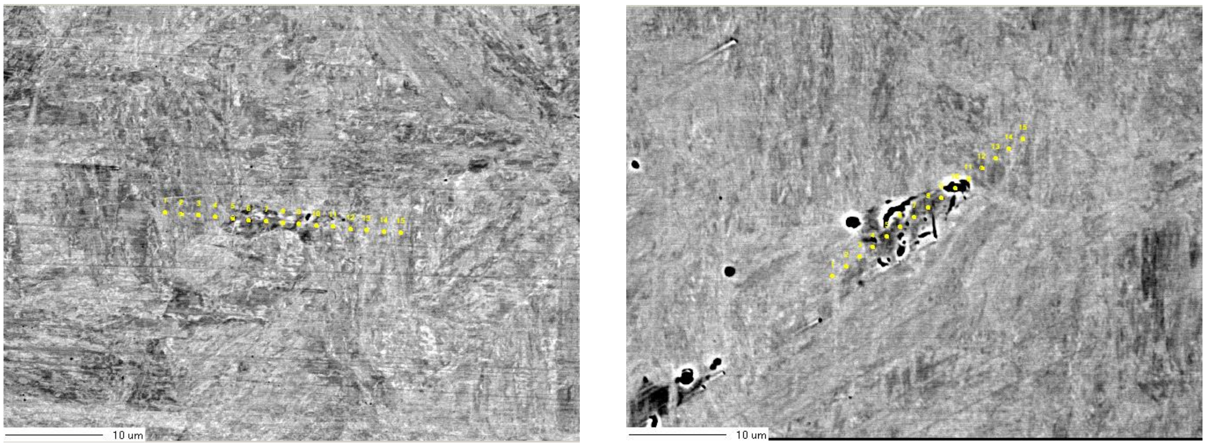

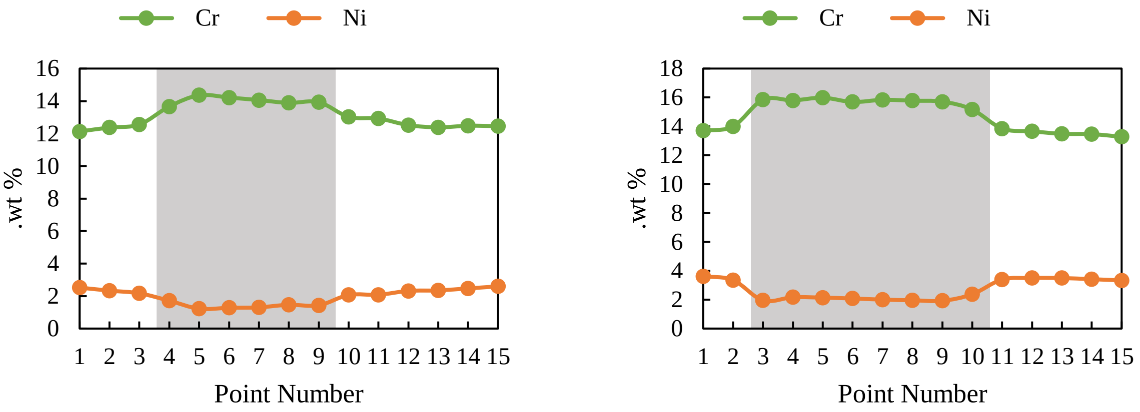

(a) (b)

Figure 64: EPMA measurements for the hot compressed M-154 Jethete samples at (a) 1000°C under 0.1/s strain rate, and (b) 1150°C under 10/s strain rate, with respective Cr and Ni content.

Following the opposite behavior from the annealed material, a more emphasized difference could be noticed along the δ-ferrite phase after compression. Higher Cr and lower Ni readings were seen, reaching an average of 1.9wt% of Cr difference when all conditions were considered. The post compression annealing time of 10 minutes was not sufficient to promote an intense microstructural homogenization, as was visualized when longer soaking times were adopted during annealing. To illustrate this idea, Figure 65 shows the measurements for the compressed samples post processed at 1150°C. As the strain rate is increased, not significant changes are presented, but a considerable difference between the matrix and the δ-ferrite grains were clearly seen.

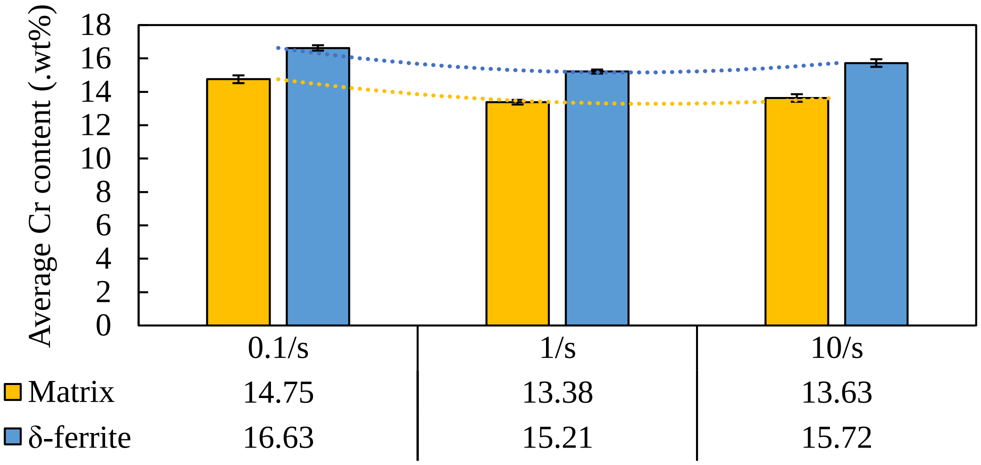

Figure 65: Cr average values from EPMA for each compressed condition at 1150°C.

5.2.3 304L Stainless Steel

The 304L steel was analyzed in terms of chemical composition following the same approach utilized previously: the extreme conditions were selected. In addition, EPMA examination was as well conducted on the as-melted sample. Figure 66 shows the analyses for the 304L steel after the re-engineering treatment to create δ-ferrite. A higher Cr content is well known to be seen along the δ-ferrite grains, followed by a chemical depletion of Ni. Those results corroborate what was observed after EDS measurements.

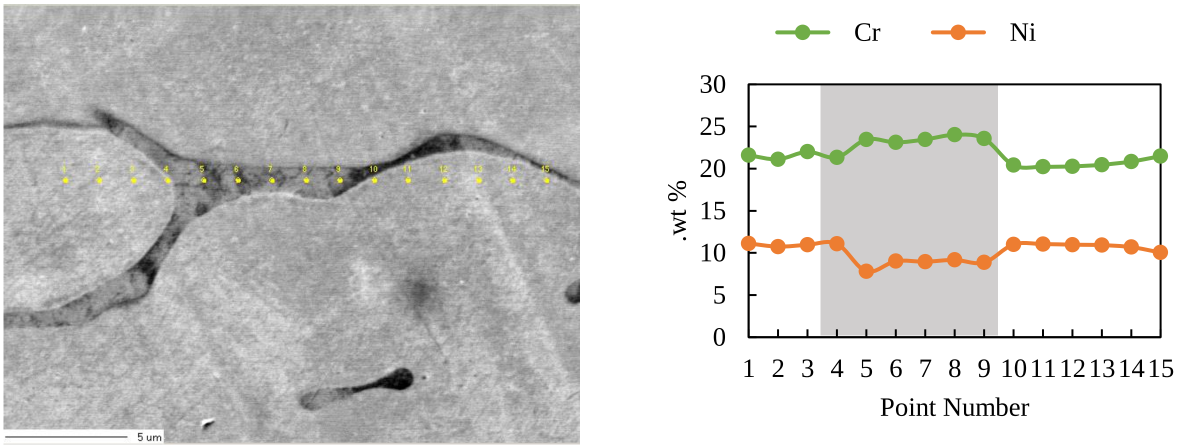

Figure 66: EPMA measurements for the melted 304L steel, with respective Cr and Ni content

To better illustrate the differences in composition between the δ-ferrite and the matrix, map analysis was conducted in addition with the compositional line measurements. The results presented on Figure 67 plainly shows differences in terms of Cr and Ni. However, since the 304L alloy was re-melted to form δ-ferrite, the differences are not as clear as the ones observed for the 15-5PH steel. For example, the δ-ferrite grains that exhibit a more accentuated depletion in Ni were colored in blue, where the ones with not as highlighted decrease were colored in green. The opposite can be stated in terms of the Cr content.

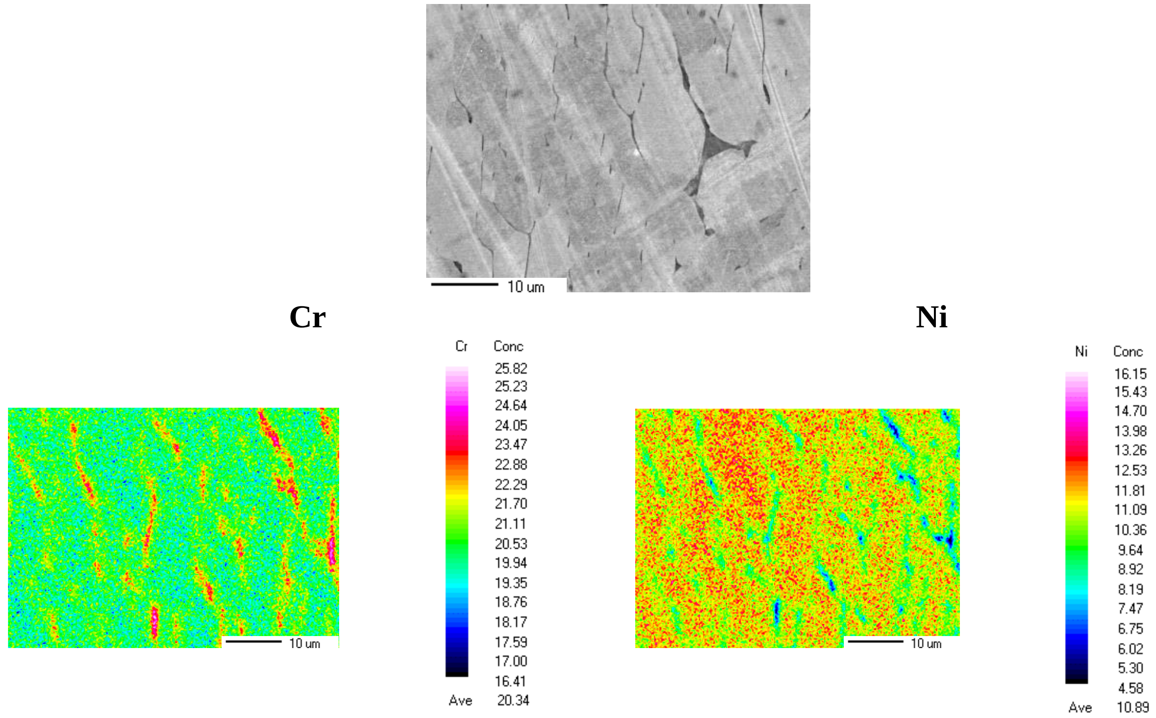

Figure 67: EPMA map analysis for melted 304L steel.

Once the melted condition was studied, the EPMA analysis focused on demonstrating if any chemical deviation could be seen on samples originated from different experiments. In other words, the Cr and Ni deviation were investigated and Figure 68 exhibits the results acquired after annealing, at 1000°C for 1 hour and at 1150°C for 3 hours.

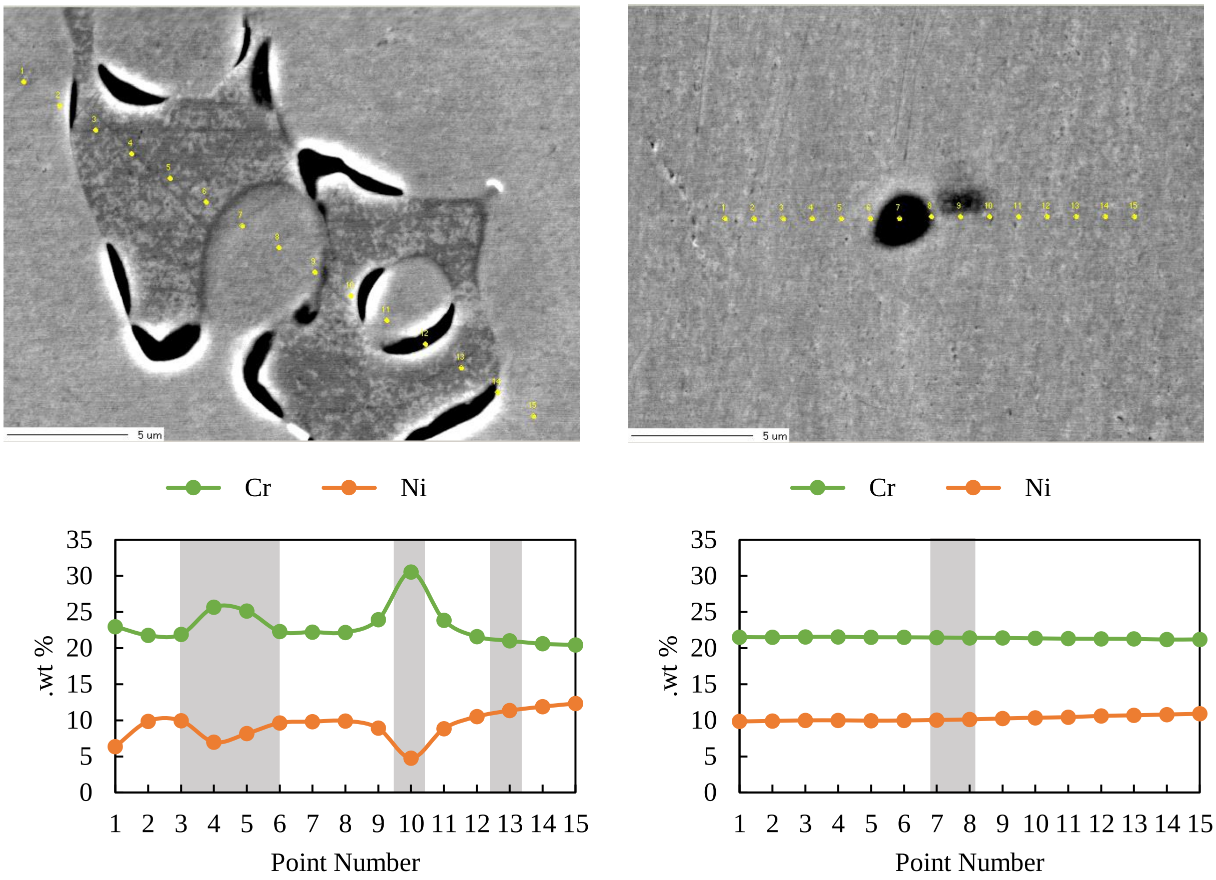

(a) (b)

Figure 68: EPMA measurements for the 304L annealed samples at (a) 1000°C for 1 hour, and (b) 1150°C for 3 hours, with respective Cr and Ni content.

The results indicate a plain difference between the two selected states. The highest annealing temperature, in combination with the longest heat treatment time moreover promoted a faster δ-ferrite dissolution rate, but also induced a homogenization of the microstructure, by minimizing the matrix/δ-ferrite composition differences. As predicted, once the δ-ferrite is dissolved, a chemical accommodation would take place, and no chemistry differences would be seen. This phenomenon took place after treating the 304L alloy at 1150°C for 3 hours, but a clear trend could be seen when the other samples were analyzed after annealing at this temperature. Figure 69 exemplifies the change in Cr content on the matrix and inside the δ-ferrite areas with the increase in annealing time, at a fixed temperature. As longer treatment times were adopted, more energized was the system, promoting the δ-ferrite dissolution, and therefore homogenizing the microstructure.

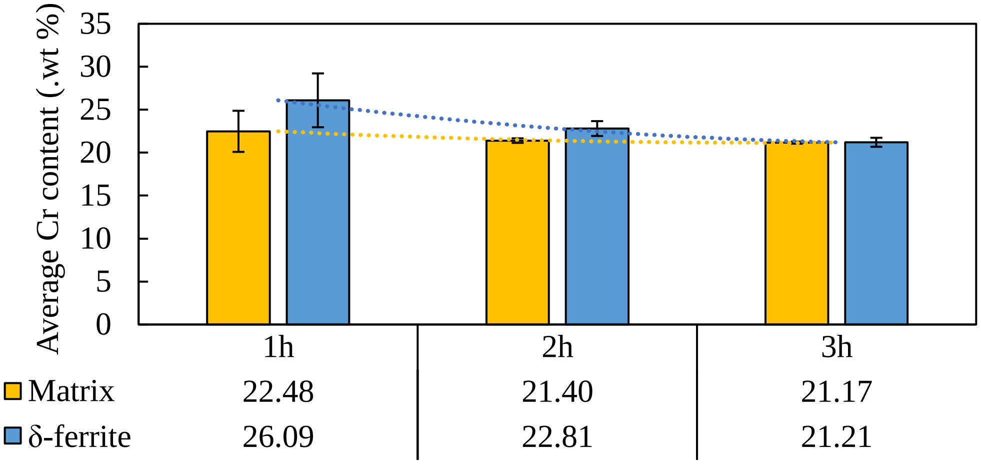

Figure 69: Cr average values from EPMA for each annealed condition at 1150°C.

Following with the same approach, the chemical differences caused by the addition of compression to the system were examined. The two most opposite conditions were analyzed, and the results can be visualized on Figure 70. The material compressed under a 0.1/s strain rate and post processed at 1000°C for 10 minutes was compared with the alloy deformed under a rate of 10/s and post heat treated at 1150°C.

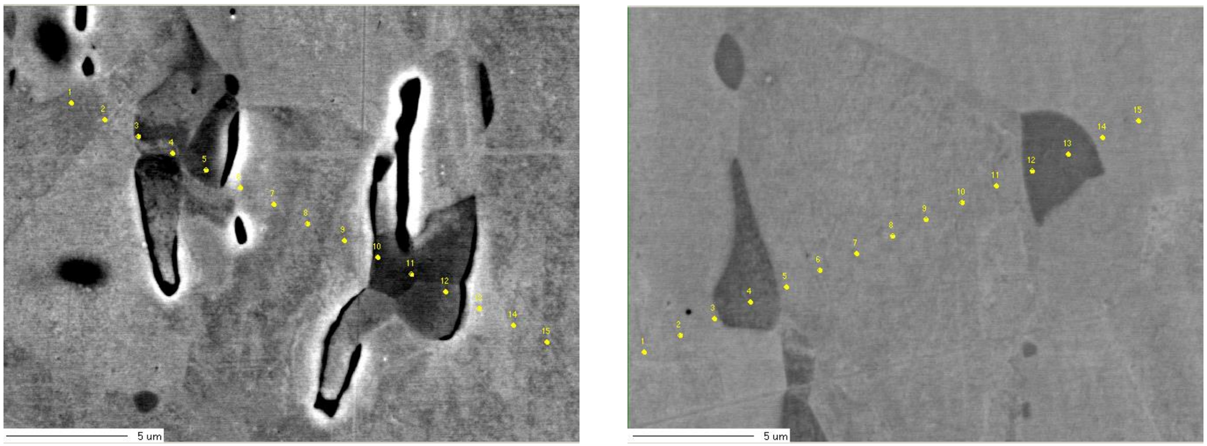

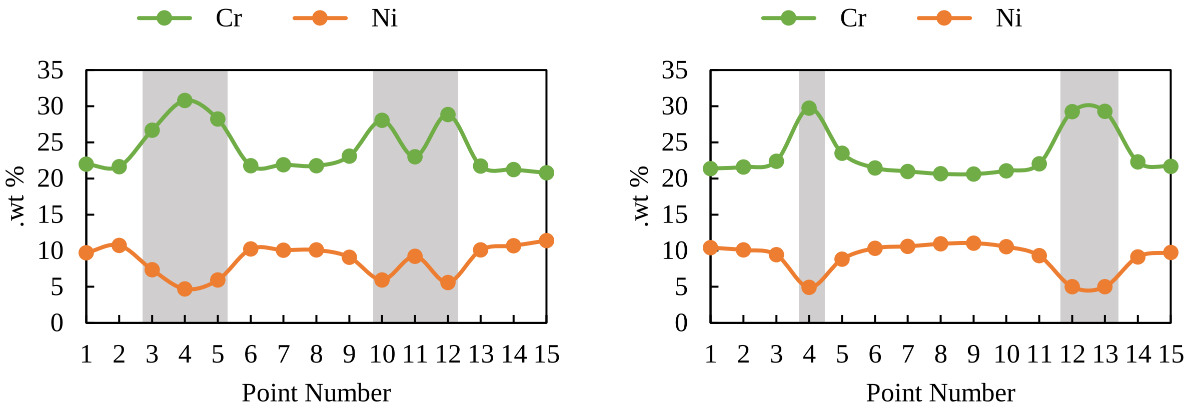

(a) (b)

Figure 70: EPMA measurements for the hot compressed 304L samples at (a) 1000°C under 0.1/s strain rate, and (b) 1150°C under 10/s strain rate, with respective Cr and Ni content.

Differently from what was observed before, the increase in strain rate does not have a direct influence on the 304L microstructural homogenization. The post process temperature seems to be more effective on promoting this phenomenon; however, since all samples were heat treated using the same soaking time, any considerable changes could be noticed. The average compositional values are seen on Figure 71, with no significant changes either on the matrix, and neither on the δ-ferrite phases. The chemical composition remained close to constant and within the standard deviation.

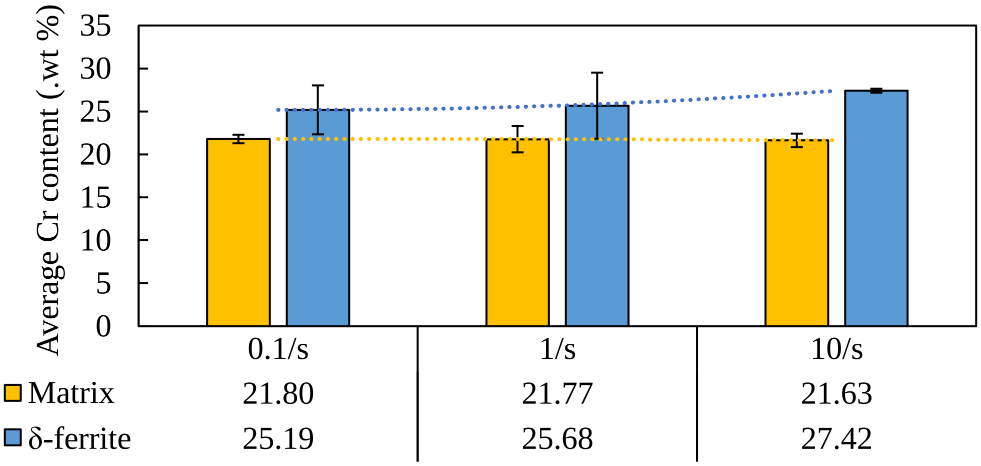

Figure 71: Cr average values from EPMA for each compressed condition at 1150°C.

5.3 Thermodynamic Simulations

Thermodynamic simulations were conducted with the aid of Thermo-Calc software, equipped with Diffusion Module DICTRA. [37] As an input, EDS compositional lines were obtained for each alloy. Figure 72 shows the line-scans along with the Cr and Ni weight percentages measured after EDS analysis. 500 grid points were acquired guaranteeing enough readings both on the matrix and on the δ-ferrite regions.

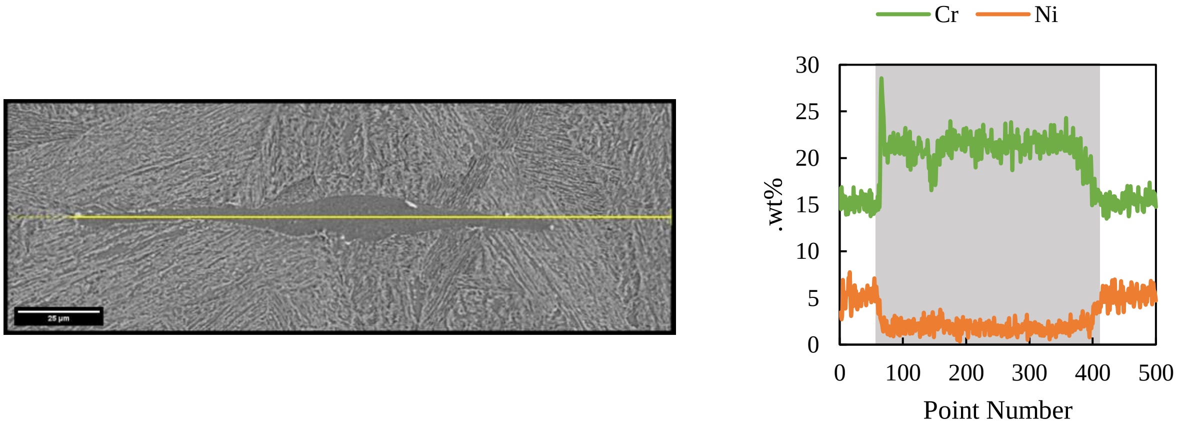

(a)

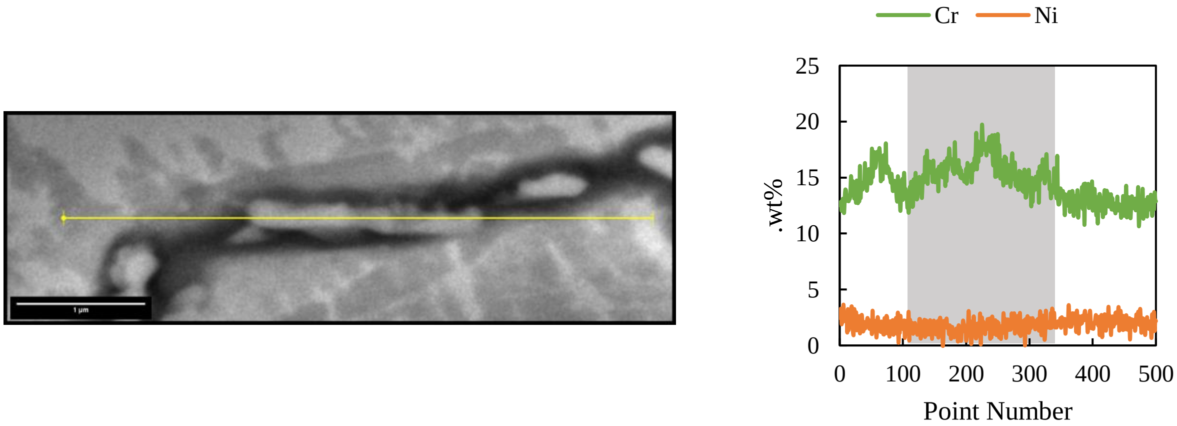

(b)

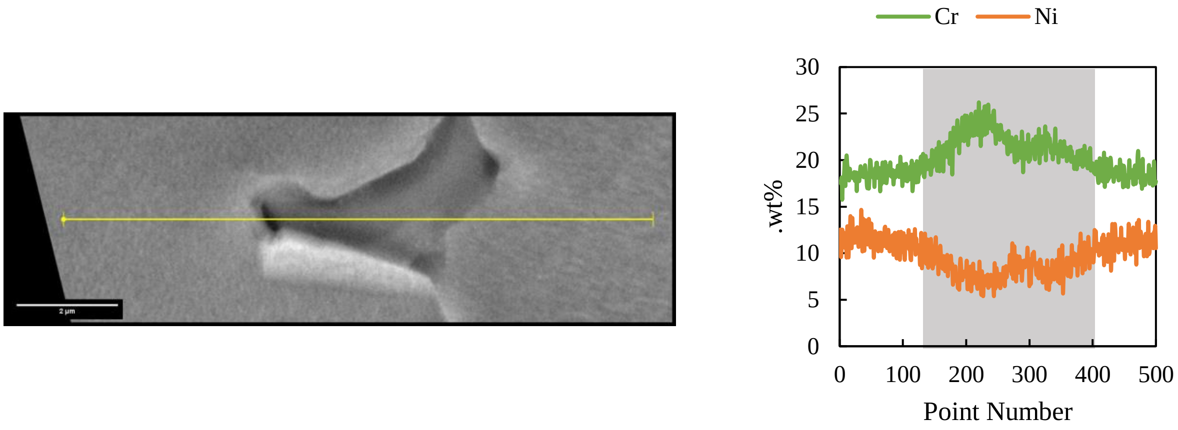

(c)

Figure 72: EDS compositional lines input for: (a) 15-5PH, (b) JET, and (c) 304L materials.

The simulations were done assuming the δ-ferrite dissolution as a homogenization process; in other words, as the dissolution progresses, a chemical accommodation takes place simultaneously within the matrix of each stainless steel. For this reason, all the systems were analyzed considering each of their matrices: a BCC matrix for the 15-5PH and the M-154 Jethete alloys, and an FCC matrix, for the 304L steel. Six different annealing times were selected for the simulation: 30 minutes, 1 hour, 2 hours, 3 hours, 4 hours, 5 hours, and 10 hours, and the two experimental temperatures, 1000°C and 1150°C, were fixed. Figure 73 demonstrates the results for the 15-5PH alloy.

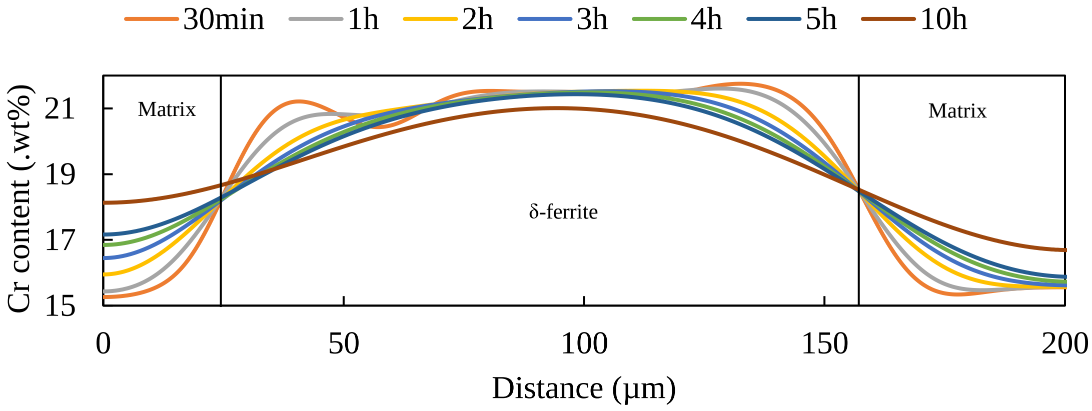

(a)

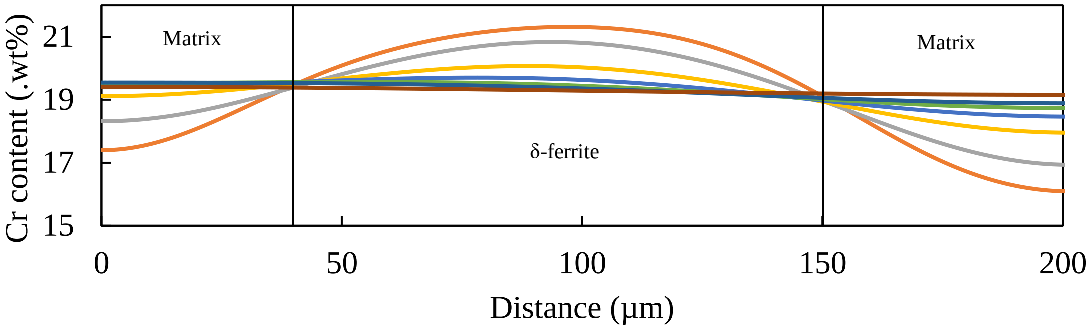

(b)

Figure 73: 15-5PH DICTRA simulations at (a) 1000°C, and (b) 1150°C, showing the Cr content evolution after different annealing times.

Comparing the simulations done using 1000°C and 1150°C, two main observations can be made. Firstly, as the simulation time is increased, the Cr content is decreased inside the δ-ferrite regions for both temperatures, presupposing the occurrence of dissolution. However, when a higher temperature is accounted, the decrease in Cr is more abrupt, appearing to be homogeneous after 3 hours of annealing, corroborating for the faster dissolution and reduction in area fraction noticed for the 15-5PH alloy after annealing at 1150°C. Secondly, the distance correspondent to the δ-ferrite island is shortened as both simulation times or temperatures are enlarged, also demonstrating dissolution.

Since the Cr and Ni content substantially changed within the δ-ferrite grains, the maximum compositional heterogeneity was expected to be found within those areas, which indeed was measured after EPMA analysis. Therefore, at a certain distance, a Cr enrichment and Ni depletion were noticed, representing the δ-ferrite grains. Hence, the time to fully homogenize each of the studied materials was estimated by fixing this distance. Figure 74 shows the Cr and Ni variation as a function of time, for the 15-5PH material. According to the DICTRA calculations, the expected homogenization time is reached when the Cr levels are decreased towards a plateau, while Ni content is increased, and then stabilized.

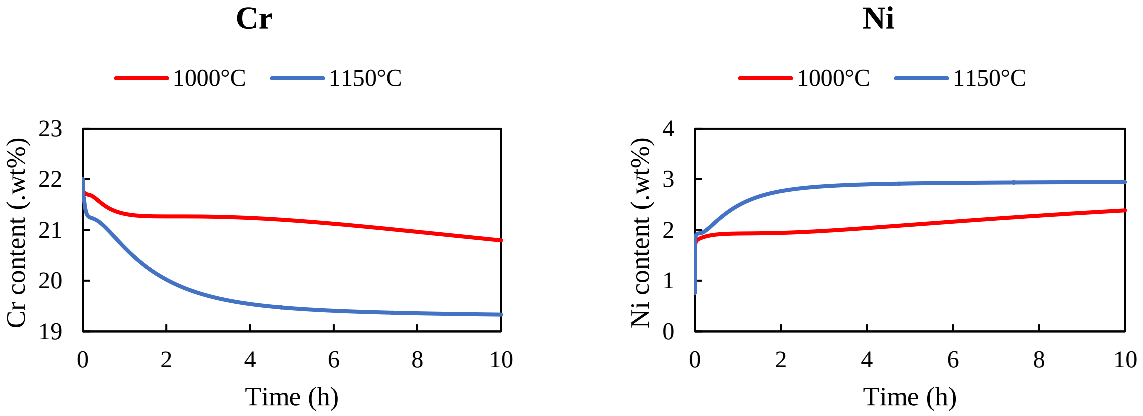

Figure 74: Variation of Cr and Ni at the δ-ferrite location as a function of the predicted time by DICTRA, for the 15-5PH steel.

When the simulation was performed considering a temperature of 1000°C, both Cr and Ni did not present a uniform behavior as the time was increased, indicating that the chemical accommodation of those elements would happen at times longer than 10 hours. Differently, for the simulation at 1150°C, a plateau could be observed after 6 hours, associating a microstructural homogenization and an almost complete dissolution of δ-ferrite. The results observed on Figure 74 can be validated by the EPMA measurements done after the annealing treatments at 1150°C, exhibited on Figure 57, where an approximation between the Cr content in the matrix and in the δ-ferrite grains was noticed as longer annealing were adopted.

Figure 75 shows the simulations performed on the M-154 Jethete material under the same circumstances and parameters. As the simulation time was increased, a chemical homogenization was induced, as the Cr content appeared to get constant throughout the matrix and the δ-ferrite regions. In addition, this chemical accommodation process is more favorable at higher temperatures, where the decrease in Cr content inside the δ-ferrite grains was found to be more accentuated as the time was overestimated. For the annealing simulation at 1150°C for 10 hours, a minimum deviation could be perceptible, probably indicating a complete δ-ferrite dissolution at that time. The simulation done at 1150°C follows the same trend as was observed after EPMA analysis, on Figure 63.

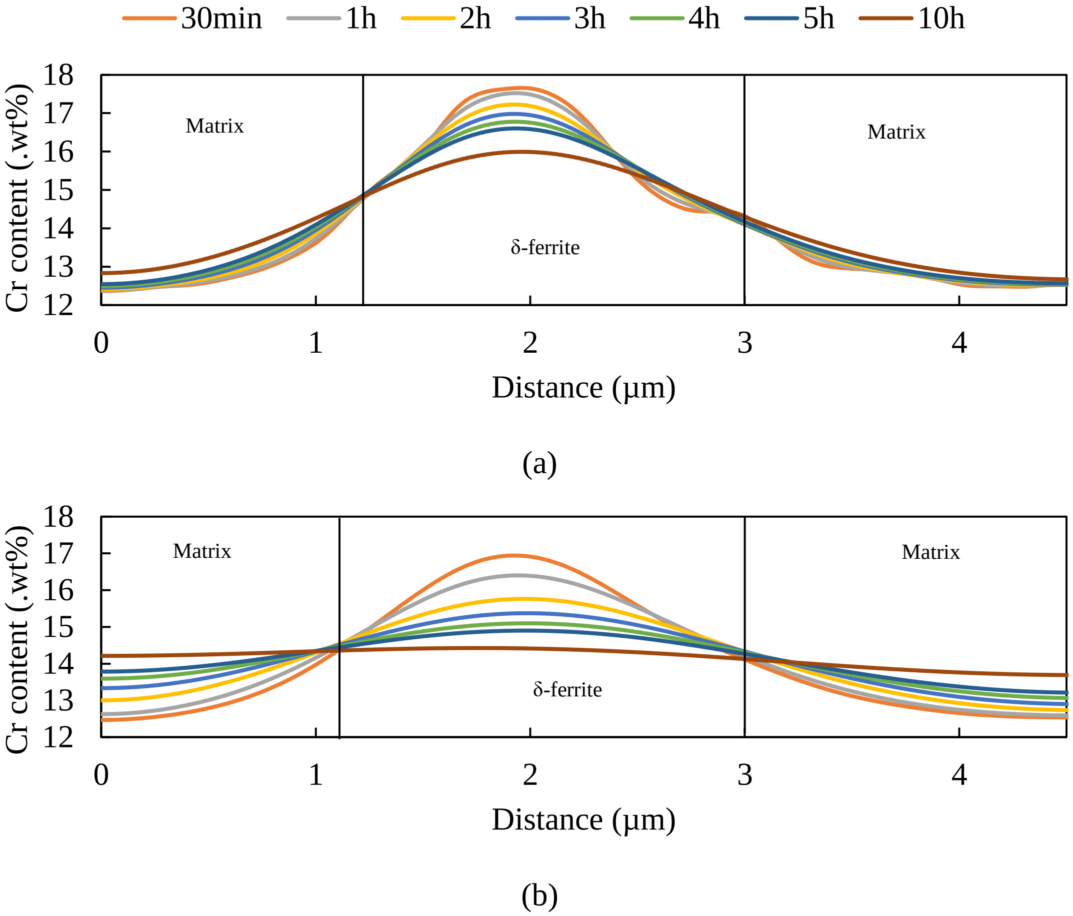

(a)

(b)

Figure 75: JET DICTRA simulations at (a) 1000°C, and (b) 1150°C, showing the Cr content evolution after different annealing times.

The full dissolution time was simulated by fixing a certain distance, that represented the δ-ferrite grains. Those areas exhibited higher Cr and lower Ni contents with respect to the material matrix. For the Jethete material and according to DICTRA, the simulation conducted at 1000°C demonstrates that the Cr and Ni accommodation was not fully completed even after 10 hours of annealing. In contrast, when the higher temperature of 1150°C was adopted, a constant tendency could be seen after 8 hours of annealing, as the higher energy promoted by the system temperature offered a shorter diffusion path, favoring the δ-ferrite dissolution. Figure 76 presents those calculations.

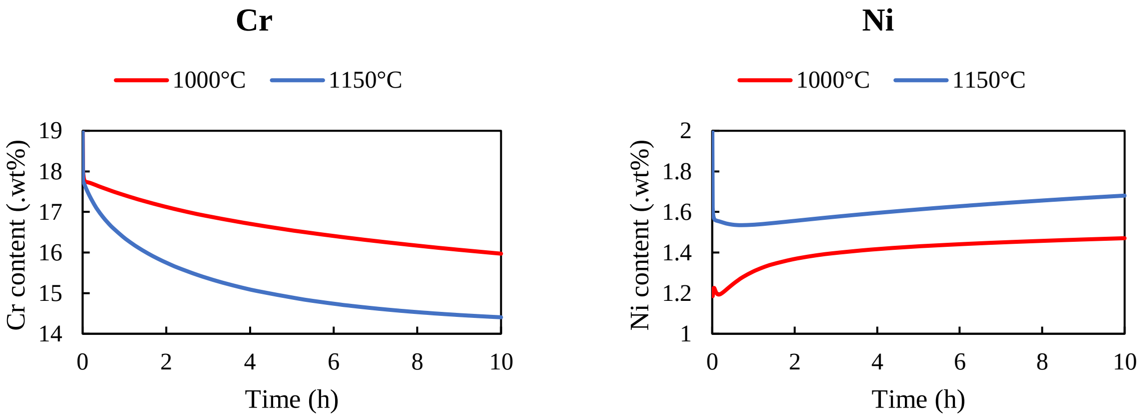

Figure 76: Variation of Cr and Ni at the δ-ferrite location as a function of the predicted time by DICTRA, for the JET steel.

The same parameters and approach were used for conducting the simulation of the 304L material, and the data output can be seen on Figure 77. The difference between the simulation ran at 1000°C and at 1150°C is clear, as the Cr content goes lower inside the δ-ferrite grains when longer annealing times were simulated. In addition, the simulation conducted at 1150°C predicted a drastically reduction in Cr inside the δ-ferrite islands, even after short annealing times, such as 30 minutes. This behavior points out to a stronger influence of temperature on the δ-ferrite dissolution on the 304L alloy, in agreement with the EPMA results presented on Figure 69.

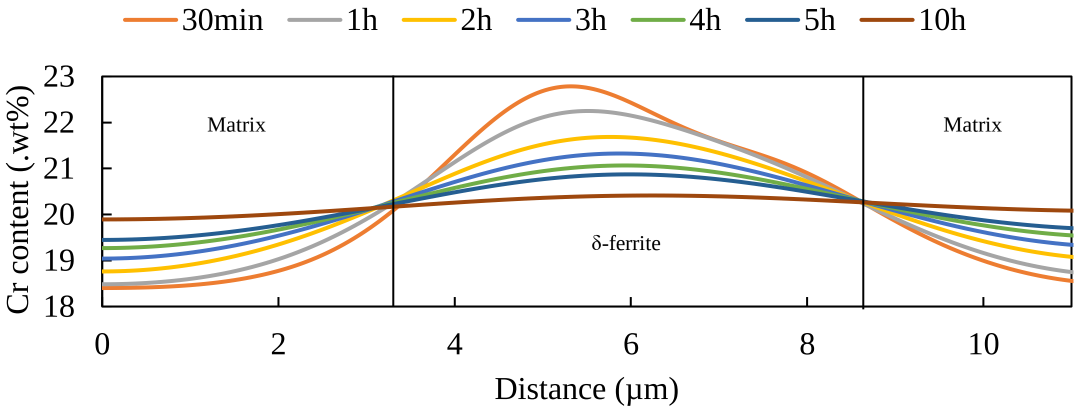

(a)

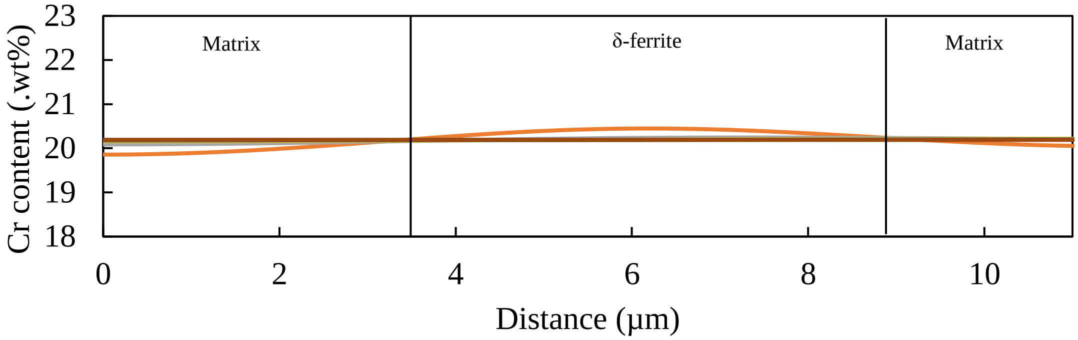

(b)

Figure 77: 304L DICTRA simulations at (a) 1000°C, and (b) 1150°C, showing the Cr content evolution after different annealing times.

The simulation for the 304L material was conducted following the same parameters and approach used before. The results can be visualized on Figure 78. Fixing the distance where high Cr were measured along with lower Ni contents (representing the δ-ferrite), it was possible to extrapolate the simulation annealing time in order to investigate these chemical elements behavior at this δ-ferrite region.

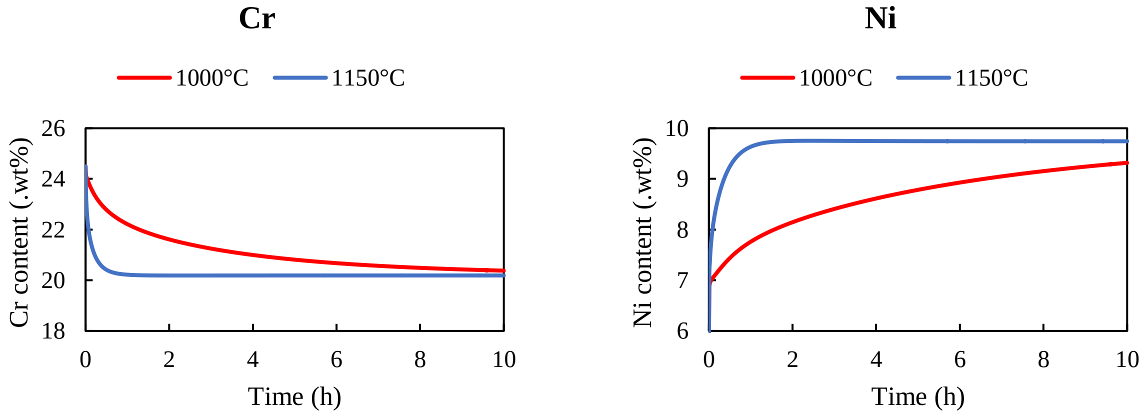

Figure 78: Variation of Cr and Ni at the δ-ferrite location as a function of the predicted time by DICTRA, for the 304L steel.

After 1000°C, a chemical stabilization of Cr and Ni was perceptible as the times reached values closer to 10 hours. Therefore, longer heat treatments would be necessary to fully accommodate the 304L microstructure in terms of chemical composition at this temperature. On the other hand, when the higher temperature was analyzed, both elements exhibited a similar behavior, with a substantial accommodation after 2 hours, followed by a constant and homogeneous tendency, indicating that the dissolution of δ-ferrite is more accentuated at shorter times, and tends to deaccelerate as the time grew.

5.4 Activation Energy Calculation

The activation energy for the annealing heat treatments was calculated using Equations 2-7 and 2-8, and the results are presented on Figure 79, for all the 15-5PH material. The Arrhenius equation was utilized, and the measured activation energy was of 94.33 kJ/mol.

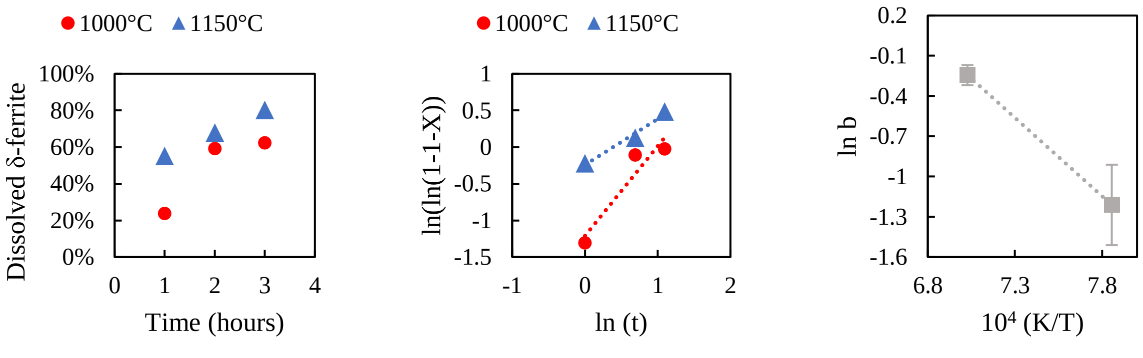

(a) (b) (c)

Figure 79: 15-5PH activation energy calculation processs showing: (a) the dissolved δ-ferrite fraction; (b) the variation of the δ-ferrite fraction with the natural logarithm of the annealing time; and (c) the temperature dependence of the rate constant for the dissolution process.

Figure 80 exhibits the results obtained for the Jethete alloy, with the activation energy evaluated as 33.39 kJ/mol.

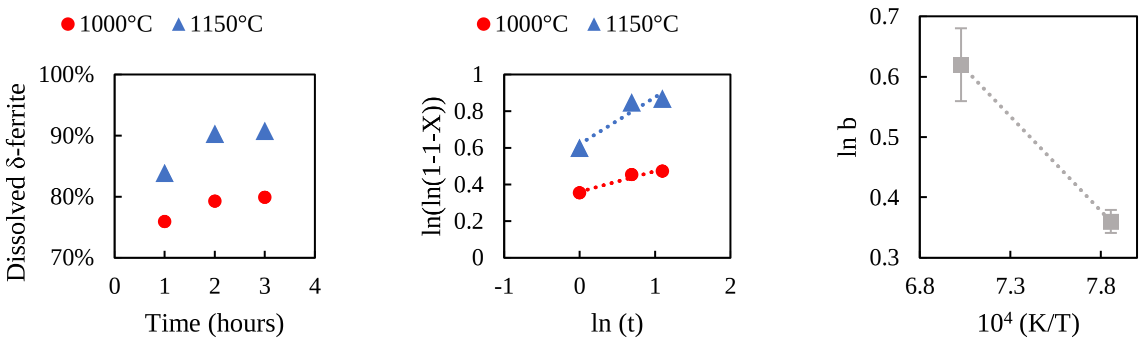

(a) (b) (c)

Figure 80: JET activation energy calculation processs showing: (a) the dissolved δ-ferrite fraction; (b) the variation of the δ-ferrite fraction with the natural logarithm of the annealing time; and (c) the temperature dependence of the rate constant for the dissolution process.

Figure 81 shows the results for the 304L material, with the activation energy calculated as 30.80 kJ/mol.

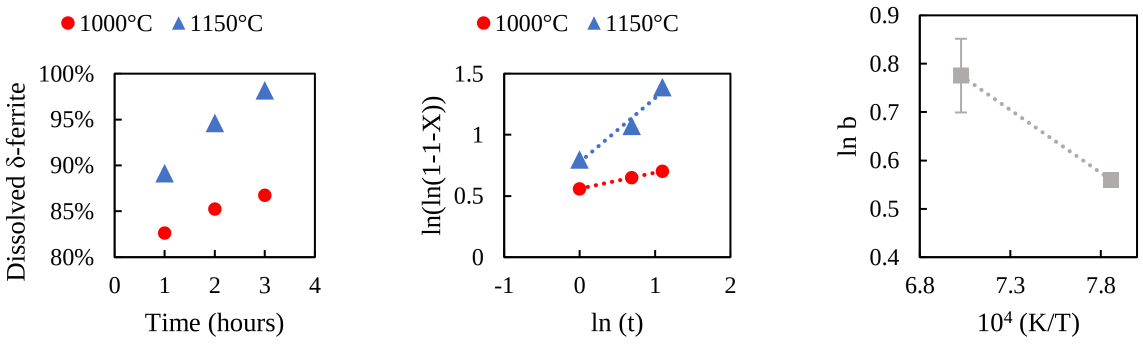

(a) (b) (c)

Figure 81: 304L activation energy calculation processs showing: (a) the dissolved δ-ferrite fraction; (b) the variation of the δ-ferrite fraction with the natural logarithm of the annealing time; and (c) the temperature dependence of the rate constant for the dissolution process.

Since the Jethete and the 304L materials presented a behavior of fasting dissolving the δ-ferrite at the early stages of annealing, with the dissolution rate becoming slower as the time increased, their activation energies were calculated exhibiting lower values when compared with the 15-5PH alloy. The reason is that throughout all the experimental annealing design, the dissolved δ-ferrite fractions did not substantially change with the increase of time. In order to elucidate this idea, the Jethete steel presented a dissolved fraction of 75.95% after 1 hour at 1000°C, and of 79.91% after 3 hours at the same temperature, while the 15-5PH alloy was characterized showing 23.75% of dissolved δ-ferrite after 1 hour, and 62.21% after 3 hours at 1000°C, corroborating for the higher activation energy.

6.0 Conclusions

Comprehending the dissolution behavior of δ-ferrite was possible by considering the variety of information provided by the present work. Each experimental approach was selected to investigate the effect of well-known processing parameters, such as time and temperature, in addition with variables like % of deformation and strain rate, which delivered a new understanding of the δ-ferrite dissolution. To accomplish that, all alloys were subjected to conventional annealing treatments and hot compression experiments.

A significant dissolution was induced after the first stages of annealing for the Jethete and 304L alloys, where values close to 70% were measured. On the other hand, the 15-5PH alloy presented a slower dissolution process during the initial stages of annealing, with 20% of dissolved δ-ferrite area fraction calculated. This behavior can be associated with the presence of precipitates along the δ-ferrite boundaries on the as-received sample, differently from what was observed for the other two alloys at their re-melted condition. The faster dissolution rate at higher temperatures promoted a higher activation energy to the 15-5PH steel.

Analyzing the δ-ferrite area fraction, conventional annealing treatments reported a consistent decrease as the soaking time increased, for all the analyzed materials. Interestingly, the introduction of deformation to the system promoted an even shorter diffusion path for all the three stainless steels, as the area fraction significantly decreased just after 10 minutes of post processing heat treatments. However, no significant area fraction differences could be reported when the strain rate was changed. A slight decrease was noticed when higher strain rates were adopted, but all measurements remained within the standard deviation of one another. Therefore, time and temperature more effectively influence the dissolution of δ-ferrite than strain rate.

Samples subjected to compression under different strain rates did not exhibit remarkable Cr variation between the δ-ferrite and the matrix. However, chemical deviations analyzed after EPMA analysis were more perceptible after conventional annealing heat treatments, where the microstructural homogenization was noticed, as δ-ferrite and matrix chemistries were approximated as longer annealing treatments were performed. The EPMA results were confirmed with DICTRA simulations, that predicted microstructural accommodation more accentuated after 1150°C, with the necessary time for fully homogenization varying for each alloy.

Comparing the three alloys studied during the present work, it seems that the 304L austenitic stainless steel exhibited a faster δ-ferrite dissolution behavior under the current experimental conditions. A more intense area fraction contraction could be observed in combination with a faster chemical homogenization, posteriorly to all the designed heat treatments simulations. This affirmation is corroborated by the lower activation energy empirically calculated for the 304L alloy, when compared with the 15-5PH and the Jethete steels, attaching an easier dissolution behavior to that material. Therefore, the dissolution kinetics of δ-ferrite is strongly related to the chemical composition of the base steel.

7.0 Future Work

The 15-5PH, M-154 Jethete, and the 304L alloys could be further investigated by changing the experimental approach, using different temperatures and holding times during annealing, and distinct deformation rates combined with longer post processing heat treatments after hot compression. These complementary parameters would abroad the actual studied range, enriching the results and helping to conclude about which parameter represents as more effective for each system.

Additionally, the response of δ-ferrite to annealing and hot deformation processes could be explored on other stainless-steel materials. Since the chemical composition has an important role on the formation/dissolution behavior of this phase, changing the chemistry could generate steels that would respond differently to the adopted experimental approaches.

The present project could be more in-detail validated if the mechanical properties of the studied alloys after each physical simulation were evaluated. With the application of impact toughness testing, for example, the influence of the δ-ferrite on the studied steels physical properties would be further investigated and analyzed. Complementarily, the efficacy of the hot compression experiments would be concluded in a more illustrative and practical way.

Other analyses and techniques could be applied, such as the AFM microscopy or nano-hardness indentation. Those methods would help us to understand more about the strain along the δ-ferrite boundaries. As observed, with the increase in dissolution, morphological changes are followed by a reduction in δ-ferrite fraction, and possibly by a change in strain, occurring at the higher energy regions dividing matrix and δ-ferrite areas.

Finally, since the thermodynamic predictions were calculated by only considering the effect of time and temperature, other equations could have been added to the system and computations in order to englobe the effect of deformation and strain rates on the dissolution behavior of δ-ferrite.

Bibliography

[1] Bhadeshia, H. K. D. H., & Honeycombe, R. W. K. (2006). Steels. *Butterworth-Heinemann*.

[2] Gardner, L. (2005). The Use of Stainless Steel in Structures. *Progress in Structural Engineering and Materials*, *7*(2), 45-55. https://doi.org/10.1002/pse.190

[3] Guide, S. D. (2013). Structural Stainless Steel. *American Institute of Steel Construction*. Chicago, IL, USA.

[4] Vander Voort, G. F., Lucas, G. M., & Manilova, E. P. (2004). Metallography and Microstructures of Stainless Steels and Maraging Steels. *Materials Park, ASM International*, 670-700.

[5] Davis, J. R. (2000). Stainless steels. *Materials Park: ASM International*.

[6] Kain, V. (2011). Stress Corrosion Cracking (SCC) in Stainless Steels. *Stress Corrosion Cracking*, 199-244. Woodhead Publishing. https://doi.org/10.1533/9780857093769.3.199

[7] McGuire. (2008). Stainless Steels for Design Engineers. *ASM International*.

[8] Wang, D., Kahn, H., Ernst, F., & Heuer, A. H. (2015). NiAl Precipitation in Delta Ferrite Grains of 17-7 Precipitation-Hardening stainless steel during low-temperature interstitial hardening. *Scripta Materialia*, 108, 136-140. https://doi.org/10.1016/j.scriptamat.2015.07.001

[9] San Martin, D., Del Castillo, P. R. D., Peekstok, E., & Van Der Zwaag, S. (2007). A New Etching Route for Revealing the Austenite Grain Boundaries in an 11.4% Cr precipitation hardening semi-austenitic stainless steel. *Materials characterization*, 58(5), 455-460. https://doi.org/10.1016/j.matchar.2006.06.009

[10] Lula, R. A., Parr, J., & Hanson, A. (1986). Stainless Steel. *American Society for Metals*. Metals Park, OH, USA.

[11] Isfahany, A. N., Saghafian, H., & Borhani, G. (2011). The Effect of Heat Treatment on Mechanical Properties and Corrosion Behavior of AISI420 Martensitic Stainless Steel. *Journal of Alloys and Compounds*, 509(9), 3931-3936. https://doi.org/10.1016/j.jallcom.2010.12.174

[12] Michler, T. (2016). Austenitic Stainless Steels. *Reference Module in Materials Science and Materials Engineering*, 1(6). https://doi.org/10.1016/B978-0-12-803581-8.02509-1

[13] Wright, R. N. (2011). Relevant Aspects of Carbon and Low-Alloy Steel Metallurgy. *Wire Technology Process Engineering and Metallurgy*. Butterworth-Heinemann. Oxford. p, 175-197. https://doi.org/10.1016/B978-0-12-382092-1.00014-2

[14] Laxminarayana, P., & Reddy, A. C. (2008). Quantification of Delta Ferrite in Austenitic Stainless-Steel Cast in Investments Shell Moulds. *6th National Conference on Materials and Manufacturing Processes*, Hyderabad (pp. 62-65).

[15] ASTM 800/A 800M-01 (2001), Standard Practice for Steel Casting, Austenitic Alloy, Estimating Ferrite Content Thereof, *American Society for Testing and Material*.

[16] Passos, D. D. O., & Otubo, J. (2010). A Influência da Ferrita Delta em Aços Inoxidáveis Austeníticos Forjados. *Revista Escola de Minas*, 63, 57-63. https://doi.org/10.1590/S0370-44672010000100010

[17] Bashu, S. A., Singh, K., & Rawat, M. S. (1990). Effect of Heat Treatment on Mechanical Properties and Tracture Behaviour of a 12CrMoV Steel. *Materials Science and Engineering*. A, 127(1), 7-15. https://doi.org/10.1016/0921-5093(90)90184-5

[18] Kim, S. H., Moon, H. K., Kang, T., & Lee, C. S. (2003). Dissolution Kinetics of Delta Ferrite in AISI 304 Stainless Steel Produced by Strip Casting Process. *Materials Science and Engineering*. A, 356(1-2), 390-398. https://doi.org/10.1016/S0921-5093(03)00152-7

[19] Li, S., Eliniyaz, Z., Zhang, L., Sun, F., Shen, Y., & Shan, A. (2012). Microstructural Evolution of Delta Ferrite in SAVE12 Steel Under Heat Treatment and Short-Term Creep. *Materials characterization*, 73, 144-152. https://doi.org/10.1016/j.matchar.2012.08.009

[20] Steiner Petrovič, D., Klančnik, G., Pirnat, M., & Medved, J. (2011). Differential Scanning Calorimetry Study of the Solidification Sequence of Austenitic Stainless Steel. *Journal of Thermal Analysis and Calorimetry*, 105(1), 251-257. https://doi.org/10.1007/s10973-011-1375-2

[21] Mateša, B., Samardžić, I., & Dunđer, M. (2012). The Influence of the Heat Treatment on Delta Ferrite Transformation in Austenitic Stainless Steel Welds. *Metalurgija*, 51(2), 229-232.

[22] Arh, B., Tehovnik, F., & Vode, F. (2021). Transformation of the δ-Ferrite in SS2343 Austenitic Stainless Steel upon Annealing at 1050° C, 1150° C and 1250° C. *Metals*, 11(6), 935. https://doi.org/10.3390/met11060935

[23] Ghosh, S. K., Mahata, D., Roychaudhuri, R., & Mondal, R. (2012). Effect of Rolling Deformation and Solution Treatment on Microstructure and Mechanical Properties of a Cast Duplex Stainless Steel. *Bulletin of Materials Science*, 35(5), 839-846. https://doi.org/10.1007/s12034-012-0353-z

[24] Gigović-Gekić, A., Avdušinović, H., Hodžić, A., & Mandžuka, E. (2020). Effect of Temperature and Time on Decomposition of δ-ferrite in Austenitic Stainless Steel. *Materials and Geoenvironment*, 67(2), 65-71. https://doi.org/10.2478/rmzmag-2020-0007

[25] Thelning, K. E. (1984). Nitriding, *Steel and its Heat Treatment*. 2nd, 492.

[26] Hernandez-Silva, D., & RD, M. (1992). The Spheroidization of Cementite in a Medium Carbon Steel by Means of Subcritical and Intercritical Annealing. *ISIJ international*, 32(12), 1297-1305. https://doi.org/10.2355/isijinternational.32.1297

[27] Luzginova, N. V., Zhao, L., & Sietsma, J. (2008). The Cementite Spheroidization Process in Hhigh-Carbon Steels with Different Chromium Contents. *Metallurgical and Materials Transactions A*, 39(3), 513-521. https://doi.org/10.1007/s11661-007-9403-3

[28] Gill, T. P. S., Vijayalakshmi, M., Gnanamoorthy, J. B., & Padmanabhan, K. (1986). Transformation of Delta-Ferrite During the Postweld Heat Treatment of Type 316 L Stainless Steel Weld Metal. *Weld. J.*, 65(5), 122.

[29] Cui, C., Gao, X., Su, G., Gao, C., Liu, Z., & Misra, R. D. K. (2018). Effect of Thermal Treatment on the Evolution of Delta Ferrite in 11Cr–3Co–2.3W Steel. *Materials Science and Technology*, 34(17), 2087-2096. https://doi.org/10.1080/02670836.2018.1510072

[30] Shaikh, H., Khatak, H. S., Seshadri, S. K., Gnanamoorthy, J. B., & Rodriguez, P. (1995). Effect of Ferrite Transformation on the Tensile and Stress Corrosion Properties of Type 316 L Stainless Steel Weld Metal Thermally Aged at 873 K. *Metallurgical and Materials Transactions A*, 26(7), 1859-1868. https://doi.org/10.1007/BF02670773

[31] Wang, P., Lu, S. P., Xiao, N. M., Li, D. Z., & Li, Y. Y. (2010). Effect of Delta Ferrite on Impact Properties of Low Carbon 13Cr–4Ni Martensitic Stainless Steel. *Materials Science and Engineering A*, 527(13-14), 3210-3216. https://doi.org/10.1016/j.msea.2010.01.085

[32] Bhambri, S. K. (1986). Intergranular Fracture in 13 wt% Chromium Martensitic Stainless Steel. *Journal of Materials Science*, 21(5), 1741-1746. https://doi.org/10.1007/BF01114734

[33] Tseng, C. C., Shen, Y., Thompson, S. W., Mataya, M. C., & Krauss, G. (1994). Fracture and the Formation of Sigma Phase, $M_{23}C_6$, and Austenite from Delta-Ferrite in an AlSl 304L Stainless Steel. *Metallurgical and Materials Transactions A*, 25(6), 1147-1158. https://doi.org/10.1007/BF02652290

[34] Cho, J. Y., Czerwinski, F., & Szpunar, J. A. (2000). The Effect of Reheating Conditions and Chemical Composition on δ ferrite Content in Austenitic Stainless-Steel Slabs. *Journal of Materials Science*, 35(8), 1997-2003. https://doi.org/10.1023/A:1004734906671

[35] Raghunathan, V. S., Seetharaman, V., Venkadesan, S., & Rodriguez, P. (1979). The Influence of Post Weld Heat Treatments on the Structure, Composition and the Amount of Ferrite in Type 316 Stainless Steel Welds. *Metallurgical Transactions A*, 10(11), 1683-1689. https://doi.org/10.1007/BF02811701

[36] McLean, M. (1978). Microstructural Instabilities in Metallurgical Systems - A Review. *Metal Science*, 12(3), 113-122. https://doi.org/10.1179/msc.1978.12.3.113

[37] Borgenstam, A., Höglund, L., Ågren, J., & Engström, A. (2000). DICTRA, A Tool for Simulation of Diffusional Transformations in Alloys. *Journal of Phase Equilibria*, 21(3), 269-280. https://doi.org/10.1361/105497100770340057

[38] Andersson, J. O., Helander, T., Höglund, L., Shi, P., & Sundman, B. (2002). Thermo-Calc & DICTRA, Computational Tools for Materials Science. *Calphad*, 26(2), 273-312. https://doi.org/10.1016/S0364-5916(02)00037-8

[39] Niessen, F., Tiedje, N. S., & Hald, J. (2017). Kinetics Modeling of Delta-Ferrite Formation and Retainment During Casting of Supermartensitic Stainless Steel. *Materials & Design*, 118, 138-145. https://doi.org/10.1016/j.matdes.2017.01.026

[40] Ravibharath, R., Muthupandi, V., Bala Srinivasan, P., & Devakumaran, K. (2020). Characterization of Solidification Cracking in 304HCu Austenitic Stainless Steel Welds. *Transactions of the Indian Institute of Metals*, 73(9), 2345-2353. https://doi.org/10.1007/s12666-020-02028-1

[41] Schäfer, L. (1998). Influence of Delta Ferrite and Dendritic Carbides on the Impact and Tensile Properties of a Martensitic Chromium Steel. *Journal of Nuclear Materials*, 258, 1336-1339. https://doi.org/10.1016/S0022-3115(98)00200-1

[42] Zhang, X. F., Terasaki, H., & Komizo, Y. (2011). Correlation of Delta-Ferrite Precipitation with Austenite Grain Growth During Annealing of Steels. *Philosophical Magazine Letters*, 91(7), 491-497. https://doi.org/10.1080/09500839.2011.587464

[43] Martins, M., & Casteletti, L. C. (2009). Microstructural Characteristics and Corrosion Behavior of a Super Duplex Stainless Steel Casting. *Materials Characterization*, 60(2), 150-155. https://doi.org/10.1016/j.matchar.2008.12.010